DEMOCRATIC AND POPULAR REPUBLIC OF ALGERIA
MINISTRY OF HIGH EDUCATION AND SCIENTIFIC RESEARCH

THESIS

Presented at

ABOU-BAKR BELKAID UNIVERSITY - TLEMCEN

Faculty of Sciences-Physics Department

by

Ms BOUAYED born KANOUN Nawel

To obtain the degree of

DOCTOR OF PHYSICS

Option: Materials Science

Theme

Density functional theory study of physical properties of nitrides, rare-earth dioxides and silicon-germanium oxynitrides

At 27 June 2011 with the board of examiners:

Prof. Boumédiènne BENYOUCEF	Chairman	University of Tlemcen
Prof. Berrezoug BELGOUMENE	Examiner	University of Saida
Dr. Boumédiènne LASRI	Examiner	University of Saida
Dr. Smaine BEKHECHI	Examiner	University of Tlemcen
Dr. Abdelkrim MERAD	supervisor	University of Tlemcen
Dr. Souraya GOUMRI-SAID	Co-Supervisor	King Abdullah University of Science and Technology

DEDICATIONS

I dedicate this thesis to:

My lovely children Sanaa , Rawida and Ahmed Abderrahmen

My dear husband Fouad

My lovely parents, my parents in law and my grandmother.

My brother Benali as well as his wife Souraya

My sister souhila as well as her husband

My brothers Mohammed Adil and Ahmed-Ali

My well liked Areslane, Mehdi Sidi-Mohammed, Nihel and Smain

Nawel

Acknowledgements

With the help of God Almighty, I was able to accomplish this modest work.

This thesis was achieved within the « Laboratoire Equipe Physique de l'état solide, LPT, Département de Physique» at Abou-BekrBelkaid University of Tlemcen.

I would like to express my deep gratitude to Dr. Abdelkrim MERAD, Maitre de Conférences "A" at the University of Tlemcen and he is my supervisor for this thesis. I wish to express my thanks to him for guiding me along this work, for his permanent follow-up, his attentive readings as well as for his confidence, his comprehension during these years of research.

I would like to express my deep gratitude to my Co-Supervisor Dr. S. GOUMRI-SAID, researcher at King Abdullah University of Science and Technology , for teaching me the new concepts and techniques on "computational material "during my stay in Belgium in 2008, for critical reading of my results, she was always available to answer my questions, I thank her for helping me in writing this manuscript, she found enough and necessary time to be effective in the corrections of my various versions, thank you for your guidance, encouragement and support throughout this work.

I would like to thank Mr. B. BENYOUCEF Professor at University of Tlemcen, to have accepted to chair the jury of this thesis.

I hold to present my thanks to M^{r}B. BELGOUMENE, Professor at University of Saida, M^{r}B. LASRI Maître de conferences "A" at University of Saida, and M^{r}S. BEKHECHI, Maître de conferences "A" at University of Tlemcen, that makes me honor to judge this thesis.

I would also like to acknowledge my brother Dr. KANOUN Mohamed Benali researcher at King Abdullah University of Science and Technology for his good ideas on different sides of my research, for his comments and clarifications that enriched this manuscript. I wish to thank Benali for his permanent encouragements and assistance.

All My thanks go to my family. I am indebted to my husband for helping me throughout these years. To my parents, my parents in law, my sister and brothers, your prayers helped me to accomplish this work.

My thanks go also to my colleagues in the research group" *Equipe Physique de l'état solide"*- for their kind support and encouragement. Thanks for all.

Contents

List of Figures:

List of Tables

INTRODUCTION

Solid materials are of great technological importance but the challenge to theory and computation is that they are governed by very different length and time scales. These may differ by many orders of magnitude depending on the specific applications. On the length scale from meters down to micrometers classical mechanics and continuum models are dominant conceptual frameworks for investigation of diverse material properties. However, when one comes to the nanometer scale or atomic dimensions measured in angstrom, all properties are determined (or critically influenced) by the electronic structure of the solid state.

The electronic structure is determined by resolution of the quantum mechanics equations. Understanding how these equations work out can enable one to make qualitative predictions about structural, mechanical, electronic, spectroscopic, and optical properties. Solving these equations can also give quantitative predictions of these properties. In the past, it was necessary to use very severe approximations when solving the quantum mechanics equations, and the most powerful computers available were needed. The results were hard to interpret, and of qualitative value only. Nowadays, even standard desktop computers are far more powerful than state-of-the-art supercomputers of 20 years ago, and the programs used to solve the equations have become much more powerful. Therefore, ab-initio approaches to atomic electronic structure are much more widespread and useful.

The manuscript will focus on structural, electronic and magnetic aspects as well as problems stability in different systems. Our interest lies on three categories of systems: nitrides, rare earth oxides and oxynitrides. Even nowadays with efficient methods and powerful computers it remains challenging to achieve an accurate description of the close lying electronic states of such compounds, because of the complex interactions between them.

The first chapter will be devoted to a detailed presentation of the numerical tool introducing the spine of our work mainly the ab-initio methods based on density functional theory. Throughout this chapter we will show the effect of different approximations adapted to the various systems such as the rare earth elements which require the application of strong correlation (i.e Hubbard U).

Indeed, in chapter 2, we apply the former detailed tool to study the copper nitrides in zincblende, rocksalt and fluorite structures. Then the quasi-harmonic Debye model will be applied to investigate the temperature effect on the variation of linear thermal expansion parameters and the specific heat.

Chapter 3 is devoted to the strong correlation effect in the most challenging materials rare earth dioxides. Our interest in these materials dates back to the work achieved during the Magister thesis where we applied correction to the local density approximation by taking into account of the Hubbard model parameter (U). The rare-earth dioxides are more challenging and need both of U parameter and spin-orbit coupling to correct generalized gradient calculations. Furthermore we try to understand the properties of rare earth dioxides by applying the former approximation to determine the structural, elastic, electronic and magnetic properties.

In Chapter 4, we focus our attention to the Oxynitrides based on Silicon and Germanium: Si_2N_2O and Ge_2N_2O. These compounds contain both of nitrogen and oxygen. We present a deep study of their optimized geometries, crystal structure, bonding, mechanical, thermodynamic and the optical properties will using the density function (DFT) calculation by means of two methods, the full-potential linearized augmented plane-wave plus local orbitals and plane-wave pseudopotential.

Finally, the manuscript is accomplished by general conclusions with a discussion of the main results and outlook on the future research. We hope that our work will open interesting perspectives, particularly on the prediction study of new nitrides, oxides and their mixing compounds oxynitrides.

Chapter One

Theoretical methods and numerical tools

Abstract

In this chapter we outline the theoretical framework that underpins the bulk of this work. We begin by introducing the concept of density functional theory, and explain how the physical systems can be described by the many-electrons Schrödinger equations. We introduce the Kohn-Sham method based on of DFT, and how this can be implemented efficiently with different basis set and using appropriate approximations. In particular, we talk about the exchange-correlation potential and related numerical approximations. Finally, we will see the impact of DFT approximations through simple physical properties of some compounds.

Les ordinateurs ont le pouvoir de transformer notre monde en un monde qui nous soit tout à fait étranger.
Dave Barry

1.1. Introduction

The description of the physical properties of interacting many-particle systems has been one of the most important goals of physics during this century. The problem is to derive the properties of many-particle systems from the quantum mechanical laws. According to quantum mechanics, the whole information of a system of interacting electrons and nuclei is contained in the many-body wave function ψ, which can be obtained by solving the Schrodinger (or Dirac equation) equation of *3N* spatial variables and *N* spin variables (for electrons) where N is the number of particles in the system:

$$H\psi = E\psi \tag{1.1}$$

H is the many-particle hamiltonian which describes the various contributions to the total energy of the system of *N* electrons and *M* nuclei given by:

$$H = T_{el} + T_n + V_{n-el} + V_{el-el} + V_{n-n} \tag{1.2}$$

The Hamiltonian operator can be expressed more precisely by the equation:

$$H = -\frac{h^2}{2}\sum_i \frac{\nabla_{r_i}^2}{m_e} - \frac{h^2}{2}\sum_i \frac{\nabla_{R_i}^2}{M_e} - \frac{1}{4\pi\varepsilon_0}\sum_i^N \sum_\alpha^M \frac{e^2 Z_\alpha}{|\vec{R}_\alpha - \vec{r}_i|} + \frac{1}{8\pi\varepsilon_0}\sum_i^N \sum_{i\neq j}^N \frac{e^2}{|\vec{r}_i - \vec{r}_j|}$$

$$+ \frac{1}{8\pi\varepsilon_0}\sum_\beta^M \sum_\alpha^M \frac{e^2 Z_\alpha Z_\beta}{|\vec{R}_\alpha - \vec{R}_\beta|} \tag{1.3}$$

In which the different terms correspond respectively to:

T_{el} : kinetic energy for the M electrons of mass m_e at $\vec{r}_i$

T_n : kinetic energy operator for the N nuclei of mass Me at $\vec{R}_\alpha$

$V_{n\text{-}el}$: Coulomb interaction attractive nuclei - electrons

$V_{n\text{-}n}$: Coulomb repulsive interaction nuclei– nuclei

$V_{el\text{-}el}$: Coulomb repulsive interaction between electrons and other electrons.

It is out of question that the problem cannot be solved without making approximations somewhere along the line. A first level of approximation can be obtained by the Born-Oppenheimer, or adiabatic, approximation **[Born-27],** and treat the nuclei as classical particles that move on a time scale much longer than that of the electrons. This means that, as far as calculations on the electrons are concerned, the nuclei can be considered to be fixed in space. The many-body problem is therefore reduced to the smaller problem of a system of electrons moving in some external potential, i.e. the potential created by the positively charged nuclei. Thus, the Hamiltonian given before reduces to the so-called electronic Hamiltonian which is central to the theory of electronic structure.

$$H^{elec} = T_{el} + V_{nu-el} + V_{el-el} \tag{1.4}$$

The quantum many body problem obtained after the first level approximation (Born-Oppenheimer) is much simpler than the original one, but still far too difficult to solve. Several methods exist to treat the problem. Solution of such models generally requires the use of approximation schemes: the independent electron approximation, the Hartree theory and a historically very important one is the Hartree-Fock (HF) method, described in many condensed matter textbooks. It performs very well for atoms and molecules, and is therefore used a lot in quantum chemistry. For solids it is less accurate, however. We will not treat HF, but explain a more modern and probably also more powerful method: Density Functional Theory (DFT). Although its history goes back to the early thirties of the 20th century, This method has the double advantage of being able to treat many problems to a sufficiently high accuracy, as well as being computationally simple (simpler than even the Hartree scheme).

The main idea of DFT is to describe an interacting system of fermions via its density ρ and not via its many-body wave function. For N electrons in a solid, which obey the Pauli principle and repulse each other via the Coulomb potential, this means that the basic variable of the system depends only on three -- the spatial coordinates x, y, and z -- rather than 3N degrees of freedom.

1. 2. Fundamentals of density functional theory

Density functional theory (DFT) is a quantum mechanical modeling method used in physics and chemistry to investigate the electronic structure (principally the ground state) of many-body systems, in particular atoms, molecules, and the condensed phases. With this theory, the properties of a many-electron system can be determined by using functionals, i.e. functions of another function, which in this case is the spatially dependent electron density ρ. Hence the name density functional theory comes from the use of functionals of the electron density. DFT is among the most popular and versatile methods available in condensed-matter physics, computational physics and computational chemistry. Historically, the first who expressed energy in terms of density were L. H. Thomas **[Thomas-27]** and E. Fermi **[Fermi-28]** in 1927. But DFT has been formally established in 1964 by two theorems due to Hohenberg and Kohn **[Hohenberg-64].**

1.2.1. Hohenberg-Kohn Theorem

In 1964, Hohenberg and Kohn set out a simple theorem which relates the potential and the electronic density in a quantum system **[Hohenberg-64**]. Stated simply the Hohenberg Kohn theorems are as follows:

1.2.1. a) First theorem [Hohenberg1964]:

The external potential $V_{ext}(r)$ (to within a constant) and hence the total energy is a unique functional of the density $\rho(r)$.

$$\rho(r) \Rightarrow V_{ext}(r) \tag{1.5}$$

In fact all properties of the system, including excited state properties are, in principle, exact functionals of the electron density. The reason for this, as was proven by Hohenberg and Kohn, is that there is a one-to-one mapping between the electron density $\rho(r)$ and the external potential (Figure 1.1). If we happen to know the density, then, in principle, we know the external potential, and if we know the external potential we can, again in principle, solve the many-electron Schrödinger equation and know everything about the system **[Gibson-06].**

$$\rho \Rightarrow V_{ext} \Rightarrow H \Rightarrow \psi \Rightarrow E \text{ (and all properties)} \quad (1.6)$$

Of course, this is not yet of any practical use, because the whole point of using DFT is so that we can avoid having to deal with the many-electron Schrödinger equation. Nevertheless, we are provided, at least in principle, with a means of finding the ground state energy for a given external potential. The energy functional ***E*** alluded to in the first Hohenberg-Kohn theorem can be written in terms of the external potential in the following way:

$$E(\rho) = E[\rho(r)] = F_{HK}(\rho) + \int \rho(\vec{r}) V_{ext}(\vec{r}) d\vec{r} \quad (1.7)$$

With

$$F_{HK}[\rho(r)] = T_{el}[\rho(r)] + V_{el-el}[\rho(r)] \quad (1.8)$$

Where $F_{HK}[\rho(r)]$ is the Hohenberg-Kohn density functional universal for any many-electron system. An explicit expression for the Hohenberg-Kohn functional F_{HK} is not known, notably the kinetic $T_e[\rho]$, and electron-electron functional $V_{el-el}[\rho]$ are unknown.

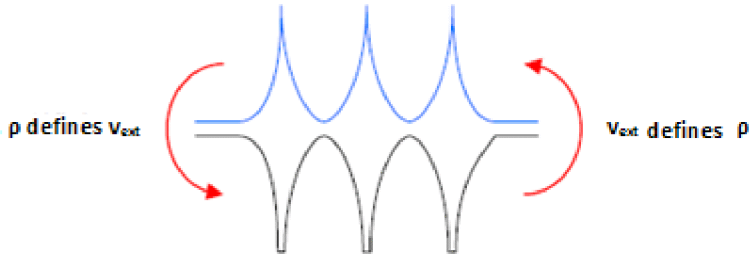

Figure1.1: Correspondence between the electron density $\rho(r)$ and the external potential.

1.2.1. b) Second theorem: variational principle

The functional E for the ground state energy is minimized by the ground state electron density ρ_0.

$$E = \min_{\rho} E[\rho(\vec{r})] \quad (1.9)$$

This theorem being a direct consequence of the variational principle of Rayleigh-Ritz enables the ground state electron density to be calculated variationally **[Renold-03].**

The first theorem is a statement about the existence of an energy functional E and gives no information about this functional form. If $E(\rho)$ were known the ground state electron density could easily be found using the second theorem hence requiring the variation of the energy functional with respect to the electron density to vanish. At this stage we are still no nearer to a practical method because exact evaluation of $F(\rho)$ would require us to solve the many-body Schrödinger equation. The question that arises is, what should we use for functional F_{KH}??

1.2.2. Kohn-Sham equations

In 1965, Kohn and Sham made a significant breakthrough when they showed that the problem of many interacting electrons in an external potential can be mapped exactly to a set of non-interacting electrons in an effective external potential **[Kohn-99, Kohn-65]**. Indeed, central to the Kohn-Sham method is the introduction of a fictitious auxiliary system, which is intended in some way to mimic the true many-electron system that we are dealing with. This fictitious system is a set of particles whose properties are identical to those of electrons, except that the electron-electron repulsive interaction is switched off. The particles move in some fictitious external potential $V_{KS}(r)$ known as the Kohn-Sham potential, which is defined such that the system's ground state density equals ρ the same density as the electronic system for which we want to evaluate $F(\rho)$.This assumes that the true ground state density actually is also the ground state density of a non-interacting system. Because there are no interactions between the particles, the ground state wavefunction of this system is far less complicated that of the true, interacting, system. In fact, we can write the ground state wavefunction explicitly in terms of simple single-particle wavefunctions, and the kinetic energy and electron density are known exactly from the orbitals.

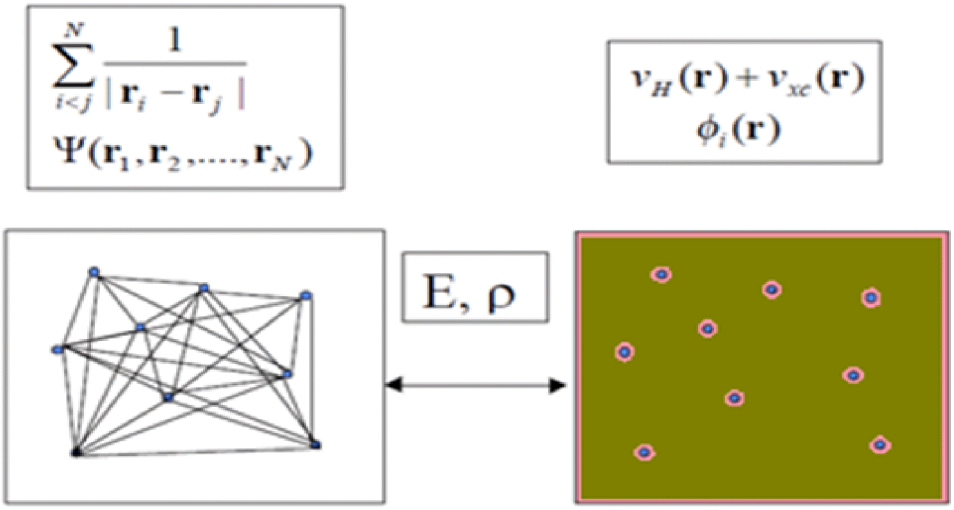

Figure 1.2: A cartoon representation the relationship between the "real" many body system (left hand side) and the non-interacting system of Khon Sham density functional theory (right hand side)

The confrontation between these two systems so different, so similar (same energy, same density distribution) springs an exact formal expression and (in principle) accessible to the functional.

$$F_{HK}[\rho(r)] = T_{el}[\rho(r)] + \int \frac{\rho(r)\rho(r')}{|r-r'|} dr dr' + E_{XC}[\rho] \qquad (1.10)$$

Where $T_{el}[\rho]$ is the kinetic energy of non-interacting electrons system $T_{el}[\rho] = \sum_{i=1}^{N} \langle \varphi_i | -{}^{1}/_{2} \nabla^2 | \varphi_i \rangle$ the second term corresponds to the electron-electron interaction is the classical Coulomb interaction– or Hartree energy $-V_H[\rho(r)] = \frac{1}{2} \int \frac{\rho(r)\rho(r')}{|r-r'|} dr dr'$, $Exc[\rho]$ is the unknown exchange-correlation functional, which contains all many-body aspects of the problem. Walter Kohn shared the Nobel Prize in Chemistry in 1998 for this work **[Kohn1999].** However, the exact form of the exchange-correlation energy functional is not known, thus approximations for this functional must be used. The resolution requires minimizing the total energy which can be rewritten as follows:

$$E[\rho(r)] = T_{el}[\rho(r)] + \int \rho(r)\, V^{eff}[\rho(r)] dr \qquad (1.11)$$

With

$$V^{eff}[\rho(r)] = V^{ext}(r) + \int \frac{\rho(r')}{|r-r'|} dr + V_{XC} \tag{1.12}$$

And

$$V_{XC} = \frac{\delta E_{XC}[\rho(R)]}{\delta \rho} \tag{1.13}$$

The Khon-Sham approach reduces the problem " many-body electrons' equations in simple single-electron interdependent equations of Kohn and Sham **[Sing-94]**:

The first can calculate the effective potential V_{eff}.

$$\rho(r) \rightarrow V_{eff}[\rho(r)] = v^{eff}(r) + \int \frac{\rho(r')}{|r-r'|} dr' + V_{XC}[\rho(r)] \tag{1.14}$$

The effective potential is inserted into the N single-electron Schrödinger equations to obtain the KS orbitals φi.

$$V_{eff}(r) \rightarrow \left(-\frac{h^2}{2m} \nabla_i^2 + V_{eff}(r) \right) \varphi_i(r) = \varepsilon_i \varphi_i(r) \tag{1.15}$$

The N wave functions solutions φ_i are reinjected into a third equation to calculate a new density described as a sum of single-particle densities.

$$\varphi_i(r) \rightarrow \rho(r) = \sum_{i=1}^{N} |\varphi_i|^2 \tag{1.16}$$

Both the Hartree term V_H and the exchange-correlation V_{xc} depend on the entire density function, which depends on the KS orbital which in turn depend on V_{eff}, that is, the solutions are self-consistent

1.2.3. Self-consistent scheme

The self-consistency or self-consistent scheme is an iterative process that provides the correct electron density which minimizes the total energy of the system. In the approaches mentioned before, V_{eff} depends on the density ρ, which in turn depends on the φ_i which are being searched. This means we are dealing with a *self-consistency problem*:

The solutions (φ_i) determine the original equation (V_H and V_{xc} in H_{KS}), and the equation cannot be written down and solved before its solution is known. An iterative procedure is needed to escape from this paradox (figure1.3). Some starting density ρ_0 is guessed, and a hamiltonian H_{KS1} is constructed with it. The eigenvalue problem is solved,

and results in a set of φ_1 from which a density ρ_1 can be derived. Most probably, ρ_0 will differ from ρ_1. Now ρ_1 is used to construct H_{KS2}, which will yield a ρ_2, etc. The procedure can be set up in such a way that this series will converge to a density ρ_f which generates a H_{KSf} which yields as solution again ρ_f: this final density is then *consistent* with the hamiltonian.

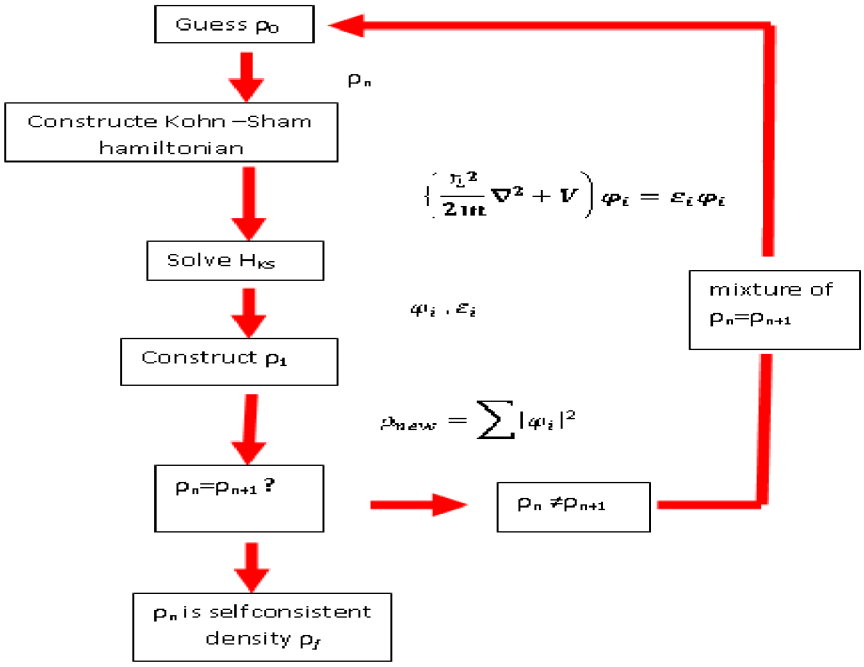

Figure1.3: Flow chart for the n[th] iteration in the self-consistent procedure to solve Kohn-Sham equations.

1.3. Energy functional exchange-correlation

The numerical advantages of the approach described are obvious. Efficient methods exist for solving single-particle Schrodinger equations with a local effective potential, the failure to find accurate expressions for the density-functional is a result of the complexity of the many-body problem which is at the heart of the definition of the universal functional.

As mentioned in the other literature**[Roquefelte-01, nawel-07],** the exchange-correlation energy is defined as what remains unknown after removing a non-interacting kinetic energy and Hartree interaction, E_{xc} is the difference between the energy of the real system and the energy of Khon Sham fictitious system:

$$E_{xc}[\rho] = T[\rho] - T^{ind}[\rho] + V_{ee}[\rho] - V_{HF}[\rho] \quad (1.17)$$

The exchange-correlation energy is decomposed into two parts: the exchange term which reflects the fact that electrons are indistinguishable fermions (due to the antisymmetry of the wave function) and the correlation term which is the rest of the Coulomb interaction between each electron (Pauli principle; Exclusion between two electrons with same spin σ).

$$\varepsilon_{xc} = \varepsilon_x + \varepsilon_c \quad (1.18)$$

DFT offers a practical and potential highly accurate alternative to the wave function methods discussed above. In practice, the utility of the theory rests on the approximation used for the exchange-correlation energy *Exc[ρ]* which has lead to a large and still rapidly expanding field of research. There are now many different flavours of functional available which are more or less appropriate for any particular study. Ultimately such judgments must be made in terms of results (i.e. the direct comparison with more accurate theory or experimental data).

1.3.1. Local density approximation

The simplest method of describing the exchange-correlation energy of an electronic system is to use the Local Density Approximation (LDA). It is the basis of all approximate exchange-correlation functions. In the LDA, the exchange-correlation functional is defined for an electron in a uniform electron gas of density **[Kohn-65]**.

$$E_{xc}^{LDA} = \int \rho(\vec{r})\epsilon_{xc}\big(\rho(\vec{r})\big)d\vec{r} \quad (1.19)$$

In other term, two hypotheses are made: 1) the effects of exchange and correlation are dominated by the density at *r* point; 2) density is a slowly varying function. In molecules and solids, however, the density tends to vary substantially in space. Despite this, the LDA has been very successfully used in many systems.

1.3.2. Involvement of the local spin-density approximation

The local spin-density approximation (LSDA) is a straightforward generalization of the LDA to include electron spin, indeed the LSDA uses the same principle as the LDA by differentiation of populations electronic spin majority and minority densities $\rho^{\uparrow}(r)$ and $\rho^{\downarrow}(r)$ in the treatment of exchange-correlation energy. Thus the functional *Exc* depends both densities of spin up and spin down:

$$E_{xc}^{LSDA}[\rho^{\uparrow},\rho^{\downarrow}] = \int \rho(\vec{r})\epsilon_{xc}^{hom}[\rho^{\uparrow}(r),\rho^{\downarrow}(r)]d^3r \qquad (1.20)$$

Where ρ is the electronic density and ε_{xc} the exchange-correlation energy of the homogeneous electron gas (HEG), it is decomposed into exchange and correlation terms linearly:

$$\epsilon_{xc}(\rho^{\uparrow},\rho^{\downarrow}) = \epsilon_x(\rho^{\uparrow},\rho^{\downarrow}) + \epsilon_c(\rho^{\uparrow},\rho^{\downarrow}) \qquad (1.21)$$

The exchange-energy density of a HEG is known analytically, is obtained by applying the expression **[Dirac-30].**

$$\epsilon_c = -3\left(\frac{3}{4\pi}\right)^{1/3}\left[\rho_{\uparrow}^{4/3} + \rho_{\downarrow}^{4/3}\right] \qquad (1.22)$$

For the correlation energy ε_c the situation is more complicated, since the correlation energy of a homogeneous electron gas is not known exactly. The ε_c can be obtained by the parameterization from Monte Carlo **[Ceperly-80]** simulations or molecular dynamics. There are several in the literature; Dirac **[Slater-64],** Wigner **[Wigner-34],** Von Barth-hedin **[Hedin-71, VonBarth-72]**, and Ceperley-Alder **[Ceperly-80]**.

This approximation has proved amazingly successful, and gives good results, However some quantities such as modulus and cohesive energy are greatly overstated, others such as lattice parameters and bond lengths are underestimated, it also gives a bad description in the case of certain magnetic systems, eg with the LDA the Iron is found ferromagnetic bcc instead of bcc antiferromagnetic **[Arras-10].**

1.3.3. Generalized gradient approximation (GGA)

In the LDA one exploits knowledge of the density at point r. Any real system is spatially inhomogeneous, i.e. it has a spatially varying density, and it would clearly be useful to also include information on the rate of this variation in the functional. A next logical step to improve on LDA is to make the exchange-correlation depend on both the density and its derivatives. This approximation is therefore called the Generalized Gradient Approximation (GGA). The concept is to make a gradient expansion of the density, which introduces a nonlocal correction:

$$E_{xc}^{GGA}[\rho] = \int f[\rho(r), \nabla\rho(r) d^3r] \tag{1.23}$$

$$E_{xc}^{GGA}\left[\rho^{\uparrow}, \rho^{\downarrow}\right] = \int f\left[\rho^{\uparrow}(r), \rho^{\downarrow}(r), \nabla(\rho^{\uparrow}(r), \rho^{\downarrow}(r))\right] d^3r \tag{1.24}$$

But there is some freedom to incorporate the density gradient, and therefore several versions of GGA exist, PW-91 version of the GGA by Perdew and Wang **[Perdew-92],** the GGA-PBE developed by Perdew, Burke and Ernzerhof (PBE) **[Perdew-96],** meta-GGA **[Perdew-99]** and a new form proposed by Wu and Cohen (WC) **[Wu-06].** Anyway, these methods offer significant advantages in the precision that they deliver the quantities that the LDA tended to describe less precisely.

1.3. 4. LDA+U approach

The standard local density approximation is a functional that works well for a vast number of compounds. But, for some crystals, the interactions between electrons are so important that they cannot be represented by the LDA alone or GGA. Generally, these highly correlated materials contain rare-earth metals or transition metals, which have partially filled *d* or *f* bands and thus localized electrons. In the last fifteen years many methods were proposed in this direction. Among these, LDA+U approach used in this thesis, first introduced by Anisimov and co-workers **[Anisimov-91,Anisimov-93,Solovyev-94**], has allowed to study a large variety of strongly correlated compounds with considerable improvement with respect to LSDA or GGA results**[Cococcioni-05].**

In LDA+U, the correlation absent in LDA is reintroduced by an on site Coulomb repulsion parameter *U* (*U* is the Hubbard term **[Hubbard-64]**). In the LDA+U, we

separate delocalized (*s* and *p* electrons) which are correctly described by the usual LDA calculation, from the localized ones *d* or *f* electrons, on which the Hubbard term will act, for the latter the total energy of a level is given by Anisimov and *al* **[Anisimov-97]:**

$$E = E_{LDA} - \frac{1}{2}UN(N-1) + \frac{1}{2}U\sum_{i\neq j} n_i n_j \qquad (1.25)$$

The orbital energies ϵ_i and the orbital-dependent potential $V_i(r)$ are given by:

$$\epsilon_i = \frac{\partial E}{\partial n_i} = \epsilon_{LDA} - U\left(\frac{1}{2} - n_i\right), V_i(r) = V_{LDA} + U(\frac{1}{2} - n_i) \qquad (1.26)$$

The LDA+U orbital-dependent potential gives upper and lower Hubbard bands with the energy separation between them equal to the Coulomb parameter *U*.

The generalized LDA+U functional is introduced and developed by Anisimov et al **[Lichtenstein-95]** as the sum of three terms:

$$E^{LDA+U}[\rho^\sigma(r), \{n^\sigma\}] = E^{LSDA}[\rho^\sigma(r)] + E^U[\{n^\sigma\}] - E_{dc}[\{n^\sigma\}] \qquad (1.27)$$

Where $\rho(r)$ is the electronic density, and E^{LSDA} is the standard LSDA functional, the second term is the correction of the correlation energy of Coulomb type described by:

$$\begin{aligned} E^U[\{n^\sigma\}] = \frac{1}{2}\sum_{m\sigma}\{ \langle m, m'|V_{ee}|m', m"\rangle n^\sigma_{mm'} n^{-\sigma}_{m"m'''} - \\ (\langle m, m"|V_{ee}|m, m'''\rangle - \langle m, m"|V_{ee}|m''', m'\rangle) n^\sigma_{mm'} n^\sigma_{m''m'''}\} \end{aligned} \qquad (1.28)$$

Where V_{ee} is the screening Coulomb interactions among the *nl* electrons (*nl* orbitals are considered partially filled), $n^\sigma_{mm'}$ are the density matrix elements defined by **[Anisimov-93]:**

$$n^\sigma_{mm'} = -\frac{1}{\pi}\int^{E_f} I_m\, G^\sigma_{inlm,inlm'}(E)dE \qquad (1.29)$$

With $G^\sigma_{inlm,inlm'}(E) = \langle inlm\sigma|(E-H)^{-1}|inlm'\sigma\rangle$ are the elements of the Green function matrix in this localized representation. Finally the last term in the equation is then subtracted in order to avoid double counting of the interactions part for localized electrons (already included in the LSDA, although in an average manner) is given by:

$$E_{dc}[\{n^\sigma\}] = \frac{1}{2}UN(N-1) - \frac{1}{2}J\left[N^\uparrow\left(N^\uparrow - 1\right) + N^\downarrow\left(N^\downarrow - 1\right)\right] \qquad (1.30)$$

With $N^\sigma = Tr(n^\sigma_{mm'})$ and $N=N^\uparrow+N^\downarrow$. U and J are the screened Coulomband exchange parameters **[Anisimov-97].**

1.3.5 Density Functional Perturbation Theory (DFPT)

Generally, the ground state properties, as the total energy, and forces and stresses are described essentially by the first derivatives of *E*. It can be possible to go further and examine higher derivatives of *E* with respect to ionic positions and lattice parameters, or with respect to macroscopic applied external (typically electric) fields. The formalism which calculates the response functions of a DFT system is known as density functional perturbation theory (DFPT) **[Baroni-87, Giannozzi-91, Gonze-97, Gonze-Lee97]**.

If the perturbation strength is characterized by a parameter λ, then the energy, potentials, and wavefunctions have an expansion as a function of lambda:

$$E = E^{(0)} + \lambda E^{(1)} + \lambda^2 E^{(2)} + \cdots \quad (1.31)$$

The first term of the series represents the standard ground-state energy. If the perturbation λ represents the atomic displacements then the first term corresponds to the forces on the atoms. This term is null at equilibrium. The forces and stresses are in $E^{(1)}$, and many experiments probe $E^{(2)}$, such as Raman and infra-red spectroscopy, linear optics, and elastic constants.

1.4. Numerical implementation of DFT

Different DFT based electronic structure methods can be classified, depending on the representations that are used for density, potential and KS orbitals. Many different choices are made in order to minimize the computational and human costs of calculations, while maintaining sufficient accuracy. A brief summary of the many possibilities to solve the Schrödinger's equation is given in Figure 1.4.

In this work, the calculations have been performed mainly using two approaches, the (linearized) augmented plane wave plus local orbitals ((L)APW+lo) and pseudo-potential plane wave (PP) (plane waves / pseudopotential). In each of these methods, Kohn and Sham orbitals are of the form:

$$\varphi_i(r) = \sum_\alpha c_{i,\alpha} \emptyset_\alpha \quad (1.32)$$

where the φ_α are the basis functions and the $c_{i,\alpha}$ are the expansion coefficients. Given a choice of basis, the coefficients are the only variables in the problem, since the density depends only on the KS orbitals.

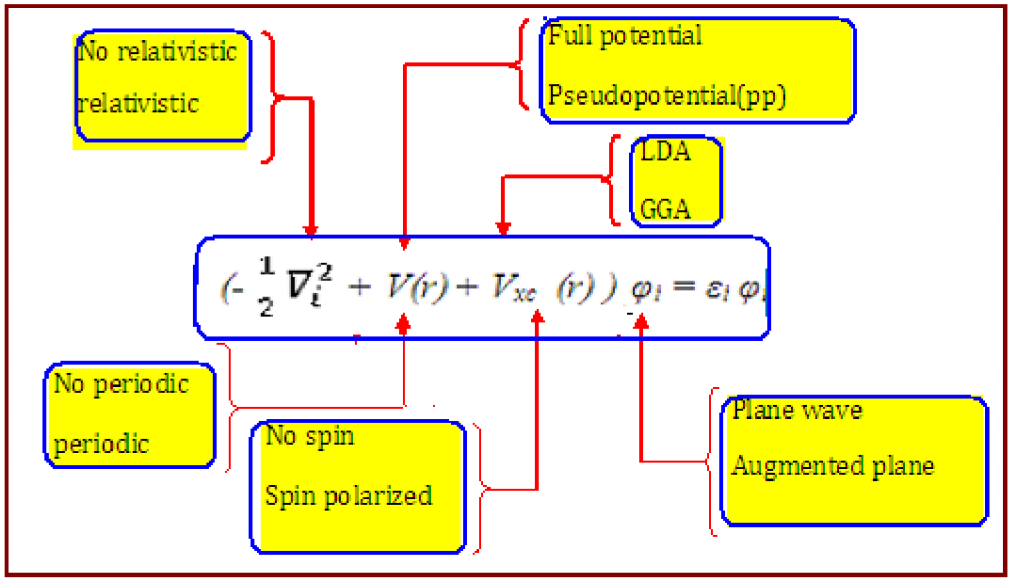

Figure1.4: Schematic representation of various DFT-based methods of calculation.

1.4.1 Bloch's theorem

Bloch's theorem tells how this can be done for a hamiltonian that has a lattice periodicity. The theorem says: Any eigenfunction can be written as a product of a function $u_k(r)$ that has the periodicity of the lattice, and a plane wave e^{ikr}.

$$\varphi_k(r) = e^{ikr} u_k(r) \tag{1.33}$$

k is a vector that is confined to the first Brillouin zone of the reciprocal lattice. $u_k(r)$ has the same periodicity as the direct lattice, has translational symmetry and it can be expressed in terms of a discrete plane-wave basis set with wavevectors $\boldsymbol{G}$ that are reciprocal lattice vectors of the crystal **[kittel-89, Cottenier-02]:**

$$u_k(r+R) = u_k(r)u_k(r) = \sum_G C_G(k-G)e^{iGr} \tag{1.34}$$

Bloch's theorem uses the periodicity of a crystal to reduce the infinite number of one-electron wavefunctions to be calculated to simply the number of electrons in the unit cell of the crystal. Bloch's theorem is of major interest in terms of first calculations for the different operators (matrix form) will be treated in direct space or in reciprocal space as they are diagonal in one or the other, and secondly, by the use of Bloch's theorem, the problem of the infinite number of equations to a single electron can be transformed to problem of a finite number (within the first Brillouin zone) and the description of the system and its study is limited the region of space defined by the unit cell, which in reciprocal space is found at the first Brillouin zone. Solving equations of Kohn and Sham will therefore sampling points k reflecting the symmetry of the first Brillouin zone.

1.4.2. Full-potential linearized augmented-plane-wave method

Among the most accurate schemes for solving the KS equations is the all-electron full-potential linearized augmented-plane-wave (FP-LAPW) method which found its origins in the work of Slater **[Slater-37].** The basic concepts and ideas of LAPW have been presented in various places **[Singh-06, Schwarz-03, Schwarz-02]** so only the main points shall be mentioned here **[Schwarz-10].** For didactical reasons it is advantageous to discuss APW first, before going to its successors LAPW and APW+lo.

1.4.2.1. Augmented plane wave method (APW)

The ideas that lead to the APW basis set is that the region far away from the nuclei, the electrons are more or less `free'. Free electrons are described by plane waves. Close to the nuclei, the electrons behave quite as they were in a free atom, and they could be described more efficiently by atomic like functions. Space is therefore divided now in two regions: around each atom a sphere with radius R is drawn (call it S(r)). Such a sphere is often called a *muffin tin* sphere; the part of space occupied by the spheres is the muffin tin region. The remaining space outside the spheres is called the interstitial region (call it I) [**Cottenier-02].** One augmented plane wave (APW) used in the expansion of φ_I and φ_S are defined as:

$$\begin{cases} \varphi_s(r) = \sum_{lm} A_{lm} u_l^{\alpha}(r, E_l) Y_{lm}(r) \\ \varphi_I(r) = \frac{1}{\sqrt{\Omega}} \sum_G C_G \, e^{i(G+k)r} \end{cases} \quad (1.35)$$

In the above relations, Ω *is* the unit cell volume, r is the position inside sphere, k is a wave vector in the irreducible Brillouin zone (IBZ) and u_{lm} is the numerical solution to the radial Schrödinger equation at the energy E_l.

$$\left[-\frac{d^2}{dr^2} + \frac{l(l+1)}{r^2} + V(r) - E_l\right] r u_l(r) = 0 \quad (1.36)$$

Where V the spherical component of the potential in the sphere and C_G and a_{lm} are expansion coefficients; E_l is a parameter (set equal to the band energy). Inside the MT sphere a KS orbital can only be accurately described if E in the APW basis functions is equal to the eigen-energy *Ei*. Therefore, a different energy-dependent set of APW basis functions must be found for each eigen-energy.

Since the continuity on the spheres boundaries needs to be guaranteed on the dual representation, constraint must be imposed. In the APW method this is done by defining the A_{lm} in terms of C_G in the spherical harmonic expansion of the plane waves.

$$A_{lm} = \frac{4\pi i^l}{\sqrt{\Omega} u_l(R)} \sum_G C_G J_l(|k+g|R) Y_{lm}^*(k+g) \quad (1.37)$$

The orbitals φi (r) of KS are expressed as linear combination of APW wave φ (r). The KS orbital can be accurately described only if E in the basic functions of APW is equal to the eigen-energy *Ei*. Consequently, all the different energy-dependent basis functions are unknown, they must be determined iteratively at each step of the process of self-consistency, which complicates greatly the problem.

1.4.2.2. Linearized augmented plane wave method (LAPW)

Several improvements to solve the energy dependence of the basis set were tried but the first really successful one was the linearization scheme introduced by Andersen **[Anderson-75]** leading to the linearized augmented plane wave method. In LAPW the energy dependence of each radial wave function inside the atomic sphere is linearized by taking a linear combination of a solution u at fixed linearization energy and its energy derivative $\dot{u}$computed at the same energy.

$$\varphi(r) = \begin{cases} \frac{1}{\sqrt{\Omega}} \sum_G C_G \, e^{i(G+k)r} \, r \in I \\ \sum_{lm} [A_{lm} u_l(r, E_l) + B_{lm} \dot{u}(r, E_l)] Y_{lm}(r) \, r \in S \end{cases} \quad (1.38)$$

where the B_{lm} are coefficients for the energy derivative analogous to the A_{lm}. The basis functions inside the spheres are linear combinations of a radial functions $u_l(r)\, Y_{lm}(r)$ and their energy derivatives. The u_l are defined as in the APW method and the energy derivative $\dot{u}_l(r)$ satisfies the following equation:

$$\left[-\frac{d^2}{dr^2} + \frac{l(l+1)}{r^2} + V(r) - E_l \right] r\dot{u}_{lm}(r) = r u_{lm}(r) \quad (1.39)$$

The LAPWs provide a sufficiently flexible basis to properly describe eigenfunctions with eigen-energies near the linearization energy, which can be kept fixed. This scheme allows us to obtain all eigen-energies with a single diagonalization in contrast to APW.

1.4.2.3. Augmented plane wave plus local orbitals method (APW+lo)

Recently, an alternative approach was proposed by Sjöstedt and al. **[Sjöstedt-00],** namely the APW+lo (local orbitals) method. Here the augmentation is similar to the original APW scheme but each radial wave function is computed at a fixed linearization energy to avoid the non-linear eigenvalue problem that complicated the APW method. Thus only the condition of continuity can be required and the basis functions may contain a kink at the sphere boundary.

The missing variational freedom of the radial wave functions can be recovered by adding another type of local orbitals containing a u and $\dot{u}$ term.

$$\varphi(r) = \begin{cases} \sum_{lm} [a_{lm}^{\alpha,lo} u_{lm}^{\alpha}(r) + b_{lm}^{\alpha,lo} u(r)] Y_{lm}(r) & pour \quad r < R_\alpha \\ 0 & r \in I \end{cases} \quad (1.40)$$

The local orbitals are evaluated at the same fixed energy as the corresponding APWs. The two coefficients are determined by the normalization and the condition that the local orbital has zero value at the sphere boundary. In this version, $\dot{u}$ is independent of the PWs, since it is only included for a few local orbitals and not associated with every plane wave. Recently it was demonstrated that this new scheme can reach the same accuracy as LAPW but converges faster in terms of number of PWs **[Madsen-01].** The

highest efficiency was found for a mixed basis set in which the "physically important" *l*-quantum numbers are treated by APW+lo but the higher *l* by LAPW. It was shown in **[Madsen-01]** that quantities such as the total energy, forces converge significantly faster with respect to the number of basic functions than with the pure LAPW procedure but reach the same values.

1.4.2.4. Full potential scheme

Within one calculation a mixed "LAPW and APW+lo" basis can be used for different atoms and even different *l*-values for the same atom **[Madsen and al. 01].** In general one describes by APW+lo those orbitals which converge most slowly with the number of PWs (such as *3d* states) or the atoms with a small sphere size, but the rest with ordinary LAPWs **[userguide-09].**

In its general form the LAPW (APW+lo) method expands the potential in the following form:

$$V(r) = \begin{cases} \sum_{LM} V_{LM}(r) Y_{LM}(r) & inside\ \ sphere \\ \sum_{K} V_{K} e^{iK.r} & outside\ \ \ sphere \end{cases} \quad (1.41)$$

and the charge densities analogously. Thus no shape approximations are made, a procedure frequently called a "full-potential" method.

The FLAPW is a method that has the double advantage of giving a complete description of the potential as well as electrons.

There are a number of computer codes implement this ab initio approximation methods as WIEN2k and Exciting.

1.4.3. Pseudopotential/ plane wave methods

1.4.3.1. Pseudopotential

This method assumes that the physical and chemical properties of a system are essentially governed by the valence electrons, while the ionic cores can be considered "frozen" in their atomic configurations. In the context of the DFT, pseudopotential method involves coupling of plane waves and pseudopotentials. This process appears to be extremely accurate and reasonably fast for solid modeling systems.

One of the main advantages of using a plane wave basis set is that its accuracy can be easily controlled. This is related to the fact that, when using such a basis set, we are making no assumptions about the final shape of the orbitals, other than that there is some scale below which they become smoothly varying. However, this also leads to a major disadvantage of using a plane wave basis set, which is that the size of the basis set required for a given system is often far larger than would be required with a localised basis set. This is because, in condensed matter systems, the orbitals tend to oscillate very rapidly in the vicinity of atomic nuclei, and are much more smoothly varying elsewhere **[Gibson-06].**

A pseudopotential essentially changes part of what the outer, or valence, electrons ``see''. The core electrons, and the potential due to the bare nuclear charge, are replaced by a fictitious potential that is defined such that the behaviour of the valence electrons is not affected outside of some cut-off radius r_c from the nucleus. So long as this radius is not so large that it overlaps regions of space that are involved in chemical bonding, the pseudopotential approximation should not significantly alter the inter-atomic interactions that govern the behaviour of condensed matter.

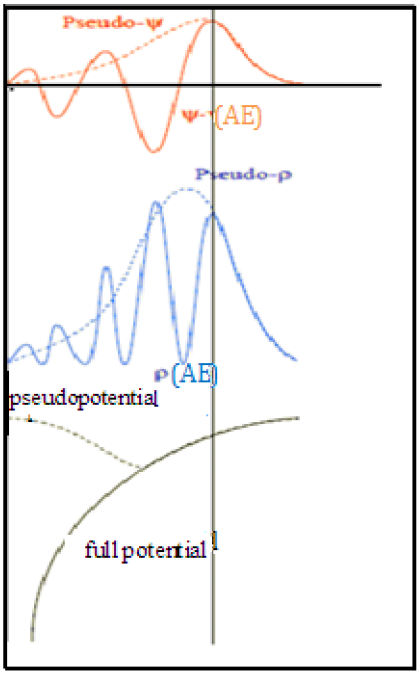

Figure1.5: An illustration of the full all-electronic (AE) wavefunction and electronic potential (solid lines) plotted against distance r, from the atomic nucleus. The corresponding pseudo wavefunction and potential is plotted (dashed lines). Outside a given radius r_c , the all electron and pseudo electron values are identical.

Some criteria to judge whether a particular pseudopotential is good, are: transferability softness and accuracy.

1/ The transferability of the pseudopotential, its ability to accurately describe the valence electrons in different atomic, molecular, and solid-state environments. A transferable pseudopotential gives correct results in a wide variety of environments.

2/A pseudopotential is called "soft" when few plane waves are needed. Making a pseudopotential soft means that it gets tailored for an element in a specific environment.

3/Accuracy: the pseudo-charge density must reproduce the true density as accurately as possible.

The art of creating good pseudopotentials is to find potentials with these criteria. There are essentially two kinds of pseudopotentials, norm-conserving soft pseudopotentials **[Troullier-91]** and Vanderbilt ultrasoft pseudopotentials **[Vanderbilt-90].**

1.4.3.2. Norm-conserving pseudopotentials

Norm-conserving pseudopotentials enforce the condition that, outside of a cutoff radius, the norm of each pseudo-wavefunction be identical to its corresponding all-electron wavefunction, therefore, it is necessary that outside the core region the real and pseudo wavefunctions be identical so that both wavefunctions generate identical charge densities .Generation of a pseudopotential that satisfies:

$$\begin{aligned} \int_0^{r_c} \psi_{AE}^*(r)\,\psi_{AE}(r)dr &= \int_0^{r_c} \psi_{pseudo}^*(r)\,\psi_{pseudo}(r)dr \\ \int_0^{\infty} \psi_{AE}^*(r)\,\psi_{AE}(r)dr &= \int_0^{\infty} \psi_{pseudo}^*(r)\,\psi_{pseudo}(r)dr = 1 \end{aligned} \qquad (1.42)$$

Where $\psi_{AE}(r)$is the all electron wavefunction and $\psi_{PS}(r)$is the pseudo wavefunction, guarantees the equality of the all electron and pseudo wavefunctions outside the core region.

Pseudopotentials of this type are known as non-local norm-conserving pseudopotentials and are the most transferable since they are capable of describing the scattering properties of an ion in a variety of atomic environments.

1.4.3.3. Ultrasoft pseudopotentials

Developed by Vanderbilt in the early 1990 **[Vanderbilt-90],** the ultrasoft pseudopotentials, as the name suggests, attain much smoother (softer) pseudo-wavefunctions so use considerably fewer plane-waves for calculations of the same accuracy. This is achieved by relaxing the norm-conservation constraint, which offers greater flexibility in the construction of the pseudo-wavefunctions. In this scheme the total valence density is partitioned into so-called hard and soft contributions. These methods are implemented in various forms, and many computer softwares can be used mainly in VASP, DACAPO, CASTEP and ABINIT codes.

1.4.4. CASTEP package

The CAmbridge Serial Total Energy Package (CASTEP) is originated from Cambridge University. It was created by Prof. M.C. Payne and it is actually widely used in U.K universities and condensed matter theory communities available from Molecular Simulations. CASTEP is based on DFT and provide a good atomic-level description of all materials. This code is a total-energy code employing pseudopotentials and either the local density approximation (LDA) or generalized gradient approximation (GGA) for electronic exchange and correlation, and plane-waves as a basis set.

1.4.5. WIEN2k package

The WIEN2k package is a computer program written in FORTRAN which performs quantum mechanical calculations on periodic solids. It uses the full-potential (linearized) augmented plane-wave and local-orbitals [FP-(L)APW+lo] basis set to solve the Kohn–Sham equations of density functional theory. WIEN2k is an all-electron scheme including relativistic effects and has many features. WIEN2k was originally developed by Peter Blaha and Karlheinz Schwarz from the Institute of Materials Chemistry of the Vienna University of Technology.

1.5. Applications

1.5.1. LSDA for chromium nitride

Our calculations are performed with the FP-(L)APW+lo method based on DFT and LSDA, as implemented in the WIEN2k code **[Schwarz-02].** The electrons exchange-correlation energy is described by LSDA, for which we adopt the Ceperley-Alder **[Ceperly-80]** forms and parametrization of Perdew and Wang **[Perdew-92].** Note that the spin-polarized calculations are achieved with two different spin-up and spin down densities and two sets of Kohn-Sham single particle equations are solved self-consistently. We employ the semi-relativistic approximation without spin-orbit effects for all valence states (including the Cr-3d states).

The band structures of majority and minority spin populations are shown in Fig. 1.6 of the hypothetical zincblende ferromagnetic CrN compound. The spin-up and spin-down Cr e_g states are occupied. The spin-up Cr t_{2g} state is only partially occupied. The Cr *d* state in the T_d symmetry is split into a triply degenerated state t_{2g} and a doubly degenerated e_g state. The t_{2g} state is higher than the e_g state and couples with the anion N *p* state **[Nkanoun-bouayed08]**.

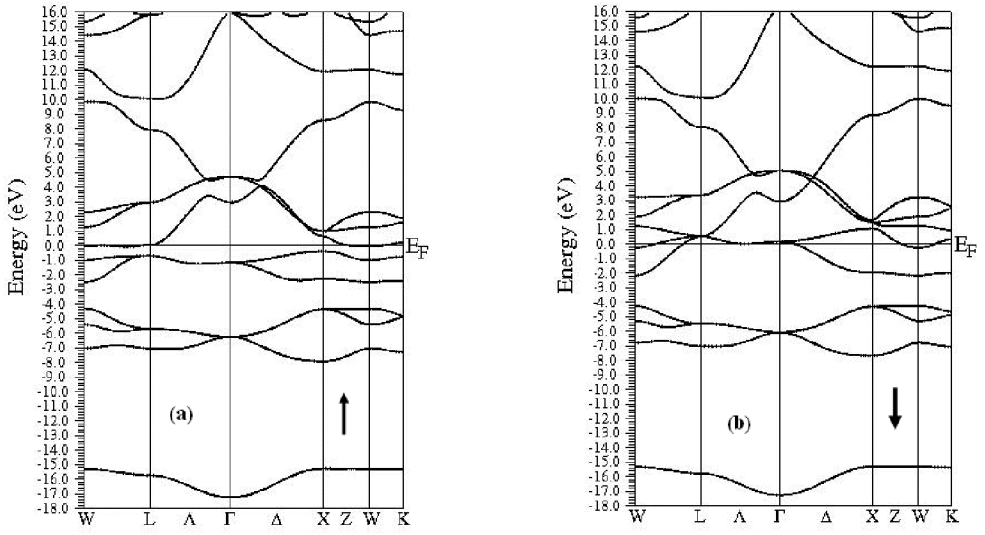

Figure 1.6: Band structure for the ferromagnetic CrN ((a) spin up, (b) spin down) in the hypothetical zincblende structure.

1.5.2. LDA+*U* approach for europium nitride

In this case, we use the spin-polarized DFT using the FP-(L)APW+lo method within the WIEN2k software package**[Schwarz-02].** The exchange-correlation energy of electrons is described by LDA or GGA with the most popular scheme of Perdew, Brouke and Ernzerhof (PBE) **[Perdew-96]** and the new one of Wu and Cohen (WC) **[Wu-06].** We employ the semi-relativistic approximation without spin-orbit effects for all valence states (including the Eu-d and *f* states). For EuN, we have adopted the values of 2.45 and 1,7 Bohr for Eu and N. In the following calculations, the FP-(L)APW + lo basis set consists of $4f^7$ $5d^{10}$ and $6s^2$ orbitals of Eu, and $2s^2$and $2p^3$ orbitals of N. In this approach, the wave function, charge density and potential are expanded differently in two regions of the unit cell.

We use the approach LDA+U which explicitly includes the term of Coulomb in the conventional Hamiltonian. As there are several schemes, we choose the scheme introduced by Anisimov et al. **[Anisimov-91, Anisimov-93]** which is based on the correction self-interaction (SIC). This application requires the introduction of two parameters: *U*, the Hubbard parameter, which is the term of electronic correlation of Coulomb and J is the parameter which makes the interatomic average of exchange. For binary compound EuN, we have adopted 7.397eV for U_{eff} =U - J **[Larson-93].**

The fundamental properties are obtained from optimization curves, giving the variation of the total energy versus the volume for EuN. From optimization, we have calculated the lattice parameter, Bulk modulus as well as its pressure derivative, using Murnaghan equation of state **[Murn-44].** In Table 1.1, we report the theoretical results obtained using LDA, GGA (PBE and WC), LDA+U, GGA+U (PBE and WC), compared to the available experimental data **[Suehiro-04]).** We can see from the table 1.1 that calculations obtained by pure LDA underestimate in a significant way the lattice parameter whereas calculations of GGA-PBE over-estimate the cell parameter in comparison with the experimental data **[Suehiro-04].** Furthermore, we notice that the GGA-WC calculations significantly improve the lattice parameter between the LDA and the GGA-PBE approximations. In the other hand, the existence of *f*-electrons in Eu, we apply both of approximations LDA+U and GGA+U. By analyzing more carefully the reported results of Table 1.1, we can see that the introduction of the parameter U in LDA and GGA (PBE and WC) calculations does not lead to a significant improvement of lattice

parameter value. Moreover, the calculated bulk modulus is in good agreement with the experimental data. GGA+U (PBE) calculations always over-estimate the cell parameter and underestimate the bulk module, which suggests that they are in slight agreement with the experiment than calculations obtained by LDA+U. When we compare the results obtained by LDA and GGA with those of LDA+U and GGA+U, we have observed that the corrections due to the U parameter do not improve the value of lattice parameter. This result was also observed in former calculation done in rare-earth nitrides using the full potential method FP-LMTO **[Larson-93].**

Table 1.1: Calculated equilibrium parameters, bulk modulus and pressure derivative of bulk modulus for EuN compared with available experimental data **[Suehiro04].**

	LDA	GGA (PBE)	GGA (WC)	LDA+U	GGA+U (PBE)	GGA+U (WC)	Expt.
a (Å)	4.027	5.053	4.982	4.924	5.05	4.97	5.00
B (GPa)	143.5	115.49	132.07	145.0	114.71	133.79	-
B'	4.425	4.604	4.429	4.804	3.983	4.476	-

We have calculated the band structure of EuN in ferromagnetic state by means of LDA and LDA+U. Figures 1.7 show the corresponding band structure (majority and minority spin respectively), according to the high symmetries directions in the Brillouin zone. We can see that the application of LDA+U induce some modifications to the levels of the *f* states in the band structure compared to the LDA, in particular on the energy levels of the occupied and unoccupied 4*f* states. Indeed, in the band structure calculated by the LDA (see fig. 1.7), the occupied states Eu-*4f* are situated approximately at 0.4 eV below the Fermi level *(E_F)* in hybridization with the N-2*p* states, whereas the unoccupied states 4*f* are located nearly 4 eV above the E_F, in hybridization with the Eu-5*d* states. Moreover, the LDA calculation does not give the correct binding energies of the *4f* energy levels. This problem is solved by the application of the LDA+U (Fig.1.7). In fact, the unoccupied *4f* states remain around 9 eV above the E_F level and the occupied states *4f* are nearly 1.44 eV below the Fermi level.

To obtain a deep description of electronic bands, we display in figure 1.8, curves corresponding to total and local densities of states (TDOS and LDOS respectively). We can notice, the calculated TDOS corresponding to LDA and LDA+U have a similar aspect except for the position of the *f*-states of Eu. In the TDOS calculated by LDA, we observe only one intense peak whereas with the introduction of the Hubbard term *U*, the f-states are represented by several peaks, which correspond to the electronic nature of these states. Furthermore, we observe three bands; the deeper one is relative primarily to the *5p* states of the rare earth. The second band is situated near the Fermi level and presents a result of hybridizations. The third band, which is slightly deeper corresponds to the states 2*s* of nitrogen atom. Moreover, when we observe the LDOS curves, the bands located under the Fermi level correspond to *p* states of N with a substantial hybridization with the *f* states of Europium **[Bouayed-Kanoun-08, Bouayed-Kanoun-09].**

We find a global magnetic moment of 6.0 μ_B per cell. As expected, the Eu atom is found to be the main contributor to the magnetic moment of the ferromagnetic structure, having a localized magnetic moment of 6.116 μ_B per atom. The nitride neighbors of Eu together make a much larger contribution of -0.297 μ_B, while the interstitial region contributes with 0.182 μ_B to the magnetic moment.

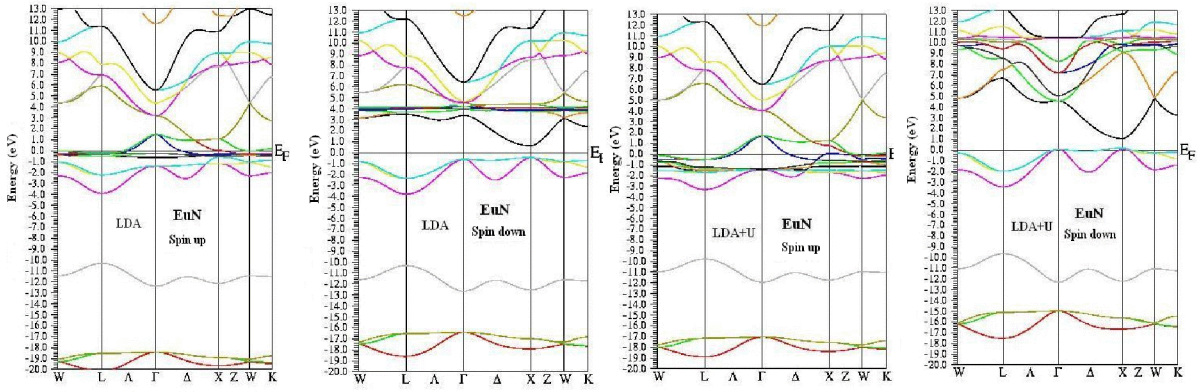

Figure 1.7: Calculated spin-polarized band structure corresponding to LDA and LDA+U calculations.

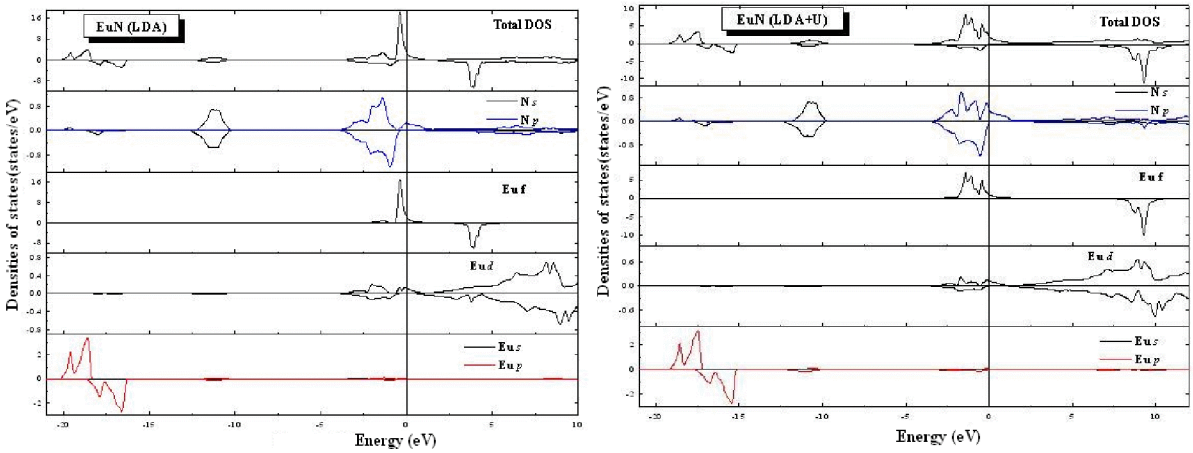

Figure1.8: Total and partial densities of states in EuN with LDA and LDA+U calculations. Majority (upper part) and minority (lower part). The vertical dash line denotes the Fermi level.

Conclusion

In this chapter we discussed the important theoretical formulation of density functional theory. We have shown in different section the obvious role of the electronic density in determination of the physical properties. The main goal of this section was to provide the reader by the important steps in the foundation of the DFT. The calculations performed are performed on two types of codes: CASTEP and WIEN2k.

References

[Anderson-75] O. K. Andersen, Phys. Rev. B, 12, 3060(1975).

[Anisimov-91] V.I. Anisimov, J. Zaanen and O.K. Andersen, Phys. Rev. B 44, 943 (1991).

[Anisimov-93] V.I. Anisimov, I.V. Solovyev, M.A. Korotin, M.T. Czyzyk, and G.A. Sawatzky, Phys.Rev. B 48, 16929 (1993).

[Anisimov-97] V. I Anisimov, F.Aryasetiawan and A. I. Lichtenstein, Phys.: Condens. Matter **9,** 767(1997).

[Arras-10] E. ARRAS, «*Étude théorique de la structure et de la stabilité des alliages GeMn dans le cadre de la spintronique*» 2010, PhD, Université de Grenoble.

[Baroni-87]S. Baroni, P. Giannozzi, and A. Testa. Phys. Rev. Lett. 59, 2662(1987).

[Born-27] M. Born and J. R. Oppenheimer, Ann. Physik 389, 457 (1927).

[Bouayed-Kanoun-08]N. Kanoun-Bouayed and S. Goumri-Said, "*Electronic and magnetic structure of rare-earth nitrides using the LDA+U approach: EuN and GaEuN*"**,** chapter 2 p. 9, Ed. By Transworld Research Network, 2008; ISBN: 978-81-7895-365-6.

[Bouayed-Kanoun-09] N. Kanoun-Bouayed, S. Goumri-Said, A. E. Merad, and M. B. Kanoun, Materials Science Forum 609, 167 (2009).

[Capelle-03] K. Capelle, *Brazilian J. of Physc.*36, 1318 (2006).

[**Ceperly-80**] D. Ceperly and B.J Alder, Phys. Rev. Lett, 45, 4264 (1980).

[Cococcioni-05]M. Cococcioni and S. de Gironcoli, Phys. Rev. B 71, 035105 (2005)

[Cottenier-02] S. Cottenier, *"Density Functional Theory and the family of (L)APW-methods: a step-by-step introduction"* (K.U.Leuven, Belgium), 2002, ISBN 90-807215-1-4

[Dirac-30]P. A. M.Dirac, "*Note on exchange phenomena in the Thomas-Fermi at*om". Proc. Cambridge Phil. Roy.Soc.26, 376 (1930).

[**Fermi-28**] E. Fermi, Z. Phys. 48, 73 (1928).

[Giannozzi-91] P. Giannozzi, S. de Gironcoli, P. Pavone, and S. Baroni. Phys. Rev.B43, 7231(1991).

[Gibson-06]M. C. Gibson;"*Implementation and Application of Advanced Density functionals*", 2006, PhD, University of Durham.

[Gonze_Lee-97] X. Gonze and C. Lee. Phys. Rev. B 55,10355(1997).

[Gonze-97] X. Gonze, Phys. Rev. B 55, 10337(1997).

[Hedin-71] L. Hedin, and B. I. Lundqvist, J. Phys. C: Solid St. Phys. 4, 2064 (1971).

[**Hohenberg-64**] P. Hohenberg, and W. Kohn, Phys. Rev. 136, 3 (1964).

[Hubbard-64] J. Hubbard, Proc. R. Soc. A 276, 238 (1963); Proc. R. Soc. A 277, 237(1964); Proc. R. Soc. A 281, 401 (1964).

[kanoun-08]M.B. kanoun, N. kanoun-bouayed and A.E. Merad, "*Theoretical investigation of electronic structure and magnetic properties of ferromagnetic $Al_{1-x}Cr_xN$ alloys*", chapter 3 p. 23, Ed. By Transworld Research Network, 2008; ISBN: 978-81-7895-365-6.

[kittel-89]C. kittel, « *Introduction à la physique de l'état solide* ».Ed.Dunod, Paris 1998.

[Kohn-65] W. Kohn and L. J. Sham. *Phys. Rev.*, 140(4A), A1133(1965).

[Kohn-65] W. Kohn and L. J. Sham. *Phys. Rev.*, 140(4A):A1133 (1965).

[Kohn-99] W. Kohn. *Rev. Mod. Phys.*, 71, 1253 (1999).

[Larson93]P. Larson and W.R.L. Lambrecht, A. Chantis and M. van Schilfgaarde, Phys. Rev. B 75,045114(1993).

[Lichtenstein-95]A.I. Lichtenstein, V.I. Anisimov and J. Zaanen, Phys. Rev. B 52, R5467 (1995).

[Madsen-01] G.K.H. Madsen, P. Blaha, K. Schwarz, E. Sjöstedt, and L. Nordström, Phys. Rev. B 64, 195134 (2001).

[Murn-44]F.D. Murnaghan, Proc. Nat. Acad. Sci. U.S.A. 30 (1944) 244.

[Nawel-07] N. Kanoun-Bouayed «*Etude théoriques de convergence et applications des approximations quantiques sur les systèmes à différentes configuration électroniques* » 2007, Magister,Université de Tlemcen.

[Perdew-92]J. P. Perdew, Y. Wang, Phys. Rev. B 45, 13244 (1992).

[Perdew-96]J. P. Perdew, K. Burke, and M. Ernzerhof, Phys. Rev. Lett. , 77, 18 (1996)

[Perdew-99]J. P. Perdew, S. Kurth, A. Zupan and P. Blaha, Phys. Rev. Lett. 82, 2544 (1999).

[Pople-99] J. A. Pople,*Rev. Mod. Phys.*, 71, 1267 (1999).

[Renold-03]S. Renold "*First-Principles Studies of Local Electronic and Magnetic Properties in Cuprates*", 2003, PhD, University of Zurich.

[Roquefelte-01] X. Rocquefelte, "*Modélisation du comportement électrochimique de matériaux pour batteries au lithium à partir de calculs de premiers principes*", 2001, PhD,Université de Nante.

[Schwarz-02] K. Schwarz, P. Blaha and G.K.H. Madsen, Comput. Phys. Commun. 147, 71 (2002).

[Schwarz-03] K. Schwarz and P. Blaha, Comput. Mater.Sci. 28, 259 (2003).

[Schwarz-10]K. Schwarz, P. Blaha and S.B. Trickey, Molecular Phys. 108,3147(2010)

[Sing-94]D.J.Singh, *Planewaves, "Pseudopotentials and the LAPW method"*, (Kluwer Academic Publishers, Boston, 1994, ISBN 0-7923-9421-7).

[Singh-06] D.J. Singh and L. Nordstrom, Plane Waves, Pseudopotentials and the LAPW method, 2nd ed. (Springer, New York, 2006), ISBN 10:0-387-28780-9.

[Sjöstedt-00] E. Sjöstedt, L. Nordström, and D.J. Singh, Solid State Comm. 114, 15 (2000).

[Slater -37] J. C. Slater, Phys. Rev. 51,840(1937)

[Slater-64]J.C. Slater, "*Quantum Theory of Matter*", 2nd edition McGraw-Hill 1964).

[Solovyev-94]I.V. Solovyev, P.H. Dederichs, and V.I. Anisimov, Phys. Rev. B 50, 16861 (1994).

[Suehiro-04]T. Suehiro, N. Hirosaki, Y. Yamamoto, T. Nishimura, and M. Mitomo, J. Mater. Res.19, 959(2004).

[**Thomas-27**] L.H. Thomas, Proc. Cambridge, Philos. Soc. 23, 542 (1927).

[Troullier-91] N. Troullier and J. L. Martins. Phys. Rev. B, 43, 1993 (1991).

[Vanderbilt-90] D. Vanderbilt. Phys. Rev. B, 41, 7892 (1990)

[VonBarth-72]U. Von Barth and L. Hedin, J Phys. C 5, 1629 (1972)

[**Wigner-34]** E. Wigner, Phys. Rev. 46, 1002 (1934).

[Wu-06]Z. Wu and R. E. Cohen, Phys. Rev. B 73, 235116 (2006).

Chapter two

Copper Nitrides

Abstract

This chapter is devoted to the investigation of physical quantities that can actually be calculated using density functional theory performed on Copper Nitrides compounds. Indeed, we report plane-wave pseudo-potential ab-initio calculations in order to investigate the structural parameters, elastic constants, bonding properties and polycrystalline parameters of CuN in zincblende, rocksalt and fluorite structures. We pay more attention to the electronic properties and bonding characteristics and their relation to the possible covalent/ionic bonding characters in copper nitrides compounds.

« Que la stratégie soit belle est un fait, mais n'oubliez pas de regarder le résultat »

Winston Churchill

2.1. Introduction

Transition metal nitrides attract considerable interest for their properties and potential technical applications **[Pierson-96-Zerr-03]**. Both theoretical and experimental efforts have gone into studying the early transition metal nitrides **[Kroll-03, Wu-05, Grossman-99, Jin-05, Zhan-03, de Paiva-07, Mattesini-03, Kanoun-07]**. The 4*d* and 5*d* series of late transition metals Ru, Rh, Pd, Ag, Os, Ir, Pt, and Au, also known as noble metals, are generally considered not to form nitrides **[Pierson-96]**, although Cu_3N and Cu_3MN have been reported **[Moreno-04, Moreno-07]**. Despite the wide interest in making ever better nitrides for applications, the noble metal nitrides have evaded discovery until the recent synthesis of gold **[Krishnamurthy-04]**, and platinum nitrides. In fact, the recent highest pressure of a new material, PtN, was synthesized and recovered in zincblende structure back to atmospheric pressure, by Gregoryanz and al. **[Gregoryanz-04]**. As for theoretical progress, *ab initio* quantum mechanical calculations of the atomic and electronic structures allow the theoretical modelling of new materials permitting their properties to be predicted, and suggesting new syntheses. In fact the structural and electronic properties of cubic PtN have been extensively studied using various theoretical calculations **[Kanoun-05–Zhang-09].** Young and al **[Yu-06]** have performed first-principles calculation and experimental studies of PtN, finding its structure to be elastically unstable. A fluorite-type structure was therefore suggested with a composition of PtN_2 **[Yu-06]**. These explorations motivated us to study theoretically different crystal structures of copper nitrides as possible candidates as hard noble metals. In particular, we are interested in studying the compound with 1:1 stoichiometric ratio of Cu:N and fluorite structure CuN_2.

2.2. Crystal structure description

We consider three possible phases for copper nitrides: ZB (space group F43m), RS (space group Fm3m), and fluorite C1-like structure (space group Fm3m). ZB, RS and C1 phases consist of three lattice constants of the conventional unit cell *a*, *b*, and *c*. The basis consists of a copper atom at (0, 0, 0) and nitrogen at $(\frac{1}{\alpha})(1, 1, 1)$, where $a = b = c$. The first and third phases have $\alpha = 4$, while the second has $\alpha = 2$. For the crystal structure of fluorite-type structure, the copper atoms form a face-centered cubic (fcc) lattice, while nitrogen atoms occupy all of the tetrahedral interstitial sites.

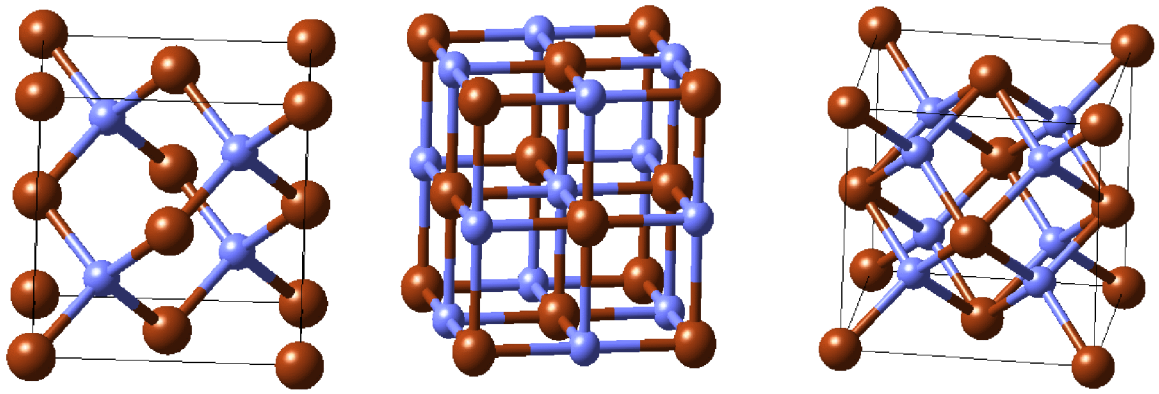

Figure2.1: Zincblende structure, rocksalt structure and fluorite structure

2.3. Method of calculation and computational details

Our calculations use first-principles total energy calculations based on DFT applying the generalized gradient approximation (GGA) using the scheme of Perdew, Brouke and Ernzerhof **[Perdew96]** and also tools specific to CASTEP code **[Segall-02–Milman-00]**. These include norm-conserving and ultra-soft pseudopotentials (UPP) **[Vanderbilt-90],** a plane wave (PW) basis set, and use of k-point sampling techniques and the Broyden-Fletcher-Goldfarb-Shanno (BFGS) scheme for optimizing geometry, etc. Major advantages of the PW based approach are: the ease of computing forces and stresses; good convergence control with respect to all computational parameters employed; favorable scaling with the number of atoms in the system and the ability to make cheaper calculations by neglecting core electrons. Our calculations used the valence electron sets but employed an UPP representation to describe the core electrons. For our systems we use PW cut-off energy of 320 eV, with a Monkhorst-Pack k-point mesh in the Brillouin zone **[Vanderbilt-90]** about 10×10×10 for ZB and RS-CuN and with 9×9×9 for CuN_2. The convergence is assumed when the forces on atoms are less than 0.03 eV/Å. *Mulliken* charges and bond populations where calculated by projecting the PW Kohn-Sham eigenstates onto the atomic basis sets.

2.4. Structure and elastic constants

The equilibrium lattice parameters and the bulk modulus, listed in Table 2.1 for CuN in the ZB, RS, and fluorite structures, were calculated using PP-PW and FP(L)APW+lo. We have obtained larger lattice parameters for the C1 type than those

reported for the ZB and RS types. This result seems reasonable because, in C1-type structure, the nitrogen atoms all occupy the tetrahedral interstitials of the copper sublattice. The octahedral interstitials are left empty because nitrogen atoms are too small to be stabilized in the octahedral interstitials of the noble nitrides. The lattice constant of the RS structure is smaller, but close to the ZB structure's one. Although the nitrogen atoms fill the same face-centered-cubic lattice formed by the metal atoms in the RS and ZB structures, the volume of the octahedral interstitial sites (where nitrogen atoms reside in the RS structure) is larger than that of the tetrahedral interstitial sites (occupied by nitrogen in the ZB structure). When we compare our results for CuN to pure fcc-Cu (a_0 = 3,615 Å, B = 133 GPa **[Sigalas-92]**), we observe that alloying copper with nitrogen makes the nitride harder than the metal. Thus, the copper nitride phases are less compressible than the pure metal.

In order to complete the mechanical stability description of these systems, we obtain a set of zero-pressure elastic constants from the resulting change in total energy on the deformation. The elastic constants C_{ij} were calculated within the total-energy method, where the unit cell is subjected to a number of finite-size strains along several strain directions. Cubic lattices have three independent elastic constants **[Nye-85]**, namely, C_{11}, C_{12}, and C_{44}. These constants obey the following relations:

$$B = \frac{1}{3}(C_{11} + 2C_{12}) \tag{2.1}$$

$$C_r = C_{44} \tag{2.2}$$

$$C_s = \frac{1}{2}(C_{11} - C_{12}) \tag{2.3}$$

Where B is the isotropic bulk modulus, C_r is the resistance to shear deformation across the [100] plane in the [010] direction, and Cs is the shear modulus across the [110] plane in the [1-10] direction. The obtained elastic stiffness constants Cij are gathered in Table 2.1. Furthermore, the mechanically stable phases or macroscopic stability is dependent on the positive definiteness of stiffness matrix **[Fedorov-68]**. For a stable cubic structure, the independent elastic constants should satisfy the well-known Born-Huang criterion **[Born-82]**, given by: $C_{44} > 0$, $C_{11} > |C_{12}|$ and $C_{11}+2C_{12} > 0$. It can be seen that the CuN in ZB, RS and C1 phases are mechanically stable because all elastic constants are positive and satisfy the Born mechanical stability restrictions.

To ascertain the stiffness of the solid, we compute Young's modulus, the ratio between linear stress and strain. Young's modulus can be calculated from Hill's **[Hill-52]** shear (G) and bulk modulus through the following equation:

$$Y = \frac{9BG}{3B+G} \tag{2.4}$$

The value of G has been obtained by taking the arithmetic mean of the computed Reuss (R) **[Reuss-29]** and Voigt (V) **[Voigt-28]** approximations:

$$G = \frac{G_R+G_v}{2} \tag{2.5}$$

$$G_R = \frac{5(C_{11}-C_{12})C_{44}}{4C_{44}+3(C_{11}-C_{12})} \tag{2.6}$$

$$G_v = \frac{C_{11}-C_{12}+3C_{44}}{5} \tag{2.7}$$

Then, Poisson's ratio v was obtained for polycrystalline compound species from B and G_V as:

$$v = \frac{3B-2G_v}{2(3B+G_v)} \tag{2.8}$$

Our calculated values for bulk modulus, shear modulus, Young's modulus, and Poisson's ratio of all structures are summarized in Table 2.1, within the Voight-Reuss-Hill bounds **[Fedorov-68]**. The shear modulus of the RS phase is evidently higher than those for the C1 and ZB phases. The larger shear and Young's moduli are mainly due to its larger value for C_{44}. Moreover, our computed Poisson's ratio of the RS phase is considerably smaller than the C1 and ZB phases. The smaller value of Poisson's ratio indicates that the RS phase is relatively stable against shear; a stronger degree of covalent bonding results in the higher hardness. In fact, Poisson's ratio can formally take values between -1 and 0.5, which correspond, respectively, to the lower bound where the material does not change its shape and to the upper bound when the volume remains unchanged. It has been proved that v= 0:25 is the lower limit for central-force solids and 0.5 is the upper limit, which corresponds to infinite elastic anisotropy **[Ledbetter-83]**. All the calculated Poisson's ratio values are larger than 0.25, which means that CuN phases are affected by central contributions. The elastic anisotropy of crystals has an important implication in engineering science since it is highly correlated with the possibility to induce microcracks in the materials **[Tvergaard-88]**. The anisotropy factor for cubic crystals **[Karki-97]** is given by:

$$A_{an} = \frac{2C_{44}+C_{12}}{C_{11}} \quad (2.9)$$

In addition, this factor may provide insight on the elastic anisotropy of the present CuN phases. The shear anisotropic factors obtained from our theoretical studies are given in Table 2.1. For a completely isotropic material, that is when Cr = Cs, the A factor takes the value of 1, while values smaller or greater than unity measure the degree of elastic anisotropy. It is interesting to note that our calculations give values close to unity for the RS phase: a characteristic of highly isotropic systems. This is further confirmed by the fact that G ≈C_{44}. On the other side both ZB and C1 phases are showing a certain amount of elastic anisotropy, which might lead to a higher probability to develop microcracks or structural defects during the growing process.

Table 2.1: Calculated equilibrium parameters a(Å),elastic constants C_{ij} (GPa), Bulk modulus B (GPa), Shear modulus G (GPa), Young's modulus Y (GPa), and Poisson's ratio v. The calculated density ρ (g/cm3), longitudinal, transverse and average sound velocity (v_l, v_t, v_m in km/s), and Debye temperatures θ_D (K) are also shown.

	CuN (ZB)	CuN (RS)	CuN_2 (Fluorite)
a	4.336	4.078	4.694
	(4.341)[a]	(4.074)[a]	
C11	293.55	340.0	292.14
C12	219.63	191.0	242.34
C44	73.16	72.80	62.36
B	244.27	240.66	258.94
G	55.623	73.475	43.154
Y	155.096	200.066	122.648
v	0.394	0.361	0.421
A	1.246	0.990	1.256
ρ	6.305	7.580	5.870
v_t	2.970	3.113	2.711
v_l	7.106	6.684	7.342
v_m	3.360	3.506	3.078
θ_D	732.592	812.901	620.058

[a]reference **[Kanoun-07]**

One of the most important parameters determining the thermal characteristics of materials is the Debye temperature (θ_D). As a rule of thumb, a higher Debye temperature

implies a higher associated thermal conductivity. The knowledge of such a numerical figure is essential for developing and manufacturing electronic devices. At low temperatures, the vibrational excitations arise solely from acoustic vibrations. Therefore, the Debye temperature calculated from elastic constants at low temperatures is the same as that determined from specific heat measurements. In order to estimate Debye temperature, we used the simple Debye-Grüneisen model. The Debye temperature can be defined in terms of the mean sound velocity and gives explicit information about lattice vibrations **[Ibrahim-88]**. It can be determined from the following equation **[Anderson-63]**:

$$\theta_D = \frac{h}{k_B}\left[\frac{3n}{4\pi}\left(\frac{N_A\rho}{M}\right)\right]^{\frac{1}{3}} V_m \tag{2.10}$$

Where h is Planck's constant, k_B is Boltzmann's constant; N_A is Avogadro's number, ρ the density, M the molecular weight, n the number of atoms in the unit cell, and v_m the mean sound velocity given by the following relations:

$$V_l = \sqrt{\left(\frac{3B_{VRH}+4G_{VRH}}{3\rho}\right)} \tag{2.11}$$

$$V_t = \sqrt{\left(\frac{G_{VRH}}{\rho}\right)} \tag{2.12}$$

$$V_m = \left[\frac{1}{3}\left(\frac{2}{V_t^3}+\frac{1}{V_l^3}\right)\right]^{-\frac{1}{3}} \tag{2.13}$$

Where v_l and v_t are longitudinal and transverse elastic wave velocity of the polycrystalline materials and can be obtained using the polycrystalline shear modulus and bulk modulus from Navier's equation **[Schreiber-73]**. The calculated Debye temperatures are listed in Table 2.1. Our model predicts a relative high θ_D value, indicating a rather stiff lattice and therefore good thermal conductivity. The progressive decrease of mean sound velocities in the RS→ZB→C1 phases further explains the proneness of lowering Debye temperatures along the same sequential order. Further properties depending on temperature will be given in the last section.

2.5. Electronic properties

For a detailed description of electronic properties using the GGA, Fig. 1a, 1b and 1c shows the total (TDOS) and local densities of states (LDOS) for the ZB, RS, C1 phases, respectively. We can decompose the LDOS into three energy regions: (i) the lowest

region stemming mainly from *N-2s* states; (ii) the region at the bottom of the valence band complex dominated by occupied *3d* noble metal states; (iii) the upper region of the valence-band complex cut by E_F and mainly due to *Cu-3d* states mixed with *N-2p* states. It can be observed that the *N-2p* states hybridize strongly with the *Cu-3d* states. We can thus consider that two main factors are at origin of the electronic structure of the cubic copper nitride compounds. The first factor is the expansion of the face-centered-cubic lattice compared to the pure Cu lattice due to the insertion of the nitrogen atoms at the tetrahedral interstitial sites. The second factor is the interaction between the *Cu-3d* electrons and the *N-2p* electrons.

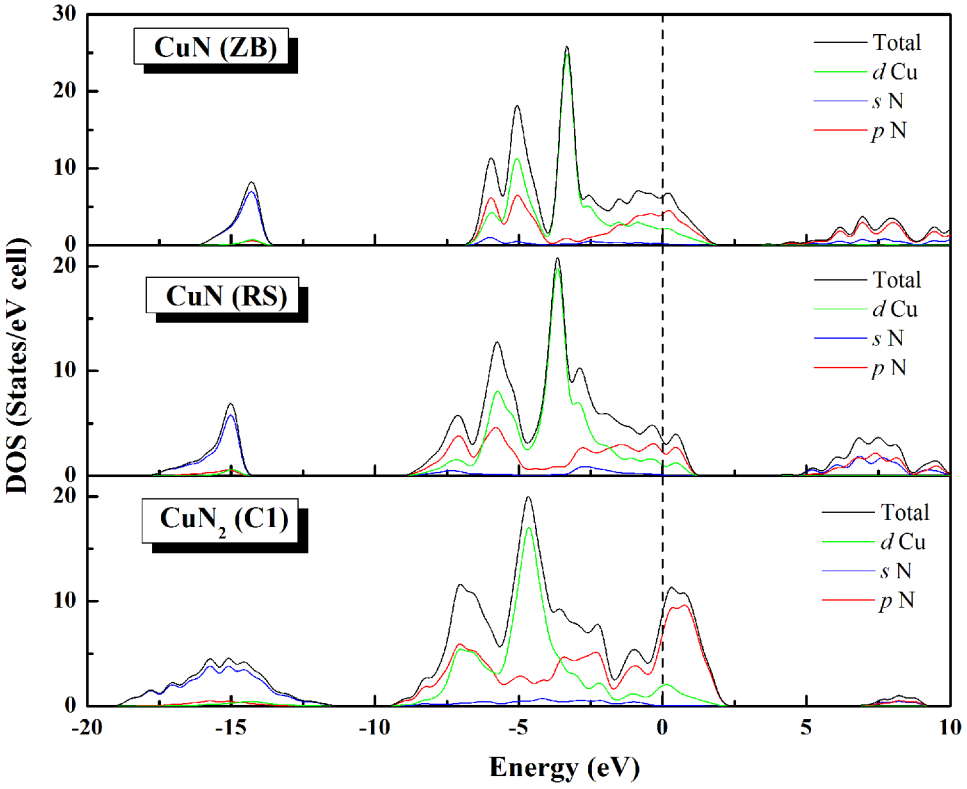

Figure 2.2: TDOS and LDOS for copper nitrides (a) ZB, (b) RS and (c) C1 phases. The vertical dot line denotes the Fermi level.

2.6. Bonding characteristics

2.6.1. Mulliken population

In order to obtain a deeper insight into the bonding character, we calculate the *Mulliken* population. Table2.2 shows the orbital charges and the effective valence of both Cu and N species for the phases under consideration. The effective valence for the Cu cation is +0.36, +0.38 and +0.23 in the ZB, RS and C1 phases respectively. These values are representative of the concurrent ionic and covalent bonding confirming a part of results of the previous calculations with full potential *ab initio* calculations **[Kanoun-07]**. Although it is difficult to put a figure on the level of iconicity and covalency using the effective valence concept, the type of bonding and its level can be determined by calculating the *Mulliken* bond population as reported in Table2.3. We can see that the bond population and bond length (mainly Cu-N) for the ZB are in the same order of those of RS. Compared to the C1 phase, the bond population decreases although the bond length still of the same order of those of the ZB and RS phases. It is important to notice that a high positive bond population indicates a high degree of covalency in the bond, and positive and negative values indicate bonding and anti-bonding states respectively. From our results, the negative values (and then the anti-bonding states) are found in the C1 phase, between the nitrogen atoms. If we compare the bond population of all three phases, we can conclude that ZB is the most covalent, followed by RS and C1 phases.

Table2.2: Atomic *Mulliken* charges in copper nitrides calculated from PW pseudo-potential calculations.

Phases	Species	s	p	d	Total (e)	Charge (e)	Effective Charge(e)
CuN (ZB)	Cu	0.49	0.53	9.35	10.36	0.64	0.36
	N	1.77	3.87	0.00	5.64	-0.64	
CuN (RS)	Cu	0.48	0.52	9.39	10.38	0.62	0.38
	N	1.78	3.84	0.00	5.62	-0.62	
CuN_2 (C1)	Cu	0.47	0.47	9.29	10.23	0.77	0.23
	N1	1.90	3.49	0.00	5.39	-0.39	
	N2	1.90	3.49	0.00	5.39	-0.39	

Table2. 3: *Mulliken* Bond populations and Bond lengths in copper nitrides calculated from PW pseudo-potential calculations.

Phases	Bond	Bond population	Bond length [Å]
CuN (ZB)	N – Cu	1.54	1.9172
	N - N	-	3.1445
CuN (RS)	N - Cu	1.45	2.0905
	N - N	-	2.960
CuN2 (C1)	N1 - Cu	0.78	2.0675
	N2 - Cu	0.78	2.0675
	N1 - N2	-0.28	2.3874

2.6.2. Electronic localized function

To further elucidate the nature of chemical bonding, we have calculated the electronic localized function (ELF) **[Burnus-05]** using the Exciting code **[Silvi-94]**. The ELF has proven to be a useful companion to the density in the task of providing us with insightful intuition on the electronic structure. In fact, when ELF = 1, it corresponds to perfect electron localization. In Figure 2.3, we sketch the ELF 3D contours and gave specific bond lengths of CuN in ZB, RS and C1structures. It is clear that the Cu-N bonds are stronger than N-N bonds for CuN in ZB, RS and C1. On the other hand, for the C1, the ELF analysis indicates that the Cu-N bonds are considerable weaker than of the ZB and RS structures (thus a much lower C_{44} value for the C1 structure). The ELF contours reveals areas with a considerable charge accumulation (at nitrogen sites) and dissipation (at Cu sites) as to indicate that charge transfer is not a negligible effect in CuN for ZB, RS and C1 structures. Most of the electronic charge transferred to the nitrogen atoms comes from regions where the covalent Cu-Cu interactions are taking place.

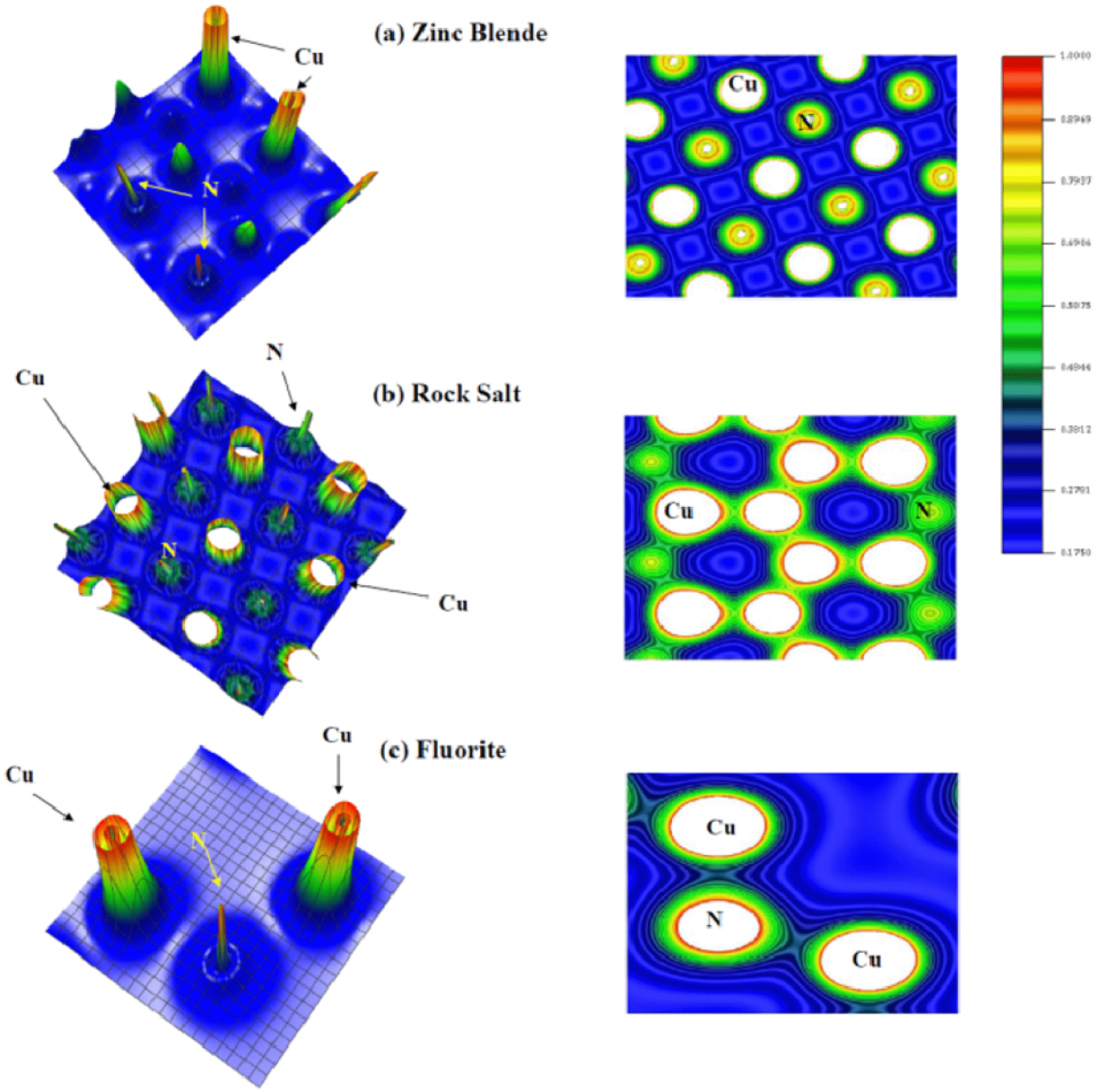

Figure 2.3: 2D and 3D-ELF for copper nitrides (a) ZB, (b) RS and (c) C1 phases.

2.7. Temperature effect

In order to investigate the thermodynamic properties, we studied thermal effects within the quasi-harmonic Debye model at high temperatures and pressures as implemented in the GIBBS program **[Blanco-04]**. We obtained $E - V$ data for the optimized CuN structures at $P = 0$ and $T = 0$, and then derived the macroscopic properties as functions of p and T from standard thermodynamic relations. Applying this model, we have successfully investigated the structural and thermodynamic properties of CuN in all the considered phases. The obtained pressure dependencies of the normalized volume are illustrated in Fig.2.4. To further investigate the thermal anisotropy of our systems, we calculate the linear thermal expansion parameters and in the inter-layer direction, by the following equation at zero pressure:

$$\alpha = \frac{\frac{\Delta l}{\Delta T}}{l_0} = \frac{1}{l_0}\frac{\partial l}{\partial T}\Big] p \qquad (2.14)$$

Where l represents the lattice parameter (a for our cubic structure). At room temperature, we obtain 1.90×10^{-5} K^{-1}, 1.81×10^{-5} K^{-1} and $1{:}70\times10^{-5}$ K^{-1} for ZB, RS and Fluorite phases respectively.

The obtained heat capacities, C_v, at P = 0 are plotted in Fig.2.5 showing that, when T> 500 K, C_v depends on both temperature and pressure. This is due to the anharmonic approximations of the Debye model used in our calculation. However, at higher temperature, the anharmonic effect on C_v is suppressed, and C_v is very close to the Dulong-Petit limit which is followed by all solids at high temperature. In the same Fig.2.5, we present at P = 0 the temperature dependencies of thermal expansion α. The thermal coefficient α also increases with T^3 at lower temperatures and gradually approaches to a linear increase at higher temperatures, and that the propensity to increase becomes moderate **[Goumri-Said-08]**. Moreover, the variation of thermal expansion coefficient with temperature is similar to that of Cv . Our results show that both of C_v and α are sensitive to the structure type of these copper nitrides.

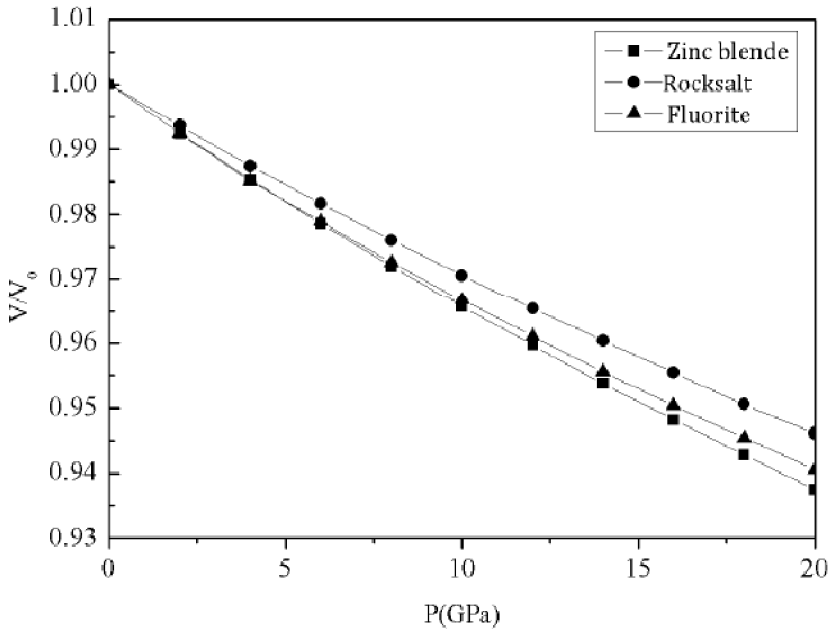

Figure2.4: Normalized volume of the copper nitrides as function of pressure.

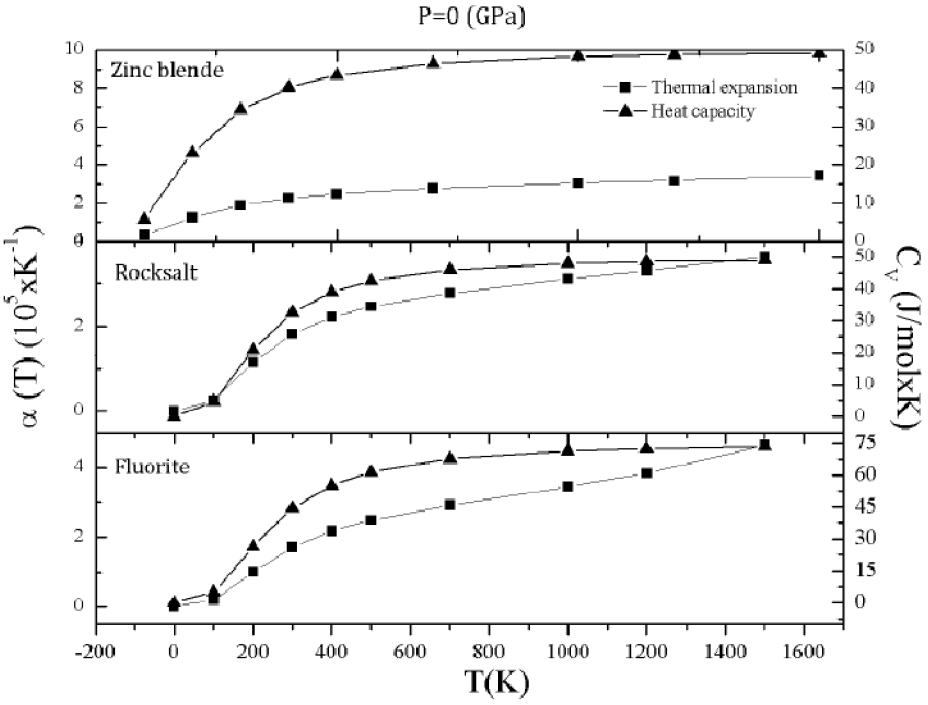

Figure2.5: Coefficient of linear thermal expansion (α) and the heat capacity (*Cv)*as a function of temperature for the considered phases

Summary

In summary, we have carried out ab *initio* calculations of structural, elastic, electronic, bonding, and thermal properties for different cubic phases for the copper nitrides. There is a concurrence between ionic and covalent character in the phases considered. The bond population calculation confirms that zincblende is the most covalent of these phases. Bonding nature was analyzed using the electronic localized function. Our results provide a basis for closer investigation of new copper nitride properties. We used the quasi-harmonic Debye model to study the effect of temperature on the variation of linear thermal expansion parameters and the specific heat. We are not aware of any experimental data or theoretical calculations on the copper nitrides, so we consider these results as a prediction study for these compounds.

References:

[Anderson-63] O.L. Anderson, J. Phys. Chem. Solids 24, 909 (1963)

[Blanco-04] M.A. Blanco, E. Francisco, V. Luana, Comput. Phys. Commun. 158, 57 (2004)

[Born-82] M. Born, K. Hang, Dynamical Theory and Experiments I (Springer Verlag Publishers, Berlin, 1982)

[Burnus-05] T. Burnus, M.A.L. Marques, E.K.U. Gross, Phys. Rev. A 71, 10501 (2005)

[de Paiva-07] R. de Paiva, R.A. Nogueira, J.L.A. Alves, Phys. Rev. B 75, 085105 (2007)

[Fedorov-68] F.I. Fedorov, *Theory of Elastic Waves in Crystals* (Plenum, New York, 1968)

[Goumri-Said-08] S. Goumri-Said, M.B. Kanoun, Comp. Mater. Sci. 43, 243250 (2008).

[Gregoryanz-04] E. Gregoryanz et al., Nat. Mater. 3, 294 (2004)

[Grossman-99] J.C. Grossman, A. Mizel, M. Cote, M.L. Cohen, S.G. Louie, Phys. Rev. B 60, 6343 (1999)

[Hill,-52] R. Hill, Proc. Phys. Soc. (London) A 65, 349 (1952)

[Ibrahim988] A.M. Ibrahim, Nucl. Instrum.Meth. B 34, 135 (1988)

[Jhi-99] S. -H. Jhi, J. Ihm, S.G. Louie, M.L. Cohen, Nature 399,132 (1999)

[Jin-05] Jin-Cheng Zheng, Phys. Rev. B 72, 052105 (2005)

[Kanoun-05] M.B. Kanoun, S. Goumri-Said, Phys. Rev. B 72, 113103 (2005)

[Kanoun-07] M.B. Kanoun, S. Goumri-Said, M. Jaouen, Phys. Rev. B 76, 134109 (2007)

[Kanoun-07]M.B.Kanoun, S. Goumri-Said, Phys. Lett.A 362, 73 (2007)

[Karki-97] B.B. Karki et al., Am. Mineral. 82, 51 (1997)

[Krishnamurthy-04] S. Krishnamurthy et al., Phys. Rev. B 70, 045414 (2004)

[Kroll-03] P. Kroll, Phys. Rev. Lett. 90, 125501 (2003)

[Ledbetter-83] M.H. Ledbetter, *Materials at Low Temperatures* (American Society for Metals, OH, 1983)

[Mattesini-03] M. Mattesini, R. Ahuja, B. Johansson, Phys. Rev. B 68, 184108 (2003)

[McMillan-03] P.F. McMillan, Nat. Mater. 1, 19 (2003)

[Milman-00] V. Milman et al., Int. J. Quantum Chem. 77, 895 (2000)

[Monkhorst-76] H.J. Monkhorst, J.D. Pack, Phys. Rev. B 13, 5188 (1976)

[Moreno-04] M.G. Moreno-Armenta, A. Martinez-Ruiz, N. Takeuchi, Solid State Sci. 6, 9 (2004)

[Moreno-07] M.G. Moreno-Armenta, W. Lopez Perez, N. Takeuchi, Solid State Sci. 9, 166 (2007)

[Nye-85] J.F. Nye, *Physical Properties of Crystals: Their Representation by Tensors and Matrices* (Oxford University Press, Oxford, 1985)

[Patil-06] S.K.R. Patil, S.V. Khare, B.R. Tuttle, J.K. Bording, S. Kodambaka, Phys. Rev. B 73, 104118 (2006)

[Perdew-96] J.P. Perdew, K. Burke, M. Ernzerhof, Phys. Rev. Lett. 77, 3865 (1996)

[Pierson-96] H. Pierson, Handbook of Refractory Carbides and Nitrides: Properties, Characteristics and Applications (Noyes, Westwood, NJ, 1996)

[Reuss-29] A. Reuss, Z. Angew. Math. Mech. 9, 49 (1929)

[Sahu-05] B.R. Sahu, L. Kleiman, Phys. Rev. B 71, 041101(R) (2005)

[Schreiber-73] E. Schreiber, O.L. Anderson, N. Soga, Elastic Constants and their Measurements (McGraw-Hill, New York, 1973)

[Segall-02] M.D. Segall et al., J. Phys.-Condens. Mat. 14, 2717 (2002) MATERIALS STUDIO, Version 4.2.1, AccelrysInc.(2002).

[Sigalas-92] M. Sigalas, D.A. Papaconstantopoulos, N.C. Bacalis, Phys. Rev. B 45, 5777 (1992)

[Silvi-94] B. Silvi, A. Savin, Nature 371, 683 (1994)

[Tvergaard-88] V. Tvergaard, J.W. Hutchinson, J. Am. Ceram. Soc. 71, 157 (1988)

[Vanderbilt-90] D. Vanderbilt, Phys. Rev. B 41, 7892 (1990)

[Voigt-28] W. Voigt, Lehrbuch der Kristallphysik (Teubner, Leipzig, 1928)

[Wu-05]Z. Wu, X-J. Chen, V.V. Struzhkin, R.E. Cohen, Phys. Rev. B 71, 214103 (2005)

[Young-06] A.F. Young et al., Phys. Rev. B 73, 153102 (2006)

[Yu-05] R. Yu, X.F. Zhang, Appl. Phys. Lett. 86, 121913 (2005)

[Yu-06] R. Yu, Q. Zhan, X.F. Zhang, Appl. Phys. Lett. 88, 051913 (2006)

[Zhan-03] Q. Zhan et al., Mater. Lett. 57, 3904 (2003)

[Zhang-09]. X. Zhang, G. Trimarchi, A. Zunger, Phys. Rev. B 79, 092102 (2009)

Chapter Three

Rare Earth Dioxides

Abstract

This chapter deals with properties and structure of rare earth dioxides. The goal of this chapter is to provide an overview of the properties that can be obtained in these systems, and to serve as a basis for more application driven research. Furthermore we try to understand the properties of these compounds from a physical and structural point of view, we clarify that the GGA implementation and the inclusion of the Hubbard U parameter and the spin-orbit coupling lead us to describe correctly the relativistic effect on 4f electrons.

"The rare earths perplex us in our researches, baffle us in our speculations, and haunt us in our very dreams. They stretch like an unknown sea before us, mocking, mystifying and murmuring strange revelations and possibilities"
Sir William Crookes, 1902

3.1. Introduction

The exploit of lanthanide elements in modern technology has increased dramatically over the past years, a continuous increase of the research effort on rare earths containing materials has occurred, and particularly on their oxides. Indeed, a number of functional materials based on rare earth oxides have been developed in various fields. Up to 1990, many review articles describing rare earth oxides have been reported and several intensive articles dealing with the physical properties have been published. It is presently acknowledged that the rare earth may find very relevant applications as catalysts **[Shafer-72, Trovarelli-02],** optical materials **[Gschneidner-81, Choppin-89, Bergmann-74],** or ionic conductors **[Guinier-64, Boulesteix-82].** Some of these applications have reached the technological maturity, large scale industrial consumption of the rare earth oxides being associated with them **[Bergmann-74],** Such is the case of the three-way catalysts **[Eyring-90, Eyring-98, Hyde-65, Zhang-96],** or the lighting applications of lanthanoid-containing photo-luminescent materials **[Gschneidner-81, Bergmann-74].**

3.1.1. Current interest in rare earth dioxides

From our personal items such as a portable compact disc player to a super computer or a huge atom-smashing accelerator, there are many rare earth materials having crucial roles in such systems. An automobile is a heap of rare earth materials. This is because rare earth ions exhibit some unique properties. Usefulness of rare earth materials for permanent magnets and luminescent materials for television and lighting systems goes without saying. Most of rare earth materials have been produced from rare earth oxides. Rare earth oxides are of importance for glass industry, not only glass components but also surface polishing **[Gschneidner-81].** As deduced from a recent review work, a great deal of data on the structural, physical and chemical properties of the binary rare earth oxides are presently available. This wealth of information has substantially modified our view about them, formerly, considered as a rather exotic group of oxides, with mainly academic interest.

In basic studies on markers for brain tumor and digestibility estimation, the rare earth oxides have an affinity for plant cell walls, and have been used in their soluble form to label indigestible plant fiber, in order to study digestion in ruminants

[Marabelli-87]. Samarium, scandium, ytterbium and europium oxides have already been successfully used as inert markers to measure apparent utilization of nutrients in humans **[Hutcheson-79].**Lanthanides are now incorporated into many technological devices, including superconductors, samarium-cobalt and neodymium-iron-boron high-flux rare-earth magnets, magnesium alloys, electronic polishers, refining catalysts and hybrid car components (primarily batteries and magnets)**[Haxel-06].** Most lanthanides are widely used in lasers, and as (co-)dopants in doped-fiber optical amplifiers (e.g. Er-doped fiber amplifiers (EDFAs) which are used as repeaters in the terrestrial and submarine fiber-optic transmission links that carry internet traffic). These elements deflect ultraviolet and infrared radiation and are commonly used in the production of sunglass lenses. Other applications are summarized in the following table 3.1 **[Helen-01].**

3.1.2. Classification

There is some confusion over the definition of the term rare earth (RE) element. Strictly speaking the term refers to the lanthanide series, that is those elements that have a partly-filled 4*f* orbital (series comprises the elements with atomic number increasing from 58 (cerium)(Ce) to 71 (lutetium)(Lu)). Usually lanthanum (La) is also included in the lanthanide series. All lanthanide elements form trivalent cations, Ln^{3+}, whose chemistry is largely determined by the ionic radius, which decreases steadily from lanthanum to lutetium.

From the chemical point of view, the Lanthanoid elements are characterized by a regular variation of their *4f* electron configuration throughout the series, Table 3.1. Inherent to this peculiar electron configuration, the lanthanoid elements show a number of atomic properties that are considered to determine the chemical and structural properties of their compounds, and, particularly, those of their oxides.

Despite their name, rare earth elements (with the exception of the radioactive promethium) are relatively plentiful in the Earth's crust, with cerium being the 25th most abundant element at 68 parts per million (similar to copper), even the least abundant lanthanoid elements, Tb, Tm, and Lu, are more abundant than Ag **[Kilbourn-93]**. However, because of their geochemical properties rare earth elements are typically dispersed and not often found in concentrated and economically exploitable forms known as rare earth minerals. It was the very scarcity of these minerals (previously

called "earths") that led to the term "rare earth". The first such mineral discovered was gadolinite, a compound of cerium, yttrium, iron, silicon and other elements.

The electronic structure of the lanthanide elements, with minor exceptions is [Xe]$6s^2 4f^n$. In their compounds, the 6s electrons are lost and the ions have the configuration [Xe]$4f^m$. The chemistry of the lanthanides differs from main group elements and transition metals because of the inner nature of the *4f* orbitals. Also, the differences of electron configuration between the lanthanoid elements are associated to 4*f* electrons relatively well screened from the chemical surroundings by the outer ($5s^2p^6$) shell. This implies weak crystal fields splitting effects **[Antic-02],** and a relatively small covalent contribution to the bonding. Accordingly, the ionic model plays an important role in determining their chemistry. Also related to these chemical characteristics, the lanthanoid compounds exhibit a rich variety of structures, often reflected in the occurrence of polymorphism phenomena.

As *f-f* transitions are forbidden, once an electron has been excited, decay to the ground state will be slow. This makes them suitable for use in lasers as it makes the population inversion easy to achieve. The Nd:YAG laser is one that is widely used. Lanthanide ions are also fluorescent as a result of the forbidden nature of *f-f* transitions. Europium-doped yttrium vanadate was the first red phosphor to enable the development of color television screens **[Eyring-90]**

Table3.1: Some relevant properties of the lanthanides elements their atomic number and symbol, and their main usages [**Kilbourn-93**].

Z	Symbol	Name	Electron Conf.	Selected Usages
57	La	Lanthanum	$5d^16s^2$	High refractive index glass, flint, hydrogen storage, battery-electrodes, camera lenses, fluid catalytic cracking catalyst for oil refineries
58	Ce	Cerium	$4f^15d^16s^2$	Chemical oxidizing agent, polishing powder, yellow colors in glass and ceramics, catalyst for self-cleaning ovens, fluid catalytic cracking catalyst for oil refineries
59	Pr	Praseodymium	$4f^36s^2$	Rare-earth magnets, lasers, core material for carbon arc lighting, colourant in glasses and enamels, additive in Didymium glass used in welding goggles, ferrocerium firesteel (flint) products.
60	Nd	Neodymium	$4f^46s^2$	Rare-earth magnets, lasers, violet colors in glass and ceramics, ceramic capacitors
61	Pm	Promethium	$4f^56s^2$	Nuclear batteries
62	Sm	Samarium	$4f^66s^2$	Rare-earth magnets, lasers, neutron capture, masers
63	Eu	Europium	$4f^76s^2$	Red and blue phosphors, lasers, mercury-vapor lamps, NMR relaxation agent
64	Gd	Gadolinium	$4f^75d^16s^2$	Rare-earth magnets, high refractive index glass or garnets, lasers, x-ray tubes, computer memories, neutron capture, MRI contrast agent, NMR relaxation agent
65	Tb	Terbium	$4f^96s^2$	Green phosphors, lasers, fluorescent lamps
66	Dy	Dysprosium	$4f^{10}6s^2$	Rare-earth magnets, lasers
67	Ho	Holmium	$4f^{11}6s^2$	Lasers
68	Er	Erbium	$4f^{12}6s^2$	Lasers, vanadium steel
69	Tm	Thulium	$4f^{13}6s^2$	Portable X-ray machines
70	Yb	Ytterbium	$4f^{14}6s^2$	Infrared lasers, chemical reducing agent
71	Lu	Lutetium	$4f^{14}5d^16s$	PET Scan detectors, high refractive index glass

3.1.3. Overview of experimental and theoretical works

On account of this obvious importance, several studies have already been conducted especially for CeO_2 and little for PrO_2. On the experimental side, the electronic states were experimentally determined on the basis of spectroscopic measurements **[Marabelli-87, Fujimori-83, Karnatak-87, Ogasawara-91]** and the Brillouin zone

center (BZC) phonon frequencies have been measured by several methods **[Spanier-01,Wang-01].** The variety of experimental results reported on the bulk modulus of CeO_2 **[Duclos-88, Gerward-93, Nakajima-94, Gerward-05]** and PrO_2 **[Gerward-05].** The high-pressure α-PbCl2-type phase of the CeO_2 has also been investigated and the transition pressures have been reported as 31 GPa.

On the theoretical side, a small number of calculations have been published for PrO_2 **[Dabrowski-01, Mehrotra-07, Divi-04, Divi-05, Novk-07]** in contrast to the number of studies related to CeO_2. Particularly, elastic stiffness, electronic structure and dielectric functions for all rare earth dioxides have not been considered yet with an accurate approximation as well as spin-orbit coupling and strong correlation effects. As for CeO_2, numerous calculations are available and are carried out by several methods such as periodic Hartree-Fock **[Gennard-99],** self-interaction-corrected local spin-density approximation **[Gerward-05, Petit-07],** local-density approximation (LDA), and generalized gradient approximation (GGA) within density functional theory (DFT) **[Mehrotra-07, Skorodumova-01, Koelling-83, Fabris-05, Loschen-07, Jiang-05, Yang-04, Silva-07]**. The debate on the methods to investigate systems with localized (strongly correlated) *f* electrons still continues in the literature. Many researchers believe that conventional DFT techniques based on LDA or GGA could be unable to cope with these systems. This belief is supported by the current and recent papers on CeO_2 and Ce_2O_3 **[Skorodumova-01, Skorodumova-04].** The LDA+U and GGA+U methods **[Anisimov-91, Anisimov-97]** are applied in the study of CeO_2 **[Shi-10, Gurel-06, Nolan-05, Andersson-07]** and PrO_2 **[Tran-08]** where Hartree-Fock type interactions are parameterized with Coulomb U and exchange J terms.

3.1.4. About fluorite structure

Fluorite structure (CaF_2) has the basic crystal structure knows as fluorite, which is shown in Figure 3.1. It is one of the most common crystalline solid types found in nature. This structure type is the aristotype for all the intermediate rare earth oxides. The fluorite structure is filled with a host structure; the anions form a simple cubic lattice where the cations occupied the half of the cubic sites. It is also possible to reverse the roles of cations and anions and considered cations as a face-centred cubic (fcc) arrangement with the anions occupying all tetrahedral sites. These two views are equivalent; the fluorite structure can be equated with two subnet works: cations form a

subnet fcc and anions form a cubic primitive subnet. In the fluorite structure, the coordination number of cations and the anions is 8 and 4 respectively. This corresponds to fcc structure in which the cations are positioned at (0, 0, 0) and the anions are located at (1/4, 1/4, 1/4) and (3/4, 3/4, 3/4), there are 4 CaF_2 in unit cell in the group Fm3m.

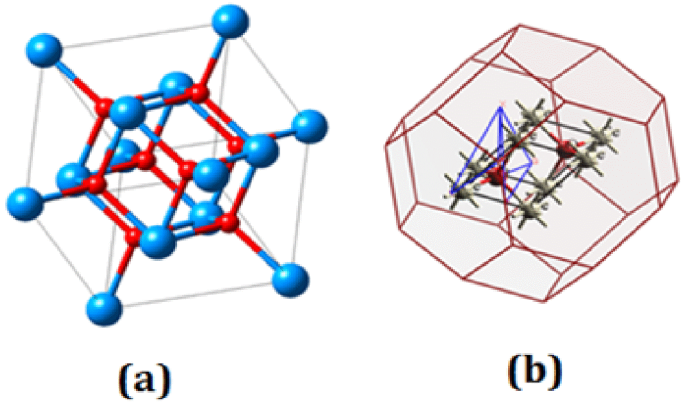

Figure3.1: (a) Crystal structure and (b) Brillouin Zone for the primitive cell of REO_2Blue atoms are RE and red atoms are Oxygen.

3.2. Computational details

Our calculations were carried out using the full-potential (linearized) augmented plane waves plus local orbitals (FP-(L)APW+lo) method **[Blaha-01]** based on the density functional theory. The electronic exchange and correlation functions have been treated by utilizing both LDA and Wu-Cohen scheme **[Wu-06]** form of GGA together with their on-site Coulomb interaction added versions, The muffin-tin radii (R_{MT}) are considered to be equal to 2.22 and 1.9 a.u. (bohr units) for Ce and O atoms, respectively. The self-consistent procedure has been carried out with the energy cutoff constant $R_{MT} \times K_{max} = 9$ and the Brillouin zone integrations were performed with the special k-points method over 12×12×12 Monkhorst-Pack mesh **[Monkhorst-76].** To improve the description of rare earth (RE) *4f* electrons we used the GGA+U (U is the Hubbard term) which corresponds to the GGA+U method described in Refs. **[Anisimov-93]** and **[Liechtenstein-95]** with the GGA correlation potential instead of LDA. In the GGA+U-like methods, an orbitally dependent potential is introduced for the chosen set of electron states, which in our case is 4*f* states of RE. This additional potential has an

atomic Hartree-Fock form but with screened Coulomb and exchange interaction parameters. The choice of U is, however, not unambiguous and it is not trivial to determine its value a priori, though there are attempts to extract it from standard first-principles calculations **[Cococcioni-05].** In order to determine the $U_{\text{eff}} = U - J$ (setting $J = 0$), available experimental data such as lattice constant, bulk modulus, and band gap have been compared with the calculated values. Hence, U_{eff} is treated as an empirical fitting parameter. Moreover, the spin-orbit coupling was included in all calculations. The convergence of the self-consistent field calculations is attained with a total energy convergence tolerance of 0.1 mRy. Moreover, the spin orbit coupling (SOC) was also included in the calculations based on the second variational approach **[Blaha-01]**.

3.3. Effect of strong correlation on Ceria

3.3.1. Fundamental properties

The cerium as all rare-earth elements differs from main group elements because of the presence of the 4*f* orbitals, which are more localized and induce then a direct weak coupling between themselves and ions. On the other hand, *4f* RE elements can have larger magnetic moments than the 3d elements, and, unlike the d states, *f* electrons can couple strongly with the host s electrons, leading to the possibility of electron-mediated ferromagnetism in these materials. It can therefore be anticipated that for a RE, LDA is unable to describe correctly the interaction between these localized and strongly correlated 4*f* electrons and the itinerant 3*d* states of the host material. This could be overcome by treating the 4*f* states as core states. An efficient and popular way to improve on the LDA failure without resorting to fully atomic 4*f* behavior is to use the LDA+U method. In LDA+U, the correlation absent in LDA is reintroduced by an onsite Coulomb repulsion parameter *U* (called also Hubbard parameter), to which an *a priori* value has to be assigned. The Hubbard approach has been used in some recent works with considerable success. It's expressed in terms of two parameters. These are the Hubbard parameter U, which reflects the strength of the on-site Coulomb interaction, and the parameter J, which adjusts the strength of the exchange interaction. In the somewhat simplified, these two parameters are combined into a single parameter $U_{eff}=U–J$.

The crystal structure of CeO_2 is equivalent with that of fluorite structure Fm3m (see Fig. 3.1). Firstly, to determine the U_{eff} parameter for this rare earth oxide lattice parameter, the bulk modulus, and band gap (E_{gap} = O 2*p* - Ce 4*f* and E_{gap} = O 2*p* - Ce 5*d*) values are calculated by LDA+*U* and GGA+*U*, then these results are compared with the experimental data as shown in Fig.3.2. Equilibrium lattice parameter, bulk modulus, and its pressure derivative for CeO_2 are gathered in Table3.2, in comparison with experimental **[Gerward-93, Nakajima-94, Gerward-05, Villars-91]** and theoretical values **[Skorodumova-01, Fabris-05, Silva-07, Gurel-06, Shi-10,Sevik-09].** The equilibrium lattice constant (a) and the bulk modulus (B) were estimated by fitting the Murnaghan-Birch equation of states **[Murnaghan-44, Birch-78]** to the resulting energy-volume data. This equation is expressed as

$$E(V) = E_0 + \frac{9V_0B_0}{16}\left\{\left[\left(\frac{V_0}{V}\right)^{\frac{2}{3}} - 1\right]^3 B'_0 + \left[\left(\frac{V_0}{V}\right)^{\frac{2}{3}} - 1\right]^2 \left[6 - 4\left(\frac{V_0}{V}\right)^{\frac{2}{3}}\right]\right\} \qquad (3.1)$$

Where E_0 and V_0 are the energy and volume at equilibrium B and B' are the bulk modulus and it's the pressure derivative

The lattice parameter is underestimated by 0.62 % at the purely LDA level (U_{eff}=0eV) compared to experiment. Thus, introducing U_{eff}> 0 show that lattice parameter is always larger than experimental value but increases as function of U_{eff} for GGA+U (see Fig.3. 2a). In the case of LDA+U, the lattice parameter is smaller than experimental data but also increases of U_{eff}. In the case of GGA+*U*, the calculation at U_{eff} = 0 eV gives that a is overestimated by 0.13 % compared to the experimental data and for a U_{eff} value between 4 and 5 eV the lattice parameter matches the experimental value. As indicated in Fig.3.2b, the bulk modulus value is also steadily increasing with increasing U_{eff} but this observable is even less affected by the latter parameter. However, our calculated a and B values calculated by the GGA+*U* approach with U_{eff} values 5 eV compare well with the experimental data. In addition to consistent reproduction of a and B with the chosen values of U_{eff} for CeO_2 compound, the calculated values for band gaps are reasonably good, given the well-known fact that DFT underestimate band gaps of insulators (see Fig.3.2c). Furthermore, our systematic study of these three parameters shows that the GGA+*U* (with Wu and Cohen scheme) approach works better than LDA+*U* and also PBE+U (Perdew-Burke-Ernzerhof formalism).

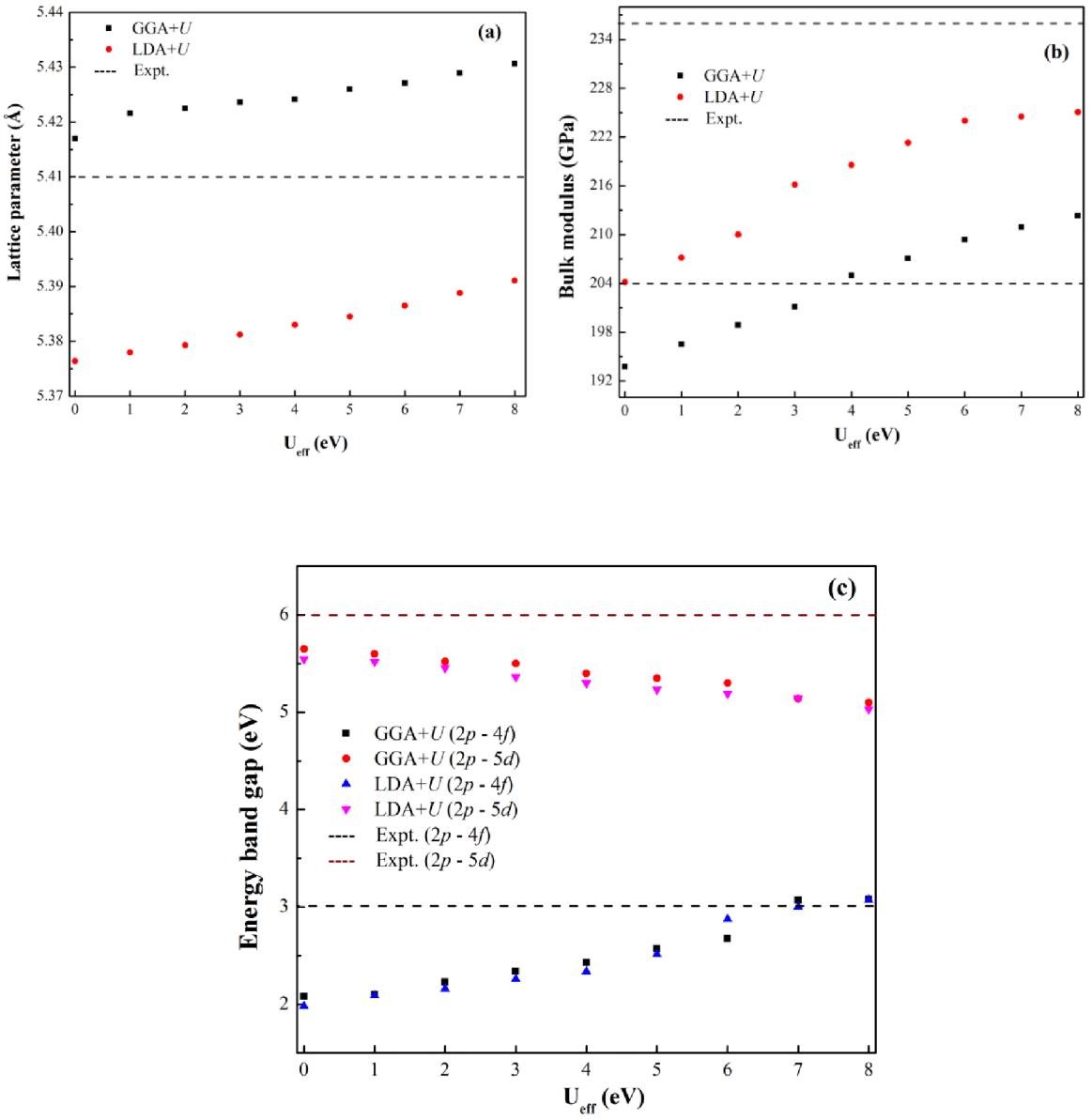

Figure 3.2: (a) Lattice constant, (b) bulk modulus and (c) band gap as a function of the Hubbard U_{eff}

Table3.2: Equilibrium lattice parameter (a), bulk modulus (B), and its pressure derivative (B') of CeO_2 compared to other theoretical and experimental data. (a is in Å, B in GPa, and B' dimensionless).

	a	B	B'	
FP-(L)APW+lo GGA (U = 0)	5.417	193.74	4.60	Our work
FP-(L)APW+lo GGA+U, 5 eV	5.426	207.08	4.81	Our work
FP-(L)APW+lo LDA (U = 0)	5.376	204.15	4.25	Our work
FP-(L)APW+lo LDA+U, 5 eV	5.384	221.3	4.5	Our work
Experiment	5.410	204 - 236		[a,b,c,d]

[a,b,c,d]reference**[Gerward-93, Nakajima-94, Gerward-05,Villard-91]**

3.3.2 Electronic structure of Ceria

In order to show the effect of strong correlation in electronic structure, we have calculated the total and partial density of states (DOS) curves at the predicted equilibrium lattice constants for CeO_2, which are displayed in Figure3.3 within the framework of GGA approach with and without U_{eff}, where the vertical line is the Fermi level (E_F).A common trend can be proposed from total DOS graphs that the influence of U_{eff} on the electronic structure is basically restricted to the unoccupied f state and this does not drastically change the electronic distribution especially occupied states. Another consequence of higher values of U_{eff} is a slightly reduced width value of the Ce 4f peak and increases the intensity of this peak, which reflects stronger localization.

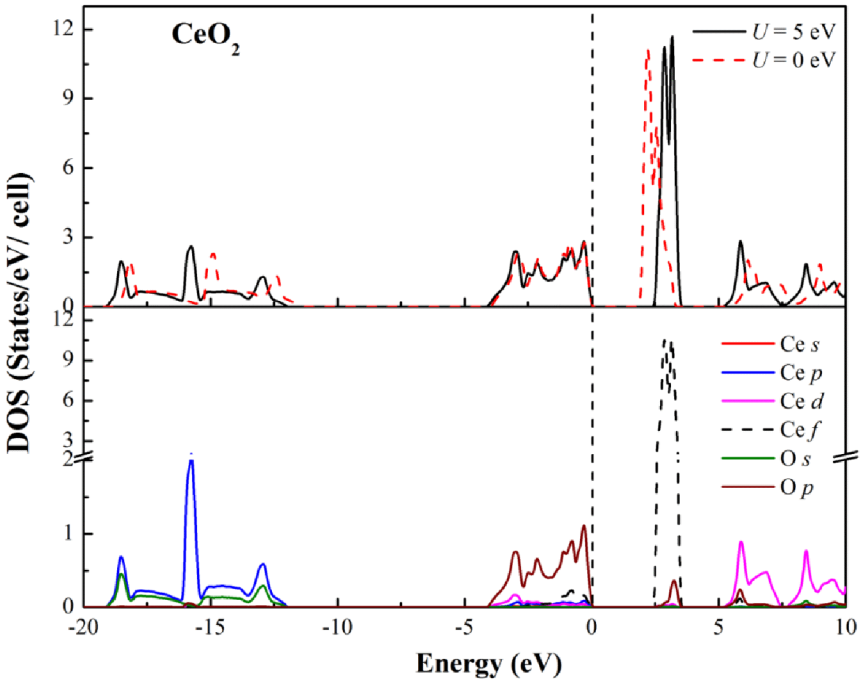

Figure3. 3: Total and partial density of states at GGA+*U* (with *U* = 0 and 5 eV) for CeO_2. Since the spin-up and spin-down channels are identical, only the spin-up channel is shown. The vertical solid line denotes the Fermi level.

3.4. Physical properties of rare earth dioxides

3.4. 1. Equilibrium lattice properties

As first step, the ground-state structures of dioxides REO_2 for the rare earths, RE= La, Ce, Pr, Nd, PM, Sm, Eu, Gd, Tb, Dy, Ho, Er, Tm, Yb, and Lu, were obtained by performing DFT/GGA (add U) calculations with spin-polarization effects. The equilibrium lattice constants (*a*), bulk modulus (B) and its pressure derivative (B') for dioxides REO_2 are listed in Table 3.4, in comparison with experimental data **[Duclos-88, Gerward-93, Nakajima-94, Gerward-05, Villars-91]** and recent theoretical calculations **[Mehrotra-07, Skorodumova-01, Fabris-05, Loschen-07, Jiang-05, Yang-04, Silva-07, Shi-10,Gurel-06 , Sevik-09]** for comparison. The calculated *a* and *B* values have been obtained from the corresponding energy minimization at constant volumes and by fitting to a third-order Birch-Murnaghan equation of state **[Murnaghan-44, Birch-78]** to find the optimized parameters.

As a general remark, the deviations for lattice constants are estimated to be about 0.07 - 0.7 % for CeO_2, PrO_2 and TbO_2 compared to available experimental data. The trends of the calculated lattice parameter of dioxides REO_2 may be discussed as displayed in Figure 3.4. As can be seen, the increase of valence electrons of RE elements when moving rightwards along the periodic table results in a decrease of the lattice parameter except for GdO_2. We have also noticed that the LaO_2 and GdO_2 have larger lattice constant values than the other dioxides REO_2.

However, our theoretical approach seems to considerably underestimate the bulk modulus, the calculated values being 207.08GPa and 189.38 GPa for CeO_2 and PrO_2, respectively, which are 6 - 19 % and 3% lower than the experimental data **[Duclos-88, Gerward-93, Nakajima-94, Gerward-05, Villars-91]**. It is observed that the experimental values for the bulk modulus of CeO_2 are confined to a 15 % range 204 to 236 GPa, whereas there is large scatter of the calculated values. Therefore, it is worth noticing that all GGA calculations tend to underestimate the bulk modulus. Unfortunately, there are no experiential data for other rare earth dioxides. Moreover, it is clear that the predicted bulk modulus value for CeO_2 is larger than the REO_2 compounds.

Table3.3: Lattice parameter *a* (Å), bulk modulus *B* (GPa), its pressure derivative *B'*, of REO_2 compared to other theoretical and experimental data.

		a	*B*	*B'*
LaO_2	This work	5.706	127.72	4.36
CeO_2	This work	5.426	207.08	4.81
	Experiment[a,b,c]	5.410	204-236	
	SIC-LSD[b]	5.384	176.9	
	FP-LMTO [d]	5.48	187.7	
	PW-PP[f]	5.48	178.0	
	PAW GGA+U [g]	5.48	187.0	
	PAW GGA+U[h]	5.38	202.4	
	PAW GGA[i]	5.45	194	
	PAW PBE0 [j]	5.39		
	PAW PBE[j]	5.47	172	
	L/APW+LO PBE[j]	5.47	170	
	PAW LDA+U[k]	5.40	217	
	HGH PP[l]	5.40	211.11	4.417
	PAW LDA+U[m]	5.366	210.1	4.4
PrO_2	This work	5.380	189.38	4.01
	Experiment[b,c]	5.394	187	
	SIC-LSD[d]	5.364	176.8	
	TB-LMTO[n]	5.392	378	
NdO_2	This work	5.358	184.80	4.97
PmO_2	This work	5.344	169.10	4.05
SmO_2	This work	5.345	156.53	5.96
EuO_2	This work	5.386	145.57	4.32
GdO_2	This work	5.434	144.64	4.18
TbO_2	This work	5.272	192.03	4.76
	Experiment[c]	5.222		
DyO_2	This work	5.241	181.36	4.62
HoO_2	This work	5.248	188.05	5.81
ErO_2	This work	5.242	177.18	4.46
TmO_2	This work	5.237	168.80	4.90
YbO_2	This work	5.240	173.37	4.60
LuO_2	This work	5.220	166.40	4.48

[a] reference **[Duclos-88]**,[b] reference**[Gerward-05]**,[c] reference **[Villars-91]**

[b] reference**[Gerward-05]**(SIC, self-interaction corrected; LSD, local spin density approximation)

[d] reference [**Skorodumova-01**] (FP LMTO, full potential linear muffin tin orbital)

[f] reference **[Fabris-05]**(PW PP, plane-wave pseudopotential method)

[g]reference**[Loschen-07]**(PAW, projector-augmented wave method
[h]reference**[]iang-05]**(PAW, projector-augmented wave method)
[i] reference**[Yang-04]**(PAW, projector-augmented wave method)
[j]reference **[Silva-07**](PAW, projector-augmented wave method)
[k]reference **[Shi-10] (**PAW, projector-augmented wave method)
[l]reference**[Gurel-06**] (HGH, Hartwigsen-Goedecker-Hutter PP)
[m]reference **[Sevik-09]**(PAW, projector-augmented wave method)
[n]reference **[Mehrotra-07]**(TB LMTO, Tight binding linear muffin tin orbital)

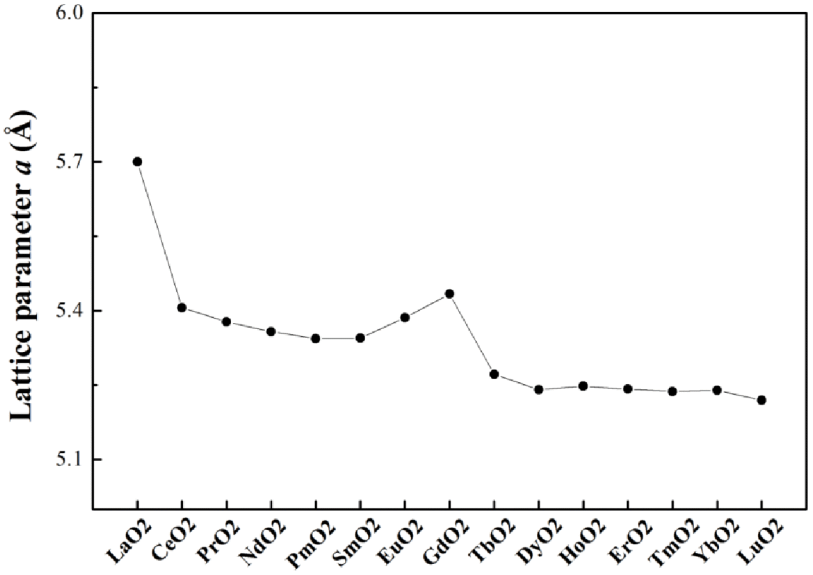

Figure 3.4: Calculated lattice parameter as function of rare earth dioxides compounds.

3.4. 2. Magnetic stability

The origin of the magnetism lies in the orbital and spin motions of electrons and how the electrons interact with each other**.** These are quantum mechanical phenomenon due to the relative orientation of the spins of two electrons. In some solids the magnetic moments on different atoms are ordered and can form a ferromagnetic or an antiferromagnetic. In the ferromagnetic phase, the magnetic moment on each atom is aligned in the same direction as shown in figure 3.5. Ferromagnetic materials exhibit parallel alignment of moments resulting in large net magnetization even in the absence of a magnetic field.

Many crystals have magnetic ions that are ordered in arrangements other than ferromagnetic. In antiferromagnetic (AFM) ordering, the moments pointing in one direction are balanced by others pointing in the opposite direction, with the result that

the substance has no net magnetization. The exchange interaction between ions in this case has the opposite sign and favors the alternate arrangements of spins. The sign of the exchange interaction between ions depends on the length of the covalent bond and the bonding angles; it may have either orientations.

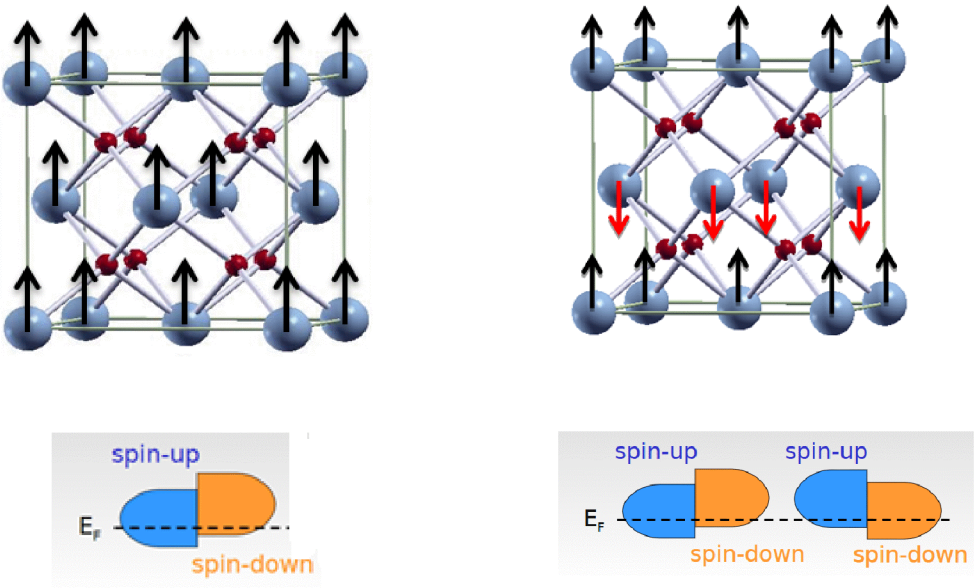

Figure3.5: Ferromagnetic and antiferromagnetic ordering

In order to compute the ground state magnetic phase between antiferromagnetic (AFM) and ferromagnetic (FM) phases, we calculated the total energy difference $\Delta E_{(AFM-FM)}$ between them. Results are summarized in Table 3.4 and displayed inFig.3.6.We must recall here that the FM phase is stabilized over the AFM phase when $\Delta E > 0$, whereas the AFM is stabilized over the FM phases when ($\Delta E < 0$). From the Table 3.4 and Fig. 3, we found that the ground state is the FM phase for LaO_2, PmO_2, SmO_2, EuO_2, TbO_2, TmO_2, and YbO_2.

So, for PrO_2, NdO_2, GdO_2, DyO_2, HoO_2 and HoO_2 compounds, the AFM phase is more stable but $\Delta E_{(AFM-FM)}$ are small. This result indicates that these systems are weakly anti-ferromagnets. Note that no theoretical calculations or experimental data exist for REO_2 as far as the stable magnetic phases are concerned.

Table 3.4: total energy difference ($E_{(AFM-FM)}$) between antiferromagnetic (AFM) and ferromagnetic (FM) phases of REO_2

	LaO_2	PrO_2	NdO_2	PmO_2	SmO_2	EuO_2	GdO_2	TbO_2	DyO_2	HoO_2	ErO_2	TmO_2	YbO_2
ΔE $_{(AFM-FM)}$	10.32	-0.56	-0.85	1.70	10.20	11.22	-5.42	37.41	-4.52	-9.77	-0.07	5.80	2.10

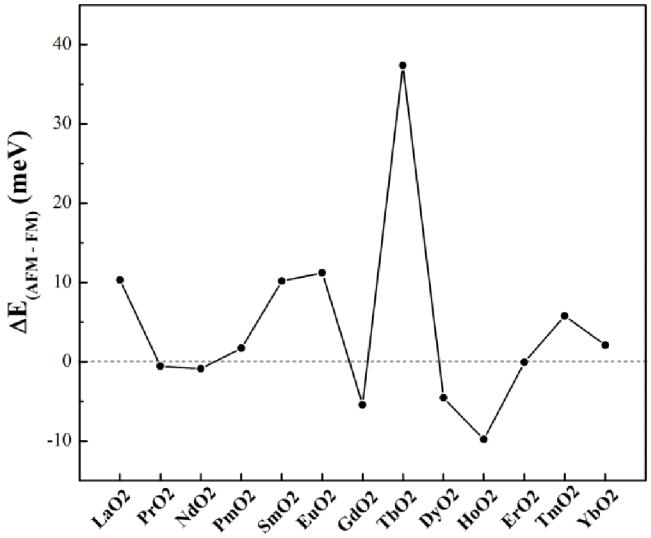

Figure 3.6: The total energy difference $\Delta E_{(AFM-FM)}$ as function of rare earth dioxides compounds

3.4. 3. Elastic stiffness and related polycrystalline properties

The elastic stiffness determines the response of the crystal to an externally applied strain (or stress) and provides information about the bonding characteristics, mechanical and structural stability. The elastic constants C_{ij} were calculated within the total-energy method, where the unit cell is subjected to a number of finite-size strains along several strain directions. Cubic lattices have three independent elastic constants **[Nye-85],** namely, C_{11}, C_{12}, and C_{44}, as show in following equation. The obtained elastic stiffness constants C_{ij} are gathered in Table 3.5. Furthermore, the mechanically stable phases or macroscopic stability is dependent on the positive definiteness of stiffness

matrix **[Fedorov-68].** For a stable cubic structure, the independent elastic constants should satisfy the well-known Born-Huang criterion **[Born-82],** given by:

$$\begin{matrix} C_{44} > 0 \\ C_{11} > |C_{12}| \\ C_{11} + 2C_{12} > 0 \end{matrix} \qquad (3.2)$$

One may see that the rare earth dioxides are mechanically stable because all elastic constants are positive and satisfy the Born mechanical stability restrictions. Considering the experimental data set due to Nakajima et al **[Nakajima-94],** the C_{11}, C_{12} and C_{44} for CeO_2 values are underestimated by 3%, 22 % and 5%, respectively, whereas the agreement is good for all elastic constants. Note also that our results are in close agreement with the available theoretical works **[Gurel-06, Sevik-06].**

In order to measure the stiffness of the solid, Voight-Reuss-Hill **[Hill-52, Reuss-29, Voigt-28]** estimates B_{VRH}, G, Y and υ of polycrystalline bulk modulus, shear modulus, Youngs modulus, and Poissons ratio computed from C_{ij} are presented in Table 3.5(following the procedure detailed in chapter 1). One can remark that the shear and Youngs modulus of the PrO_2 is higher than all REO_2 dioxides compounds. The larger shear modulus is mainly due to its larger C_{44}.

Table 3.5: Calculated elastic constants C_{ij}(GPa), Bulk moduli B_{VRH} (GPa), shear moduli G (GPa), Young's modulus Y (GPa), and Poisson's ratio ν for rare earth dioxides.

	C_{11}	C_{12}	C_{44}	B_{VRH}	G	Y	ν
LaO_2	149.3	124.22	204.0	132.58	78.06	195.76	0.254
CeO_2	390.86	128.5	57.0	215.95	80.14	213.96	0.334
	390[a]	130[a]	82[a]				
	386[b]	124[b]	73[b]				
	354.79[c]	139.27[c]	51.19[c]				
	403[d]	105[d]	60[d]				
PrO_2	344.33	126.5	181.1	199.11	147.68	355.23	0.202
NdO_2	241.04	116.5	131.35	158.01	97.34	242.28	0.244
PmO_2	217.18	128.01	98.33	157.73	71.58	186.54	0.303
SmO_2	270.91	123.26	105.72	172.47	91.55	233.36	0.274
EuO_2	159.36	132.18	326.61	141.24	116.69	274.48	0.176
GdO_2	235.7	68.4	100.62	177.37	85.01	219.9	0.293
TbO_2	300.2	108.63	130.0	184.94	119.33	294.63	0.234
DyO_2	200.0	166.05	209.0	191.16	125.38	308.66	0.230
HoO_2	291.21	138.37	142.66	189.32	111.05	278.66	0.254
ErO_2	322.3	125.6	147.5	186.31	94.44	242.38	0.283
TmO_2	200.3	123.15	93.0	148.87	65.34	171.0	0.309
YbO_2	253.53	152.7	143.61	186.31	94.44	242.38	0.283
LuO_2	314.48	128.92	59.02	190.77	70.8	189.01	0.334

[a] reference **[Sevik-06],** [b] reference**[Gurel-06],** [c] reference **[Shi-10],** [d] reference **[Nakajima-94]**experimental data

3.4. 4. Electronic properties

3.4.4.1. Density of states of nonmagnetic CeO_2 and LuO_2

The calculated total and partial density of states (DOS) curves at the predicted equilibrium lattice constants for rare earth dioxides $CeO_2$and $LaO_2$are shown in figure3.7

within the framework of GGA+U calculations, where the vertical line is the Fermi level E_F . In which concerns the electronic structure of CeO_2, the gap between the valence O (2*p*) and conduction Ce (5d) bands is 5.5 eV, however this calculated value is slightly smaller than the measured one (6 eV) **[Andersson-07]** and agrees with a previous theoretical study (5 - 5.5) eV**[Skorodumova-01, Loschen-07, Andersson-07].** Furthermore, the distance between the valence band and the Ce*4f* states is 2.66 eV, compared to 3 eV in experiments **[Andersson-07].** Then, the width of the O 2*p* is 4.38 eV, which agrees with experimental data and theoretical calculation. We notice an important feature in DOS that they are the O 2*p*–Ce*5d* band gap and the empty Ce*4f* states in the gap above the O *2p* band.

For LuO_2, the *4f* states are fully occupied around -5 eV and are located below the oxygen *p* states. Note that the O 2*p* states are partially occupied and are situated above the Fermi level.

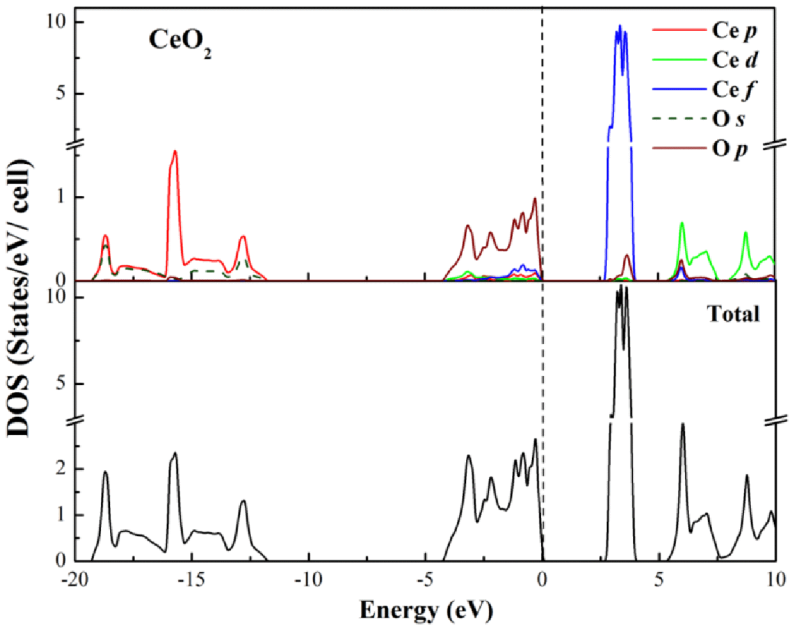

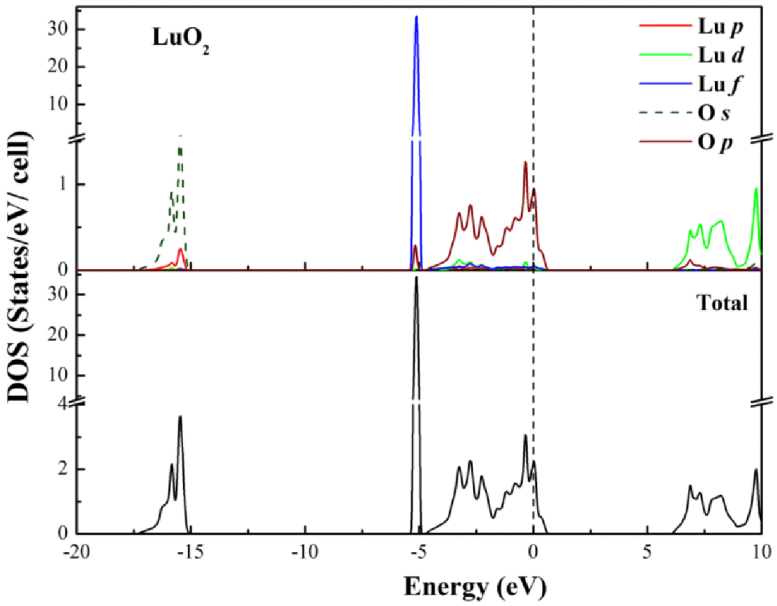

Figure 3.7: The total and partial density of states at GGA+U+SOC for CeO_2 and LuO_2. Since the spin-up and spin-down channels are identical, only the spin-up channel is shown. The vertical solid line denotes the Fermi level.

3.4.4.2. Density of states of REO_2 (RE= Pr, Nd, PM, Sm, Eu, Gd, Tb, Dy, Ho, Er, Tm, Yb, and Lu)

We have also displayed in figure 3.8 the total and partial DOS curves for rare earth dioxides REO_2 (RE= Pr, Nd, PM, Sm, Eu, Gd, Tb, Dy, Ho, Er, Tm, Yb, and Lu). The DOS of PrO_2 is plotted in Figure3.8. We can see that the highest occupied states Pr*4f* states for spin up are situated around -4 eV below the Fermi energy and concentrates them into a sharp peak. Note that the peak from the O 2*p* DOS at -4 eV comes from separate bands without 4*f* contributions and thus these *4f* states are localized and not hybridized with the O 2*p* states. A further indication of the Pr 4*f* - O 2p hybridization can be observed from some similarities in the positions of the peaks at -0.8 and -0.3 eV between the Pr 4*f* and O 2*p* curves. Note that the spin-up and spin-down Pr 4*f* DOSs above -3 eV, are very similar. Above the Fermi level we find the unoccupied *f* -levels. The fundamental band gap separates the valence band maximum and unoccupied Pr 4*f* is about 1.8 eV. Then, at about 5 eV above the Fermi energy, states predominantly of Pr 5*d* character begin to appear. Derived from experimental data, Van der Kolk and Dorenbos **[van-06]** proposed

a model to predict the insulating or metallic behavior and chemical stability of lanthanide materials. From their model, it was predicted that for PrO_2, the *4f* empty states are situated at about 2 eV above the top of the valence band, a feature which is quite well reproduced by our calculated DOS where we obtained a value of 1.8 eV. For TbO_2, we observe the dominance of Tb *4f* to majority spin in the valence band and of the minority spin in the forbidden band. Note that the spin up Tb *4f* are centered around -10 eV below Fermi level and for spin down bands, they are empty and situated between the valence band maximum and conduction band minimum with a more localized peak about 2 eV.

LaO_2 has its outer 6s electrons removed, but the *4f* shell is still empty. The DOS in GGA+U_d+U_f is also shown in Fig. 3.7. The effect of adding U_f is simply to push up the empty *4f* states in the conduction band minimum. They are centered at about 6 eV. Again, there is a small overlap between the La 5*d* conduction band and O 2*p* valence band.

In the case of NdO_2, the occupied majority spin *f* states are situated in top of valence band near the Fermi level (E_F). The density of states Figure 3.8at E_F is then dominated by *p-f* bands. In addition, the empty majority and minority spin bands occur in conduction band minimum. In PmO_2, the occupied *f* electrons occur in narrow energy range and the rest is located near the E_F. Note that the O *p*- Pm *f* bands dominated this last region. Thus, the empty majority spin bands situated above the E_F. We also observe that the empty minority spin bands occur in the forbidden band.

The DOS of SmO_2 is shown in Figure 3.8. The majority spin occupied *f* bands occur in three narrow energy ranges. Furthermore, the empty *f* bands of majority spin are about 3.5 eV above the E_F , while the empty minority spin *f* bands occur in conduction band minimum and in conduction band between about 6.5 and 8.5 eV and significantly hybridize with the rest of the conduction band.

As for SmO_2, the majority spin occupied *f* bands in EuO_2 occur in four narrow energy ranges and the empty *f* bands of majority spin are about 5 eV above the E_F. Then, the empty minority spins *f* bands situated in conduction band minimum and also in conduction band.

For GdO_2, we show in Figure 3.8that the majority spin *4f* states are fully occupied around -5 eV and are located below the oxygen *p* states. The minority spin *4f* states are fully unoccupied and are nearly 7.5 eV above the Fermi level.

Again, the DyO_2 and HoO_2 have the same behavior where the spin-majority occupied *4f* states occur in four narrow bands. The remaining occupied *f* electrons go in minority spin bands at about -1 and -4 eV. One may notice that the empty minority spin *f* bands located in conduction band minimum.

In ErO_2, the majority spin *f* states occur again in five narrow bands, while the minority spin bands are filled and occur almost evenly spread and alternating with the majority spin bands in energy. The empty minority spin bands occur in a narrow band about 4 eV above the Fermi level.

Like to ErO_2, the TmO_2 has the same behavior where the majority spin *f* bands which are completely filled, on the other hand, occur again in narrow energy ranges. The minority spin bands however show significant splitting while the empty minority spin bands occur in a two narrow band about 3 and 4 eV above the Fermi level. Finally, for YbO_2, it can be seen that the majority and minority spin occupied *4f* states are located between -2 and -7 eV while the empty minority spin bands occur in a narrow band about 4 eV.

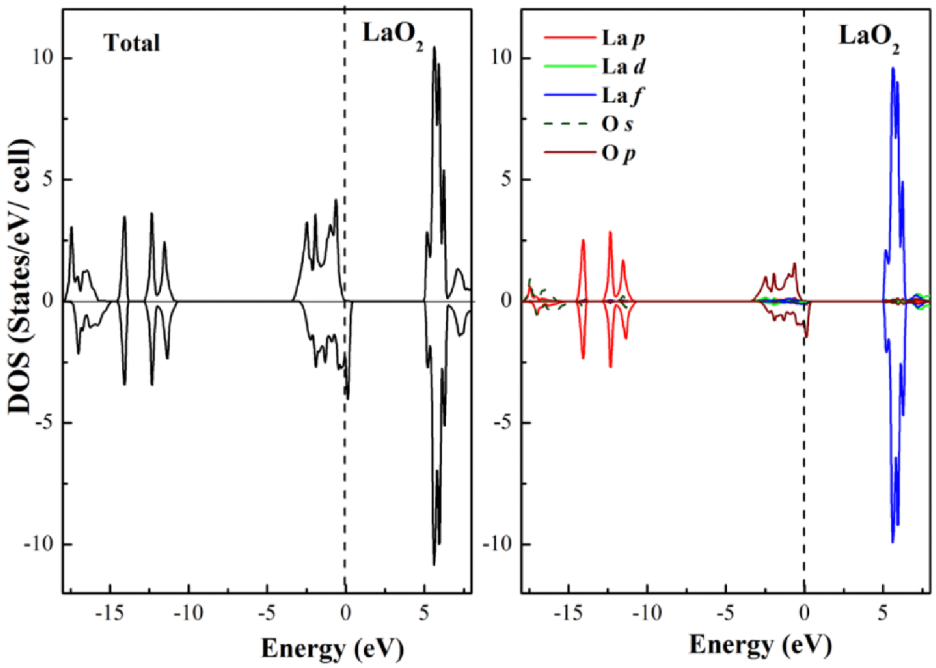

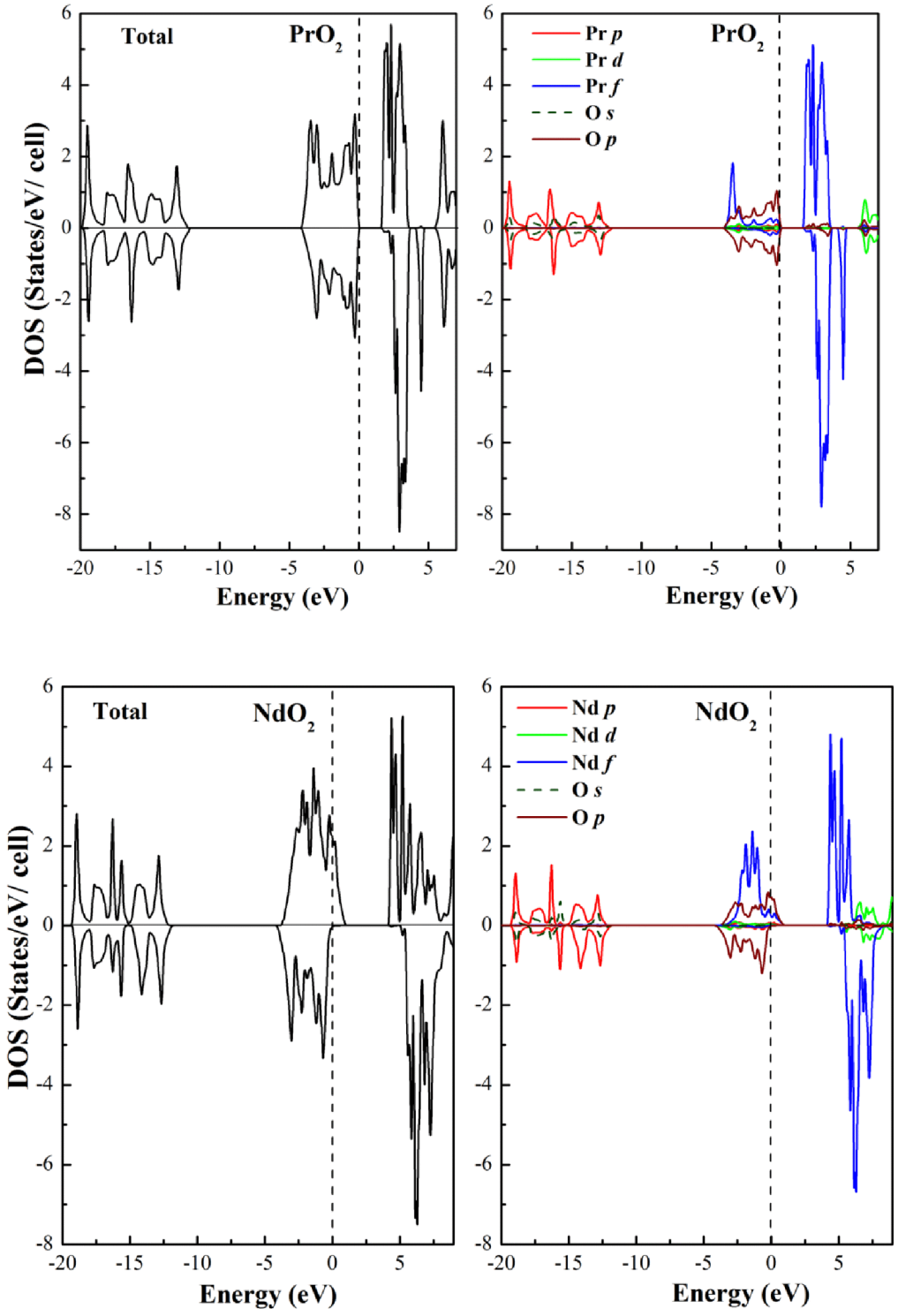

Figure 3.8(suite): Calculated total and partial density of states at GGA+U+SOC for REO_2 (RE=La, Pr, Nd, Pm, Sm, Gd, Tb, Dy, Ho, Er, Tm and Yb)) for majority (upper part) and minority (lower part) spin states.

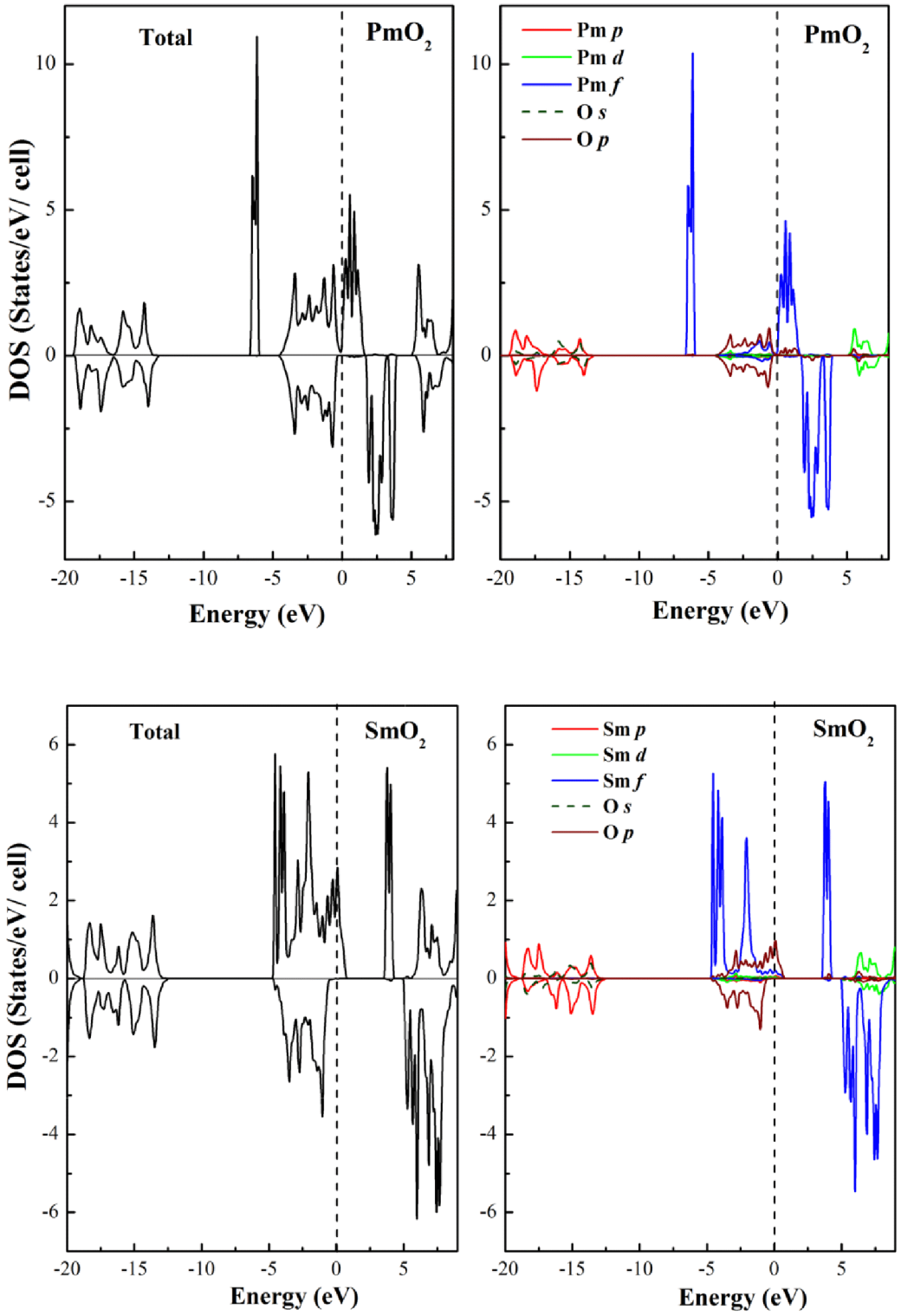

Figure 3.8(suite): Calculated total and partial density of states at GGA+U+SOC for REO_2 (RE=La, Pr, Nd, Pm, Sm, Gd, Tb, Dy, Ho, Er, Tm and Yb)) for majority (upper part) and minority (lower part) spin states.

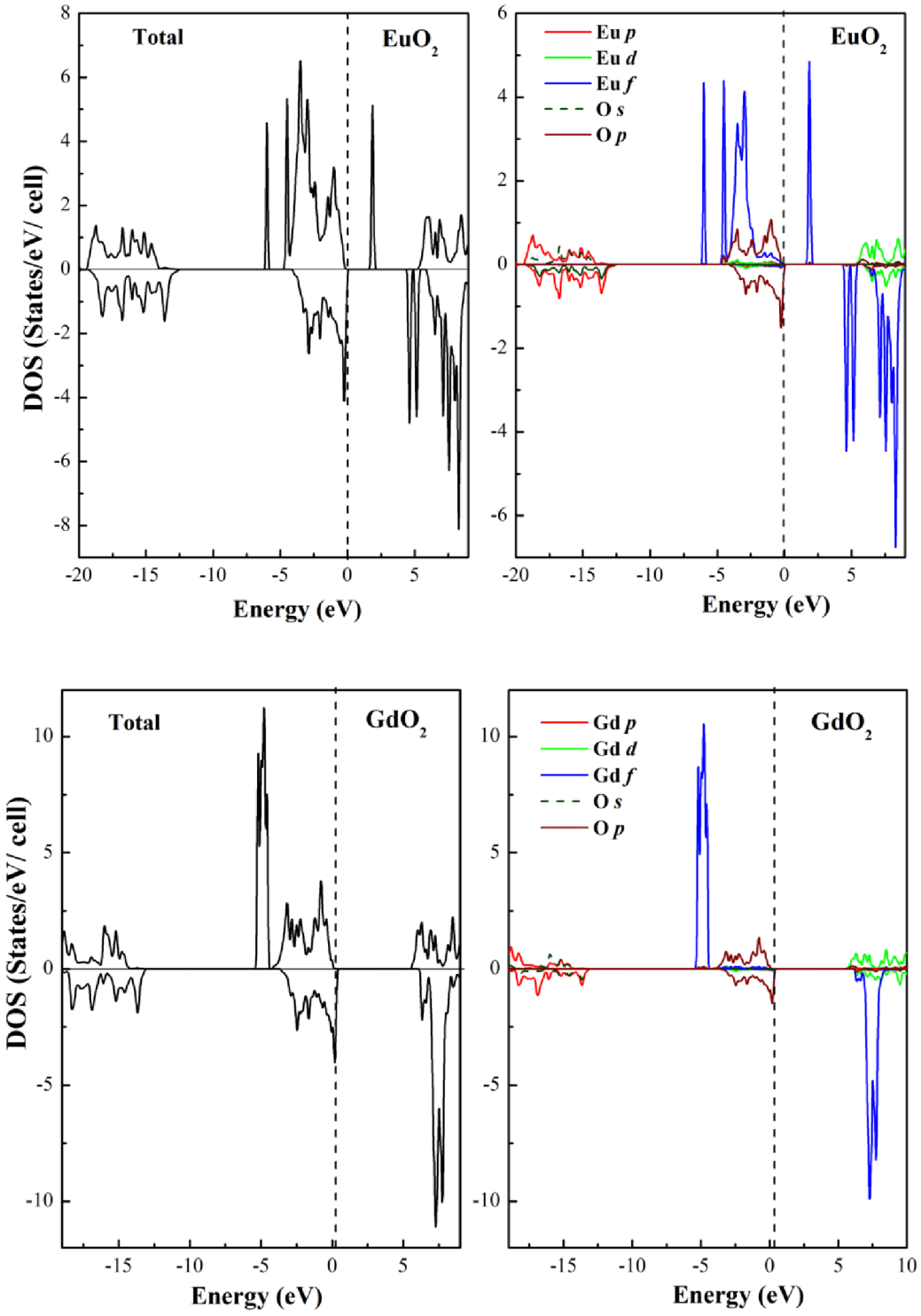

Figure 3.8(suite): Calculated total and partial density of states at GGA+U+SOC for REO_2 (RE=La, Pr, Nd, Pm, Sm, Gd, Tb, Dy, Ho, Er,Tm and Yb)) for majority (upper part) and minority (lower part) spin states.

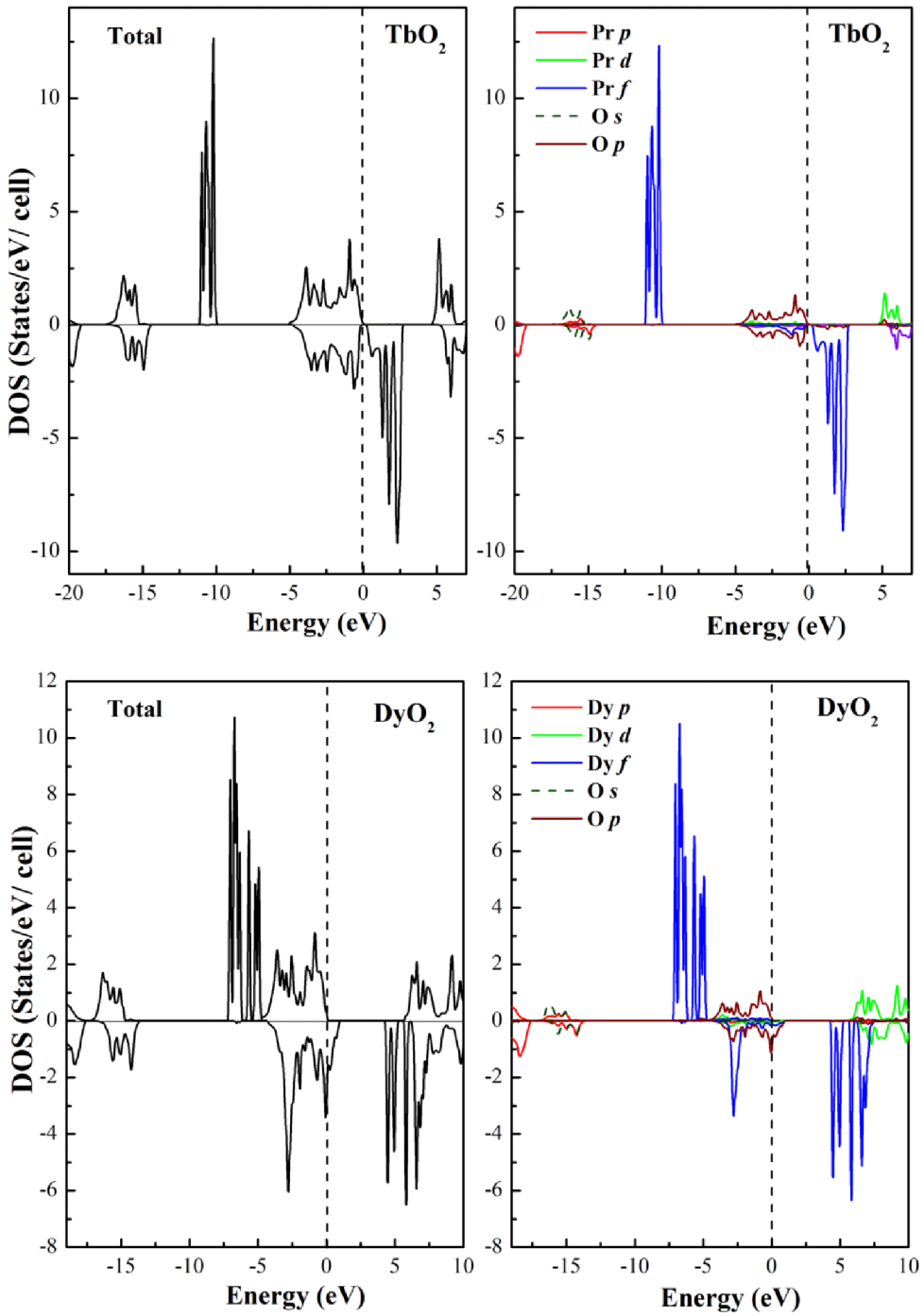

Figure 3.8(suite): Calculated total and partial density of states at GGA+U+SOC for REO_2 (RE=La, Pr, Nd, Pm, Sm, Gd, Tb, Dy, Ho, Er, Tm and Yb)) for majority (upper part) and minority (lower part) spin states.

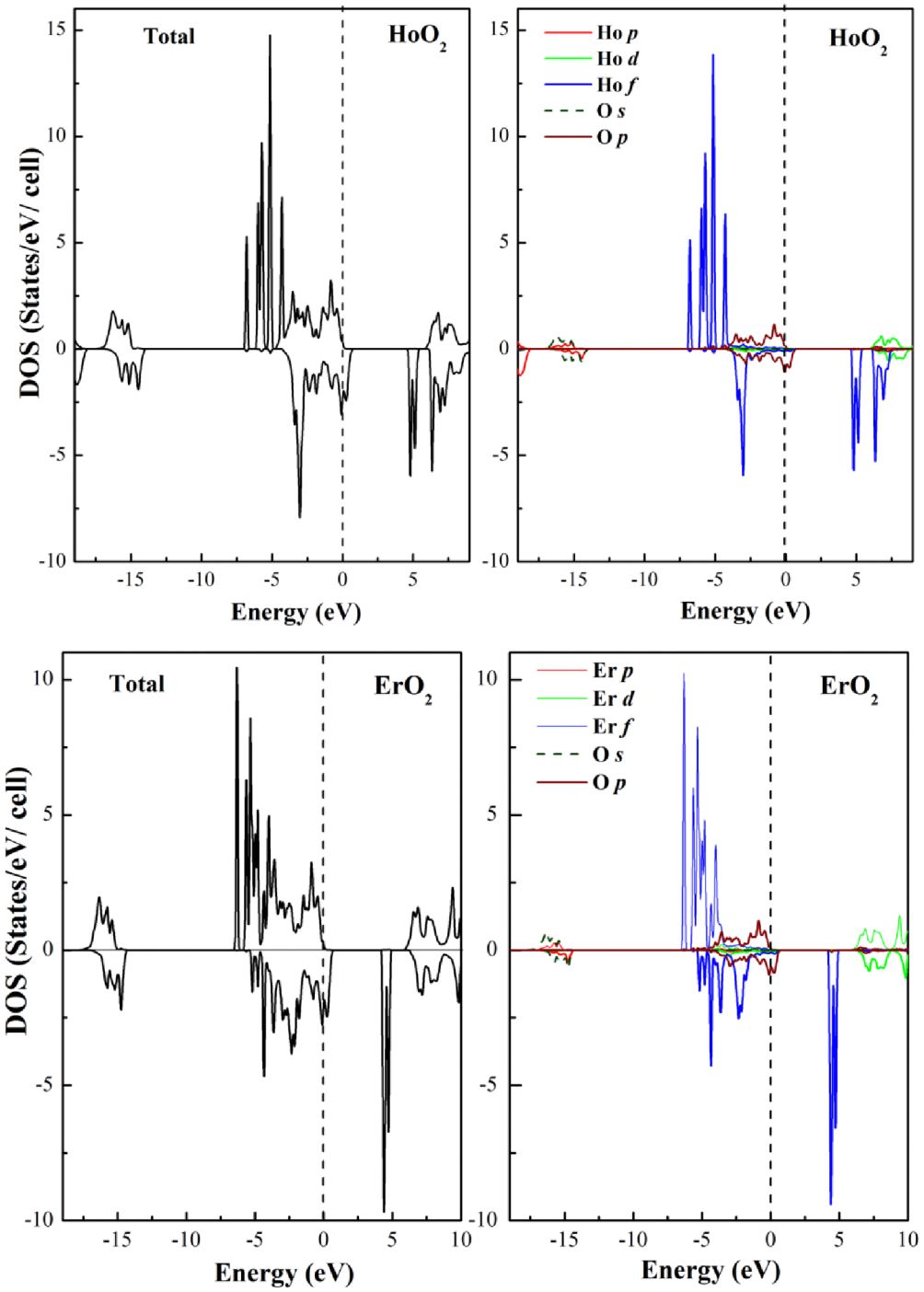

Figure 3.8(suite): Calculated total and partial density of states at GGA+U+SOC for REO_2 (RE=La, Pr, Nd, Pm, Sm, Gd, Tb, Dy, Ho, Er, Tm and Yb)) for majority (upper part) and minority (lower part) spin states.

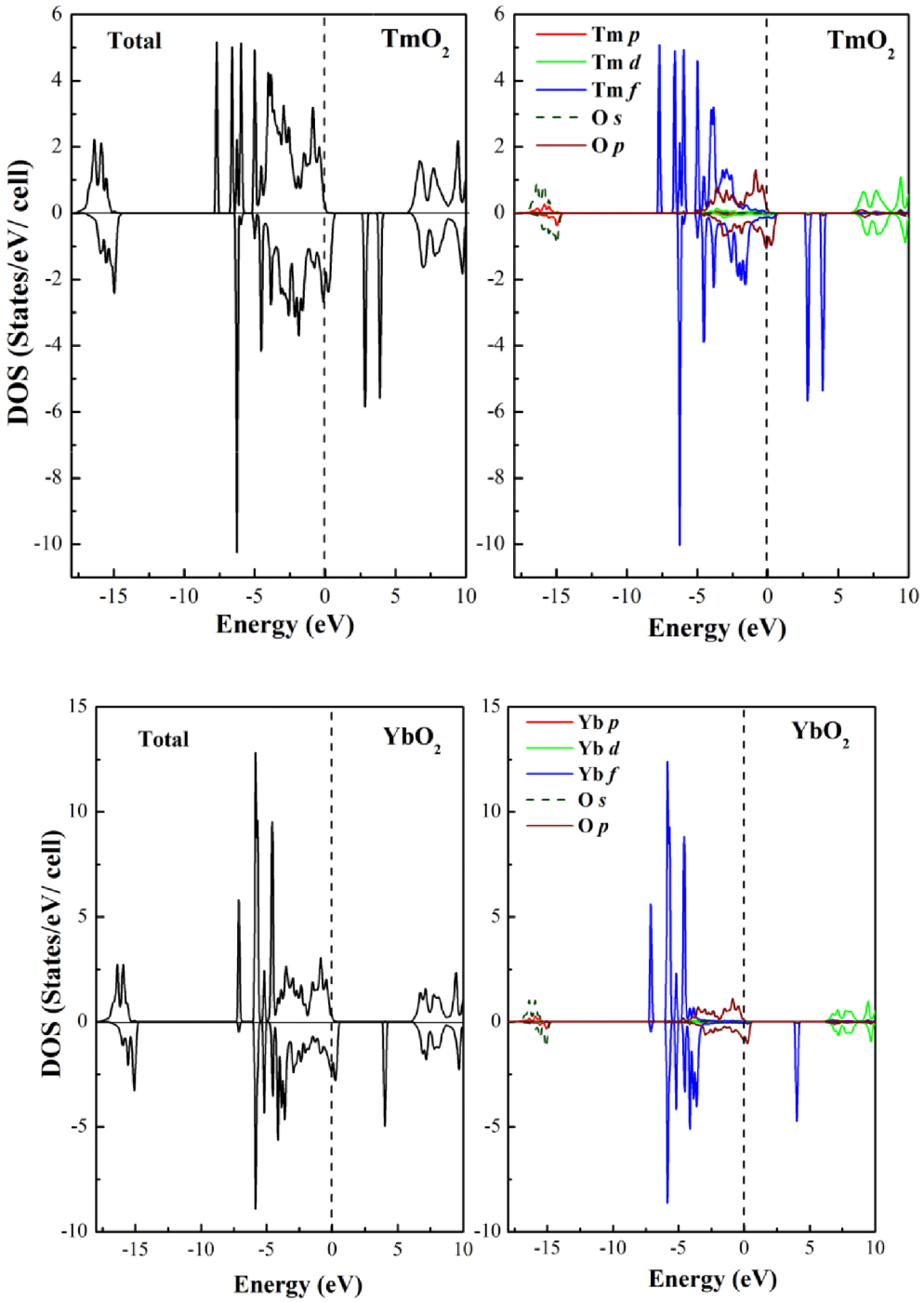

Figure 3.8(suite): Calculated total and partial density of states at GGA+U+SOC for REO_2 (RE=La, Pr, Nd, Pm, Sm, Gd, Tb, Dy, Ho, Er, Tm and Yb)) for majority (upper part) and minority (lower part) spin states.

3.4.5. Magnetic properties

We present the total and local magnetic moment by one cell for REO_2 compounds in Table 3.6. The total moment comes principally from the rare earth elements. A relative amount of the moment is found in the interstitial region about 0.001 - 0.08μB, while oxygen has a small induced moment about 0.1 - 0.5μ_B for all rare earth dioxides except for PrO_2, NdO_2, PmO_2, and SmO_2 where it shows weak antiparallel spin moment close to -0.1 and -0.47μ_B. It is important to notice that gadolinium has a strong value of magnetic moment compared to other compounds. Moreover, one can clearly observe from Figure 3.9 that the curve trend adopts triangular-like form where the total moment increases with the filling of the *f* states of the rare earth element until Gd about 7.999μ_B and after it decreases.

Table 3.6: Total and local magnetic moments (in$\mu_B/cell$) for rare earth dioxides

	M^{tot}	m^{RE}	m^{O}	$m^{interstitial}$
LaO_2	1.0	0.018	0.490	0.001
CeO_2	0.0	0.0	0.0	0.0
PrO_2	0.999	1.147	-0.101	0.056
NdO_2	2.112	2.834	-0.390	0.058
PmO_2	2.955	3.221	-0.142	0.017
SmO_2	3.996	4.875	-0.474	0.071
EuO_2	6.960	5.960	0.464	0.066
GdO_2	7.999	6.964	0.478	0.078
TbO_2	7.016	6.645	0.157	0.056
DyO_2	5.998	5.259	0.348	0.043
HoO_2	5.000	4.108	0.428	0.033
ErO_2	3.936	3.266	0.291	0.088
TmO_2	2.993	1.959	0.506	0.020
YbO_2	1.916	0.928	0.483	0.020
LuO_2	0.0	0.0	0.0	0.0

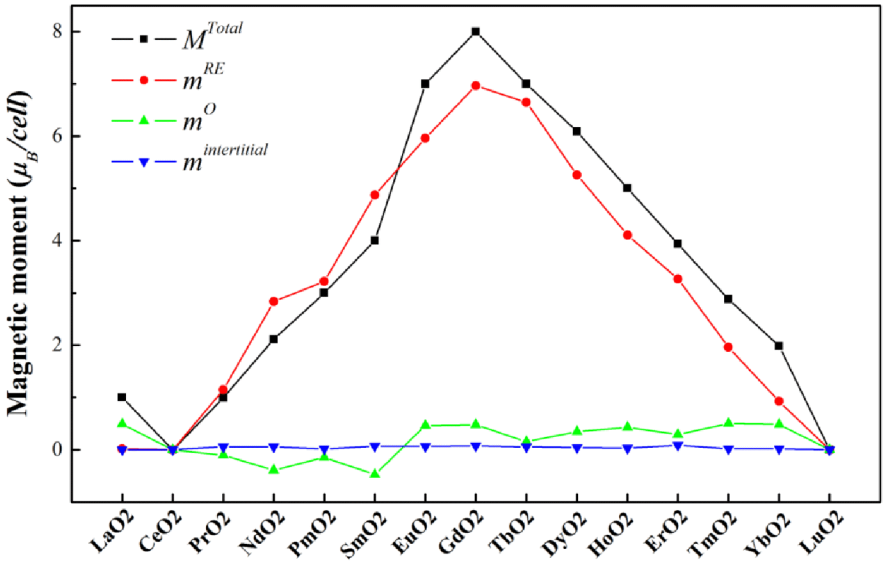

Figure 3.9: Total and local magnetic moments versus of REO_2 (RE = La, Pr, Nd, Pm, Sm, Gd, Tb, Dy, Ho, Er,Tm and Yb) .

3.4. 6. Charge density contours

To gain a more detailed insight into the bonding characters of nonmagnetic rare earth compounds, we calculate the charge density distribution. The charge density contours for a cut in the (110) plane of CeO_2 compound are displayed in Figure 3.10. It clearly seen that cerium oxide is characterized by a nearly spherical charge-density distribution around the Ce and O atoms and a low charge density in the interstitial region. It can be also seen that the ionic bonding is the determinant of the chemical bonding in CeO_2, even though the covalency is strong in the sense of orbital participation in forming the valence state. According to our density of states analysis and results of population analysis obtained by Nakamatsu and *al* **[Nakamatsu-95],** it can be to attribute to CeO_2 a covalent character due to the strong hybridization between O 2*p* and Ce*4f* and 5d states and ionic character to O p and Ce 5*s* and 5*p* states. Moreover, the components of Ce*5s, 5p* make a repulsive interaction with O *2p* because of overlap of the essentially filled states. Concerning the bonding in CeO_2, this repulsion cancels the covalent bonding between Ce 4*f*, 5*d* and O 2*p*.We have also sketched in Fig.3.10, the charge density distributions in (110) plane of LuO_2. Note that the completely filled *4f* case occurs in LuO_2. It can be seen that there is an increase of the electron charge

density around the O atoms and a decrease in the interstitial region between Lu atoms. Furthermore, these charges rearrangements reflect the electronegative nature of O atoms. It revealed an ionic contribution to the bonding that adds to a clear metallic character. Therefore, our results demonstrate that the bonds of LuO_2 are an unusual mixture of metallic and ionic bonding.

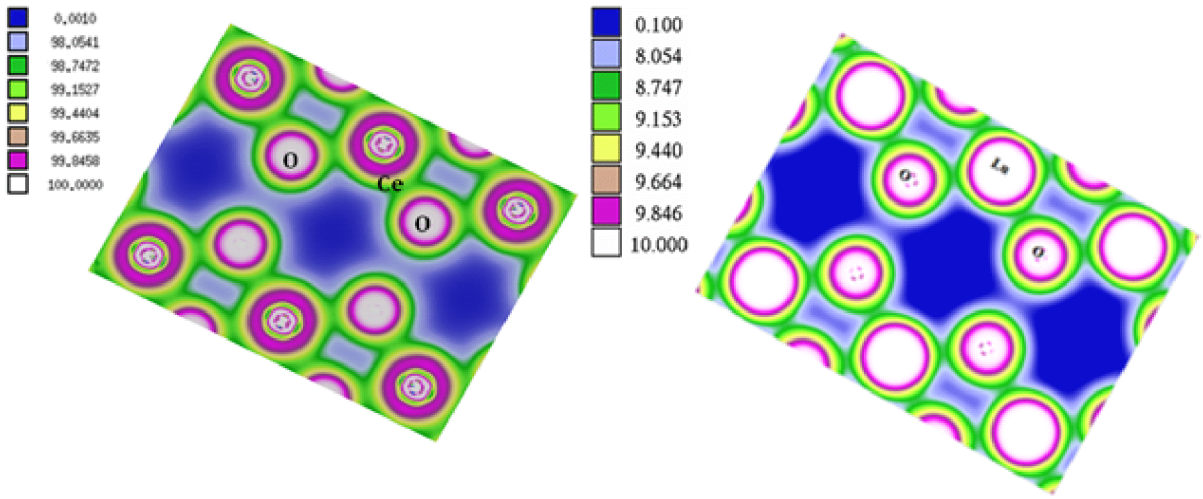

Figure 3.10: Charge density distributions in (110) plane of CeO_2 and LuO_2.

3.4. 7. Spin density contours

To complete the magnetic structure description, we display in Fig. 3.11, the spin densities map of the magnetic systems. One may observe that it is an increase in the polarization of Oxygen atoms. Moreover, interactions appeared between heavy rare earth atoms show a pronounced effect on the spin densities maps. The electron density symmetry around second rare earth atom is also influenced appreciably by cation-anion interactions and the oxides magnetic properties also reflect this complexity. This result agree well with a former calculations performed on the sesquioxides that suggested including the possibility of subshell contributions and effective electron numbers are derived for all the ions including rare earths whose polarizabilities are experimentally published **[Grimes-98].**

It is interesting to see that from one compound to another, the spin density distribution changes in size and shape. The spin density distribution around the oxygen has a circular appearance but slightly modified due to the polarization induced by the

presence of RE atom. Besides this polarization varies from one system to another, the value of the density around O atoms is estimated at 5, 1, 0.43, 0.3421, 0.285, 0.285, 0.6, and 0.11 for SmO_2, EuO_2 PmO_2, NdO_2, PrO_2, GdO_2, HoO_2 and ErO_2 systems, respectively. For the remaining systems, it tends to be negative. On the other hand, the shape of the spin densities distribution around the RE atom is far from circular. This distribution depends on the filling of orbitals, mainly the *f* one. We are able to conclude that the hybridization between different orbitals affects the spin density contours **[Grimes-98, Kanoun-09].**

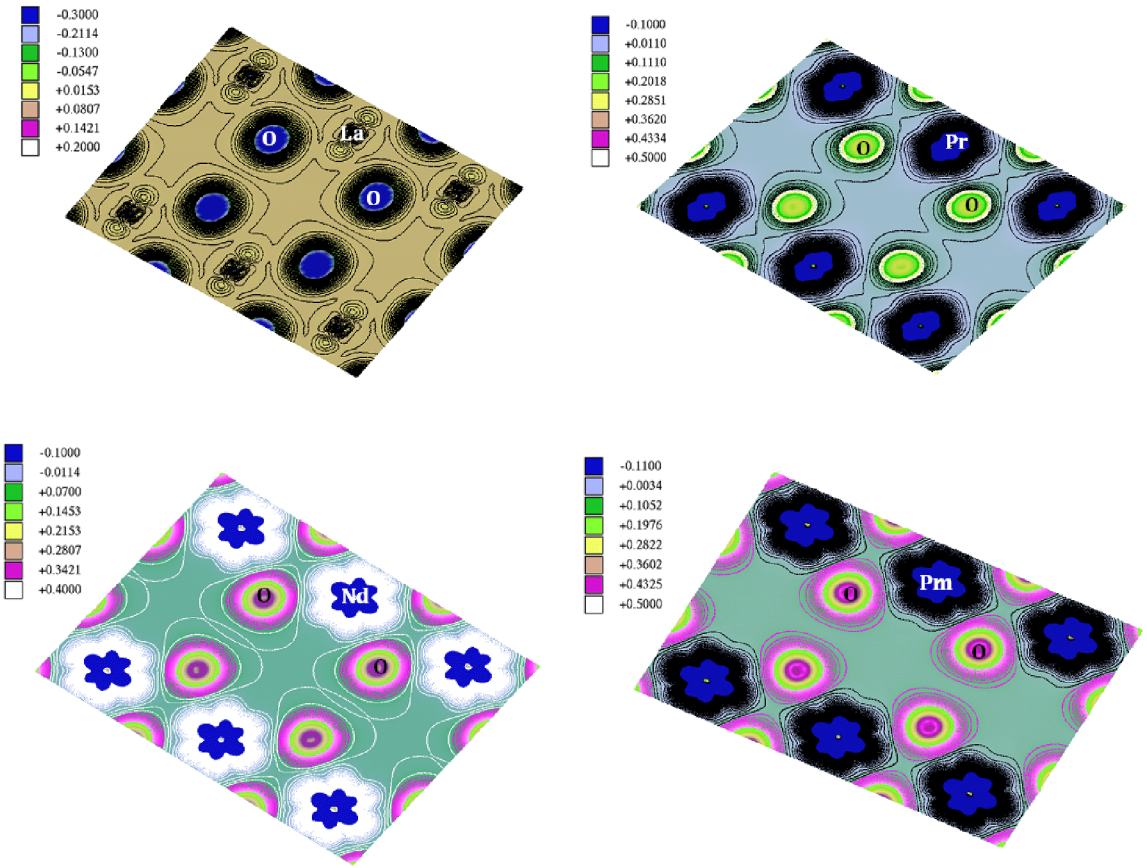

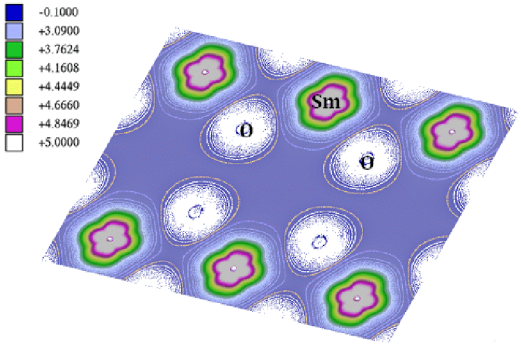
-0.1000
+3.0900
+3.7624
+4.1608
+4.4449
+4.6660
+4.8469
+5.0000
Sm
O
O

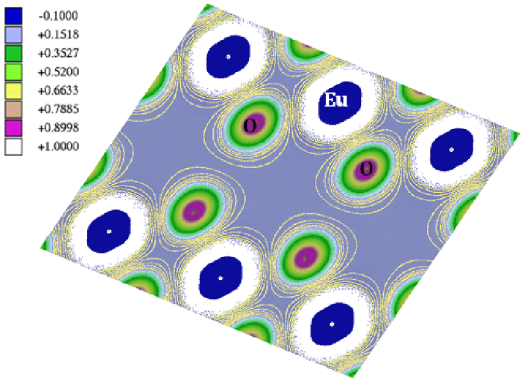
-0.1000
+0.1518
+0.3527
+0.5200
+0.6633
+0.7885
+0.8998
+1.0000
Eu
O
O

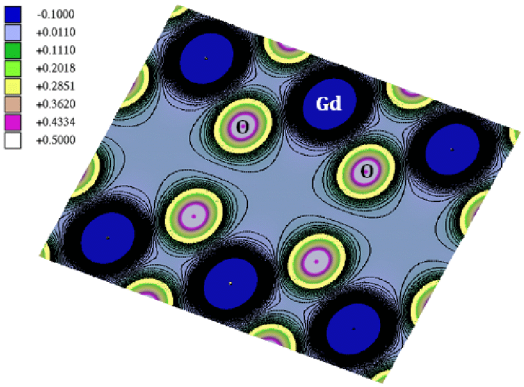
-0.1000
+0.0110
+0.1110
+0.2018
+0.2851
+0.3620
+0.4334
+0.5000
Gd
O
O

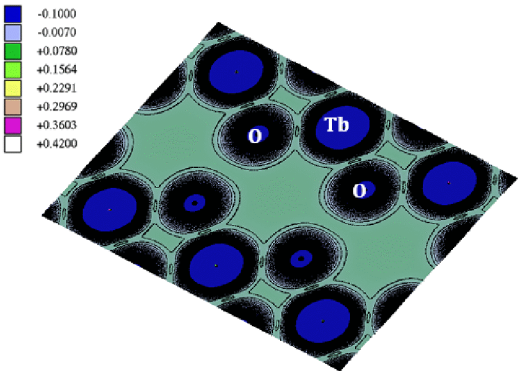
-0.1000
-0.0070
+0.0780
+0.1564
+0.2291
+0.2969
+0.3603
+0.4200
Tb
O
O

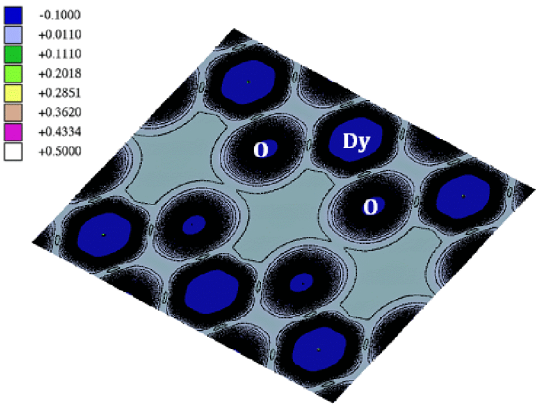
-0.1000
+0.0110
+0.1110
+0.2018
+0.2851
+0.3620
+0.4334
+0.5000
Dy
O
O

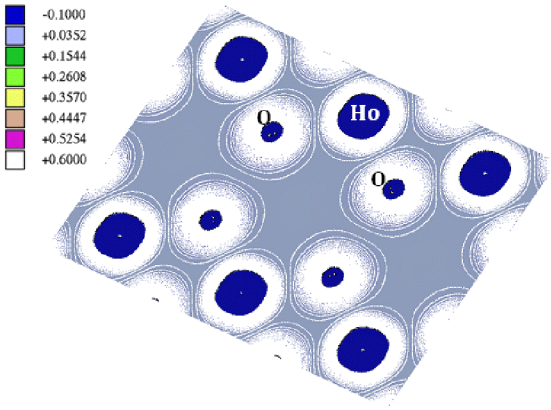
-0.1000
+0.0352
+0.1544
+0.2608
+0.3570
+0.4447
+0.5254
+0.6000
Ho
O
O

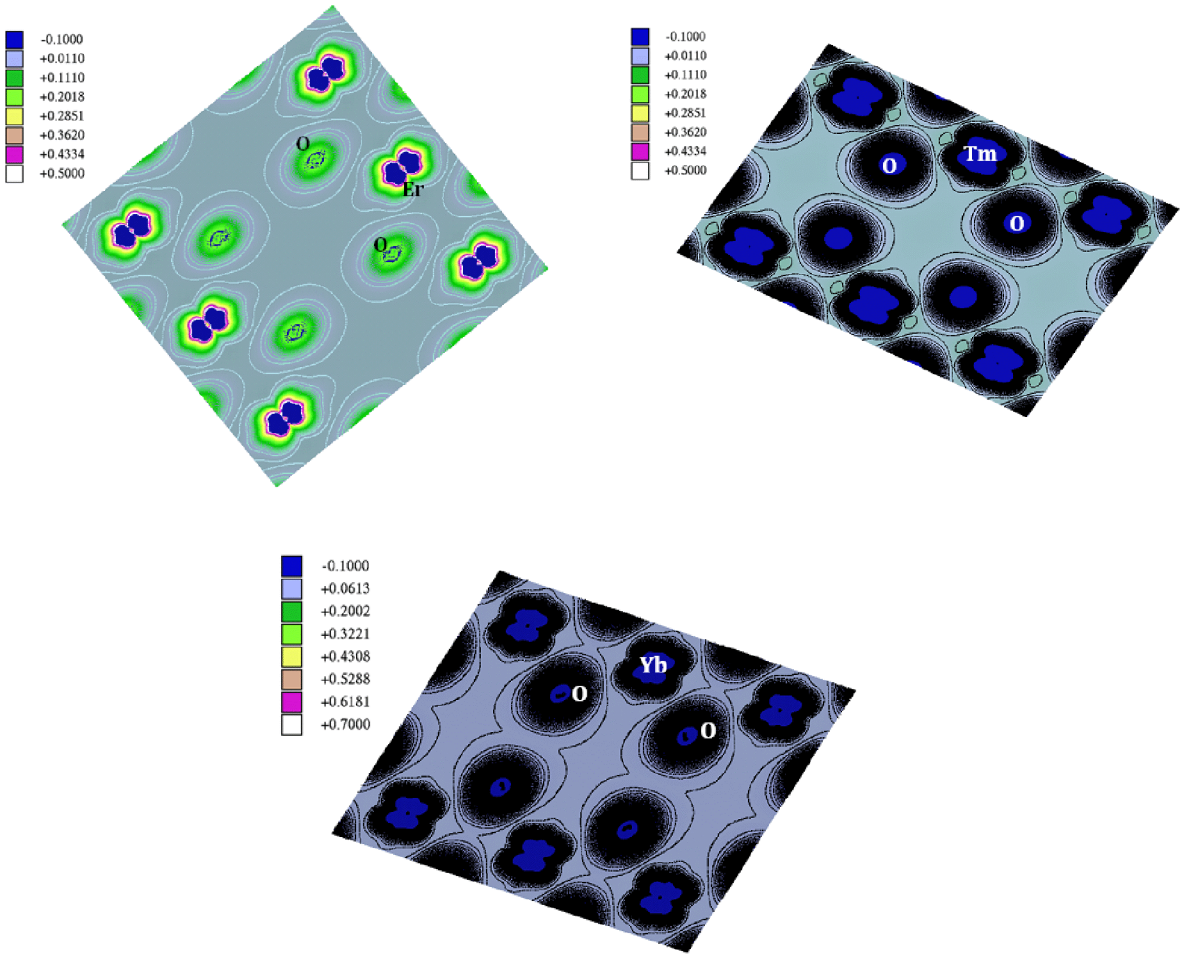

Figure 3.11: Spin density contours plot for REO_2 (RE = La, Pr, Nd, Pm, Sm, Gd, Tb, Dy, Ho, Er, Tm and Yb) .

Summary:

To conclude this chapter, we have performed detailed investigations on the structural, elastic, electronic, and magnetic properties of rare-earth dioxides compounds within the DFT framework based on full potential approaches. To achieve our goal, first we realized a set of simulations to predict Coulomb U_{eff} parameter used in LDA+U and GGA+U approaches for CeO_2. The GGA+U (WC) method gives better agreement than the LDA+U method. Consequently, we have applied of GGA+U and also the spin-orbit coupling, in order to investigate the structural, electronic, and magnetic properties of all rare earth dioxides. The calculation of the elastic constants shows the mechanical stability of all the considered systems. Moreover, the electronic structure study showed

that these structures are stable in ferromagnetic phases and good agreement with experiment can be obtained for the magnetic moment. We were able to give a trend on the magnetic moment as function of Z of rare earth atoms. It was important to give the magnetic contribution of the rare earth atom in each dioxide via the spin-density calculation, where the polarization on the first neighbor oxygen is observed.

References

[Andersson-07] D. A. Andersson, S. I. Simak, B. Johansson, I.A.Abrikosov,and N.V. Skorodumova, Phys. Rev 75, 035109 (2007).

[Anisimov-93] V. I. Anisimov, I. V. Solovyev, M. A. Korotin, M. T. Czyzyk, and G. A. Sawatzky, Phys. Rev. B 48, 16929 (1993).

[Antic-02] E. Antic-Fidancev, J. Holsa, and M. Lastusaari, J. Alloys Compds., 341, 82 (2002).

[Bergmann-74] H. Bergmann (ed.), GmelinHandbuch der AnorganischenChemie, Seltenerdelemente, Teil C1, No. 39, Springer-Verlag, Berlin, p.85, (1974).

[Birch-78] F. Birch, Phys. Rev. B 71 (1947) 809, J. Geophys. Res. 86, 1257(1978).

[Blaha-01] P. Blaha, K. Schwarz, G.K.H. Madsen, D. Kvasnicka, and J. Luitz, "*An Augmented-Plane-Wave+Local Orbitals Program for Calculating Crystal Properties* (K.Schwarz, Techn Wien, Austria, (2001).

[Boulesteix-82]C. Boulesteix, "*Defects and Phase Transformation Near Room Temperature in Rare Earth Sesquioxides*", in K.A. Gschneidner, Jr. and L. Eyring (eds.), Handbook of Physics and Chemistry of Rare Earths, Vol.5, Elsevier, Amsterdam, p.321, (1982).

[Choppin-89] G.R. Choppin, "*Chemical properties of the rare earth elements*", in J.-C.G. Bunzli and G.R. Choppin (eds.), Lanthanide Probes in Life, Chemical and Earth Sciences, Elsevier, msterdam, p.1, (1989).

[Cococcioni-05] M. Cococcioni and S. de Gironcoli, Phys. Rev. B 71, 035105 (2005).

[Dabrowski-01] J. Dabrowski, V. Zavodinsky, and A. Fleszar, Microelectron. Reliab.41, 1093 (2001).

[Divi-04] M. Divi, J. Rusz, and V. Nekvasil, Czech. J. Phys. 54, D291 (2004).

[Divi-05] M. Divi and J. Rusz, J. Magn. Magn.Mater.290-291, 1015 (2005).

[Duclos-88] S.J. Duclos, Y.K. Vohra, A.L. Ruo_, A. Jayaraman, G.P. Espinosa, Phys. Rev. B 38, 7755 (1988).

[Eyring-90]L. Eyring, "*The Binary Rare Earth Oxides: Synthesis and Identification*", in G. Meyer and L.R. Morss (eds.), Synthesis of Lanthanide and Actinide Compounds, Kluwer Academic Publishers, Dordrecht, 87, (1990).

[Eyring-98] L. Eyring, "*The Higher Oxides of the Rare Earths; A Paradigm for Solid State Chemistry*", in R. SaezPuche and P.A. Caro (eds.), Rare Earths, Editorial Complutense, Madrid, p.119, (1998).

[Fabris-05] S. Fabris, S. de Gironcoli, S. Baroni, G. Vicario, and G. Balducci, Phys. Rev. B 71, 041102 (2005).

[Fujimori-83] A. Fujimori, Phys. Rev. B 27, 3992 (1983); 28, 2281 (1983).

[Gennard-99] S. Gennard, F. Cor, and C. R. A. Catlow, J. Phys. Chem. B 103, 10158 (1999).

[Gerward-05] L. Gerward, J. Staun Olsen, L. Petit, G. Vaitheeswaran, V. Kanchana, A. Svanee, J. Alloys Comp. 400, 56 (2005)

[Gerward-05] L. Gerward, J. Staun Olsen, L. Petit, G. Vaitheeswaran, V. Kanchana, A. Svanee, J. Alloys Comp. 400, 56(2005).

[Gerward-93] L. Gerward, J.S. Olsen, Powder Di_r. 8, 127 (1993) .

[Gerward-93] L. Gerward, J.S. Olsen, Powder Diffr. 8 , 127(1993).

[Grimes-98] N.W. Grimes and R.W. Grimes, J. Phys. Condens. Matter, 10, 3029 (1998).

[Gschneidner-81] K.A. Gschneidner, Jr. ed., *Industrial Applications of Rare Earth Elements*, ACS Symposium Series 164, American Chemical Society, Washington, D.C., (1981).

[Guinier-64] A. Guinier, X-ray Diffraction, W.H. Freeman and Company, San Francisco and London, 1963; B.K. Vainshtein, Structure Analysis by Electron Diffraction, Pergamon Press, (1964).

[Gurel-06] T.Gurel, R.Eryigit, Phys. Rev. B 74, 014302 (2006)

[Haxel-06] H. G, Hedrick J, Orris J. Rare earth elements critical resources for high technology. Reston (VA): United States Geological Survey. (2006).

[Helen-01] C. Helen Aspinall. "*Chemistry of the f-block elements*".CRC Press.p. 8 (2001).

[Hill-52] R. Hill, P. Phys. Soc. Lond. A 65, 349 (1952).

[Hutcheson-79]D.P. Hutcheson, B. Venugopal, D.H. Gray, and T. Lucky, *J. Nutr.*, **109**, 702 (1979).

[Hyde-65] B.G. Hyde, D.J.M. Bevan, and L. Eyring, Internat. Conf. Electron Di_raction and Crystal Defects, Austral. Acad. Sci., C-4, p.11, (1965).

[Jiang-05] Y. Jiang, J. B. Adams, and M. van Schilfgaarde, J. Chem. Phys. 123, 064701 (2005).

[Kanoun-09] N. Kanoun-Bouayed, S. Goumri-Said, A. E. Merad, M. B. Kanoun, Mater Sci Forum Vol. 609, 167 (2009).

[Karnatak-87]R.C. Karnatak, J.-M.Esteva, H. Dexpert, M. Gasgnier, P.E. Caro and L. Albert, Phys. Rev. B 36, 1745 (1987)

[Kilbourn-93] B.T. Kilbourn, A Lanthanide Lanthology. Part I, A-L, Molycorp Inc., New York, 1993.

[Koelling-83] D.D. Koelling, A. M. Boring, and J. H. Wood, Solid State Commun. 47, 227 (1983).

[Liechtenstein-95]A. I. Liechtenstein, V. I. Anisimov, and J. Zaanen, Phys. Rev. B 52, R5467 (1995).

[Loschen-07] C. Loschen, J. Carrasco, K. M. Neyman, and F. Illas, Phys. Rev. B 75, 035115 (2007).

[Loschen-07] C. Loschen, J. Carrasco, K. M. Neyman, and F. Illas, Phys. Rev. B 75, 035115 (2007)

[Marabelli-87] M. Marabelli and P. Wachter, Phys. Rev. B 36, 1238 (1987).

[Mehrotra-07] S. Mehrotra and A. K. Bandyopadhyay, J. Alloys Compound. 436, 56 (2007).

[Monkhorst-76] H. J. Monkhorst and J. D. Pack, Phys. Rev. B 13,5188(1976)

[Mukin-91] L. Mukin, M. Chen, and S. Dechun, J. Rare Earths, 9, 294 (1991).

[Murnaghan-44] F. D. Murnaghan, Proc. Natl. Acad. Sci. U.S.A. 30, 244(1944)

[Nakajima-94] A. Nakajima, A. Yoshihara, and M. Ishigame, Phys. Rev. B 50, 13297 (1994).

[Nakajima-94] A. Nakajima, A. Yoshihara, M. Ishigama, Phys. Rev. B 50, 13297 (1994).

[Nakamatsu-95] H. Nakamatsu, T. Mukoyama, and H. Adachi, Chem. Phys. Lett., 247, 168-172 (1995).

[Nolan-05] M. Nolan, S. Grigoleit, D. C. Sayle, S. C. Parker, and G. W. Watson, Surf. Sci. 576, 217 (2005).

[Novk-07] P. Novk and M. Divi, Phys. Status Solidi B 244, 3168 (2007).

[Nye-85] J.F. Nye, "*Physical Properties of Crystals: Their Representation by Tensors and Matrices*" (Oxford University Press, Oxford, 1985).

[Ogasawara-91] H Ogasawara, A. Kotani, K. Okada and B.T.Thole, Phys. Rev. B 43, 854 (1991)

[Petit-07] L. Petit, A. Svane, Z. Szotek, and W. M. Temmerman, Appl. Phys. 106, 331 (2007).

[Reuss-29] A. Reuss, Z. Angew. Math.Mech. 9, 49 (1929).

[Sevik-09] C. Sevik and T. Cagin, Phys. Rev. B 80, 014108 (2009).

[Sevik-09] C. Sevik and T. Çagin, Phys. Rev. B 80, 014108(2009).

[Shafer-72]M.W. Shafer, J.B. Torrance, and T.J. Perry, J. Phys.Chem. Solids, 33, 2251 (1972).

[Shi-10] S. Shi, Y. Tang, C. Ouyang, L. Cui, X. Xin, P. Li, W. Zhou, H. Zhang, M. Lei, L. Chen, J. PhysChem Solids 71, 788 (2010).

[Silva-07] J. L. F. Da Silva, M. V. Ganduglia-Pirovano, J. Sauer, V. Bayer, and G. Kresse, Phys. Rev. B 75, 045121 (2007).

[**Skorodumova-01**] N.V. Skorodumova, R. Ahuja, S.I. Simak, I.A. Abrikosov, B. Johansson, and B. I. Lundqvist, Phys. Rev. B 64, 115108 (2001).

[Smith-89]L.W. Smith, J. Anim. Sci., 67, 2123 (1989).

[Spanier-01]J. E. Spanier, R. D. Robinson, F. Zhang, S.-W.Chan, and I. P. Herman, Phys. Rev. B 64, 245407 (2001).

[Tran-08] F. Tran, J. Schweifer, P. Blaha, and K. Schwarz, Phys. Rev. B 77, 085123 (2008).

[Trovarelli-02] A. Trovarelli, "*Structural Properties and Nonstoichiometric Behavior of CeO2",* in A. Trovarelli (ed.), Catalysis by Ceria and Related Materials, Imperial College Press, London, p.15, 2002.

[Van-06]E.van der Kolk and P. Dorenbos, Chem. Mater. 18, 3458 (2006).

[Villars-91] P. Villars and L. D. Calvert, "*Pearson's Handbook of Crystallographic Data for Intermetallic Phases*", 2nd ed. (ASM International, Ohio, 1991)

[Voigt-28] W. Voigt, Lehrbuch der Kristallphysik (Teubner, Leipzig, 1928).

[Wang-01] S. Wang, W. Wang, J. Zuo, and Y. Qian, Mater. Chem. Phys. 68, 246 (2001).

[Wang-03] X.H. Wang, Z.D. Zou, S.L. Song, and S.Y. Qu, J. Mater. Sci. Lett. 22, 713(2003).

[Wu-06] Z. Wu and R.E. Cohen, Phys. Rev. B. 73, 235116 (2006).

[Wuilloud-84] E. Wuilloud, B. Delley, W.-D. Schneider, and Y. Baer, Phys. Rev. Lett. 53, 202 (1984).

[Yang-04] Z. Yang and T. K. Woo, M. Baudin and K. Hermansson, J. Chem. Phys. 120, 7741 (2004).

[Zhang-96] J. Zhang, R.B. Von Dreele, and L. Eyring, J. Solid State Chem., 104, 21 (1993); J. Zhang, R.B. Von Dreele, and L. Eyring, J. Solid State Chem., 118, 133 (1995); J. Zhang, R.B. Von Dreele, and L. Eyring, J. Solid State Chem., 118, 141 (1995); J. Zhang, R.B. Von Dreele, and L. Eyring, J.Solid State Chem., 122, 53 (1996).

Chapter Four

Physical Properties of Oxynitrides

Abstract

In this chapter we are interested to the oxynitrides based on silicon and germanium: Si_2N_2O and Ge_2N_2O. We will initially present state of art of these compounds and their electronic structure. Then the structure, bonding, mechanical, thermodynamic and the optical properties will be studied using the DFT calculation by means of two methods, the full-potential linearized augmented plane-wave plus local orbitals and plane-wave pseudopotential. We will pay more attention to the electronic gap nature of Ge_2N_2O which was subject of various ab-initio contradictory studies. Furthermore, it was interesting to us to analyze the bonding via the charge densities and Mulliken population. We always compare our results with the experience whenever possible.

Attention, on n'est jamais à l'abri d'une découverte

André Verméglio

4.1. Introduction

With technological progress, natural materials become insufficient to meet increasing demands of product capabilities and functions. There are many combinations of metallic and non-metallic atoms that can combine to form ceramic components and also several structural arrangements are usually possible for each combination of atoms. This led scientists to invent many new ceramic materials to meet increasing requirements and demands in various application areas. In the past forty years, serious efforts were made to obtain an optimum composition and micro-structures of ceramics based on silicon nitride composites, which are an extremely wide class of materials possessing a unique combination of thermal, mechanical and electro-physical properties, and have found commercial application owing to interesting properties such as hardness, abrasion resistance, strength and thermal shock resistance **[Riley-77, Chelikowsky-77].**

In fact, the history of oxynitride glasses is not an old one. It was only in the late of seventies that some systematic studies on oxynitride glass were reported **[Loehman-79],** and this encouraged many researchers to explore this new field leading to accelerated research in the next decade of eighteens. The idea of the existence of oxynitride (ON) glass came in an indirect way, indirect in the sense that its preparation was not sought for from the constituents. On the other hand it was discovered that dense silicon-nitride based ceramic materials which were sintered with some metal oxide additives contained a grain boundary glassy phase, which was identified as the oxynitride glass **[Idrestedt-64, Labbe-77].** Silicon oxynitride Si_2N_2O is an important link between two major classes of materials of great technological importance, silicon nitride (Si_3N_4) and silicone dioxide (SiO_2), in recent years, Si_2N_2O has emerged as a new high–temperature ceramic material of many unique physical properties with a variety of potential applications such as high temperature electric insular, nuclear-reactor moderator or reflector, and materials for solid electrolytes. In microelectronic industry, the passivating dielectric films glow on Si may involve layers of amorphous forms of silicon oxynitride **[Ching-81]**. After, a high-pressure time-of-flight neutron diffraction studies have been carried out on orthorhombic Ge_2N_2O. The behavior of Ge_2N_2O is very similar to his isotopic Si_2N_2O **[Appl-79].**

4.1.1. State of art: theoretical studies

In this chapter we focused on the study of two oxynitrides, but before the study, we will get familiar with what is known of these systems. Intensive studies of the oxynitride phase Si_2N_2O were performed using ab-initio methods such as the non-self-consistent orthogonalized linear combination of atomic orbitals (OLCAO) method **[Ching-81],** by the self-consistent OLCAO method **[Xu-95]** and by the full-potential method (FLMTO) **[Ivanovskii-00,Ivanovskii-99].** The X-ray photoelectron spectroscopy and the X-ray Auger Electron Spectroscopy (AES) were used to study the electronic properties of silicon oxynitride lms **[Riviere-88, Chourasia-96].** Vibrational properties and pressure-induced structural transitions were theoretically studied **[Mirgorodsky-89],** and molecular-orbital studies of silicon oxynitride glasses, simulated by small clusters, were reported **[Murakami-88].**

Moreover, Kroll and Milko **[Kroll-03]** have investigated a manifold of possible structures of high pressure phases of crystalline silicon oxynitrides, Si_2N_2O, to elucidate the pressure-dependent phase of Si_2N_2O using DFT calculations**.** It revealed that the stability of the orthorhombic ternary phase of Si_2N_2O appears from 6 GPa and this phase is depending on the configurational entropy influence to the free energy of the solid state reaction. Most recently a systematic simulation study of the thermo-chemistry involved in the formation of new class of Si-Ge-N-O oxynitrides materials based on reactions of both $(SiH_3)_2O$ and $(GeH_3)_2O$ molecules, and the proposed SiH_3OGeH_3 analogue, in an ambient of ammonia was performed by Weng *et al* **[Weng-10].** They proposed two ordered phases such as $SiGeN_2O$ phase and pseudo-lamellar β-$SiGeN_2O$.

4.1.2. Current interest and motivations

In this chapter, we solve the gradient conjugate equations to systematically investigate the elastic, electronic, optical and lattice dynamics properties of Si_2N_2O and Ge_2N_2O with two major motivations. Firstly, we apply the recent amelioration reported on the full-potential (linearized) augmented plane waves plus local orbitals (FP-(L)APW+lo) in order to determine the electronic structure. We will pay more attention to the nature and the value of the band gap. In fact, the theoretical work performed by Ching and Ren **[Ching-81]** in the beginning of the eighties have revealed that Si_2N_2O have an indirect bandgap of 5.97 eV where the top of the valence band (VB) is at Γ point

and the bottom of the conduction band (CB) is at Z. Then, Xu and Ching **[Xu-95]** have employed the same method as used in ref. **[Ching-81]** (i.e. OLCAO method) but with self-consistent and they found that the band gap is a direct at Γ point. In the other hand, for the Ge_2N_2O compound, a direct band gap at Γ point was estimated to 3.78 (eV). Our second motivation is the calculation of the elastic constants and their derived mechanical properties. In fact, to the best of our knowledge, there is no work, neither theoretical nor experimental about the elastic constants and the existence of nitrogen will make it interesting to see their mechanical properties. Moreover, one can guess that the oxygen also plays a role in these properties. We will use exclusively plane wave pseudo-potential (PW-PP) method in order to compute the elastic constants. This method will help us also to determine the atomic *Mulliken* population, which will be useful to complete the bonding characterization discussion.

4.1.3. Structure description

The silicon-germanium-based oxynitrides crystallize in orthorhombic structure with space group $Cmc2_1$. The orthorhombic system is based on three unequal axes all at right angles to each other. All axes of the orthorhombic system can serve as two fold rotational axes. They as well can serve as the linear intersection of two perpendicular mirror planes. If all three perpendicular mirror planes are present, then the three crystallographic axes are defined by the intersection of the mirrors. All of this symmetry produces a center of symmetry (an inversion operation).

The Si_2N_2O (Ge_2N_2O) has an orthorhombic crystalline structure with lattice constants of a=8.843(9.312) Å, b=5.437(5.753) Å, c=4.835(5.102) Å. There are four formula units (twenty atoms) per unit cell. The basis of this structure is a three-dimensional net of SiN_3O tetrahedral **[Ching-81]**.

The overall structure is a network of sheets of Si_2N_2 or Ge_2N_2 interconnected by oxygen atoms. Nitrogen atoms are still surrounded by three Si (Ge) atoms in a trigonal structure while Si (Ge) retains its tetrahedral bonds with one of the N atoms being replaced by oxygen atoms **[Labbe-77].** These crystal structures refer to the sketches in Fig.4.1. The Si (Ge), N, and O atoms are in fourfold, threefold, and twofold coordinations, respectively.

The Si-O bond length in Si_2N_2O is longer than that in SiO_2, while the Si-N bond length is shorter than that in SiN4, In Ge_2N_2O crystal the Ge-O bond length is longer than the Ge-N bond length, but the opposite is true for Si_2N_2O crystal. In Si_2N_2O the average Si-N-Si angle is 120°, indicating an almost coplanar configuration for the N atom and the three bonded Si atoms. The corresponding structure is less coplanar in Ge_2N_2O with an average Ge-N-Ge angle of 118.5° furthermore the Ge-O-Ge angle of 122.3° is much smaller than the Si-O-Si angle of 147.7°. These differences in the crystal structure can account for their differences in the electronic structures **[Ching-81].**

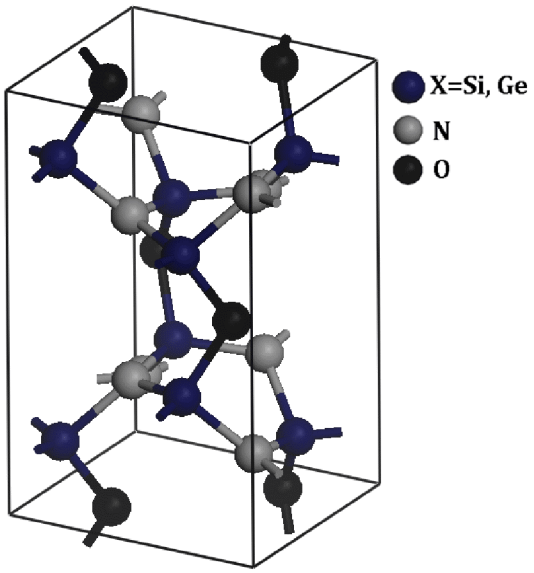

Figure4.1: Crystal structure ofX_2N_2O (X= Si and Ge)

4.2. Methodology and numerical details

The calculation procedure selected in this thesis is based on the combined use of two codes based on the density functional theory DFT. We start by calculations carried out using an all electron full-potential (linearized) augmented plane waves plus local orbitals (FP-(L)APW+lo) method as implemented in Wien2k code **[Blaha-01].** The influence of the exchange and correlation potential has been tested within the generalized gradient approximation (GGA-WC) using the scheme of Wu and Cohen **[Wu-06]** for exchange and correlation. Basis functions were expanded simultaneously as

spherical harmonic functions (inside non-over muffin-tin (MT) spheres centred at atomic sites) and as plane waves in the interstitial region. The l-expansion (azimuthal quantum number) of the non-spherical potential and charge density inside MT spheres was carried out up to l_{max} = 10. In order to achieve energy eigenvalue convergence, the wave functions in the interstitial region are expanded in plane waves with a cutoff of $K_{max}=8/R_{MT}$ (where K_{max} is the maximum modulus for the reciprocal lattice vector and R_{MT} is the average radius of the MT spheres). Moreover, local orbitals have been added for all atoms and valence states. The MT radii for Si_2N_2O and Ge_2N_2O were chosen to be 1.65, 1.75, 1.45 and 1.4 atomic units (a.u.) for Si, Ge, O and N, respectively. The self-consistency cycle was achieved taking 1500 points in the irreducible Brillouin zone. The convergence has been followed with respect to the energy and the density.

We used also the ab initio pseudo-potential density functional method based on the powerful code of CASTEP. Although a PW basis set can be very large, the use of optimized pseudopotential significantly reduces the number of plane waves needed to accurately represent the electronic states. Interactions of electrons with ions were represented by a Vanderbilt-type ultrasoft pseudopotential **[Vanderbilt-90].** As in FP-(L)APW+lo calculations, the electronic exchange correlation energy was treated under the GGA-WC **[Wu-06].** In the process of setting up the CASTEP run **[Clark-05],** all the possible structures are optimized by the BFGS algorithm proposed by Broyden, Fletcher, Gold-farb and Shannon, which provides a fast way of binding the lowest energy structure and supports cell optimization. The optimization is performed until the forces on the atoms are less than 0.01 eV/ A˚ and all the stress components are less than 0.02 GPa, the tolerance in the self-consistent field (SCF) calculation is 5:0*x*107 eV/ atom. Ultra-soft pseudo-potentials are expanded within a plane wave basis set with a 380 eV cutoff energy in the process of optimization. The k-points sampling are 7x7x7 according to the Monkhorst-Pack method. For all the optimized structures, the *Mulliken* charges and bond populations are investigated in detail with a method that projects plane wave states onto a linear combination of atomic orbitals basis set which is widely used to perform charge transfers and populations analysis.

4.3. Results and discussions

4.3.1. Structural properties:

The geometry has been optimized for the considered structures following the classical procedure: A set of different predefined volumes are chosen and for each of these volumes, different calculations are made for several *c/a* and *b/a* ratio values. The energy curves as function of the *c/a* and *b/a* ratios are then fitted with a polynomial function. This allows us to find a minimum in energy as a function of the *c/a* and *b/a* ratios for each selected volume. These minima give a set of energy as a function of the volume in which all other parameters are optimized. In the last step, this energy versus volume curves is fitted using the third-order Birch-Murnaghan equation of state **[Murnaghan-44, Birch-78]** to determine the optimized parameters.

$$E(V) = E_0 + \frac{9V_0B_0}{16}\left\{\left[\left(\frac{V_0}{V}\right)^{\frac{2}{3}} - 1\right]^3 B'_0 + \left[\left(\frac{V_0}{V}\right)^{\frac{2}{3}} - 1\right]^2 \left[6 - 4\left(\frac{V_0}{V}\right)^{\frac{2}{3}}\right]\right\} \qquad (4.1)$$

Where E_0 and V_0 are the energy and volume at equilibrium. B and B' are the bulk modulus and it's the pressure derivative. Our calculated values for a, b and c within PP-PW and FP-(L)APW+lo calculations are gathered in Table 4.1 along with the experimental data **[Idrestedt-64, Srinivasa-79, Srinivasa-77]** and theoretical calculations **[Kroll-03, Weng-10]** for comparison.

Table 4.1: Structural parameters *a, b and c* (Å), as resulted from PP-PW and FP-(L)APW+lo calculations compared to available experimental data and theoretical works.

		a	*b*	*c*
Si_2N_2O	PP-PW[a]	8.837	5.431	4.840
	FP-(L)APW+lo[a]	8.839	5.433	4.839
	Experiment[b]	8.843	5.437	4.835
	PAW-GGA-PBE [c]	8.894	5.477	4.845
	PPPW-GGA-PBE [d]	8.964	5.536	4.889
Ge_2N_2O	PP-PW[a]	9.308	5.748	5.101
	FP-(L)APW+lo[a]	9.312	5.753	5.102
	Experiment[e]	9.317	5.752	5.105
	PAW-GGA-PBE[c]	9.331	5.764	5.125

[a] Our work, **[b, c, d,e]**reference**[Srinivasa-77, Kroll-03, Weng-10, Srinivasa-79]**

Compared to the experiment, the calculated *a, b* and *c* lattice parameters from both methods were underestimated by around 0.06%, 0.07-0.11% and 0.09-0.1%, respectively, for Si_2N_2O. For Ge_2N_2O, a, b and c deviate from the experiment of about 0.05-0.09%, 0.02-0.07% and 0.06- 0.07%, respectively. It should be remarked that our calculations using both of the FP-(L)APW+lo and PP-PW methods give a good agreement compared to the experimental data.

4.3.2. Mechanical properties

In the study of materials, hardness or elasticity of the solid (material response to the forces (stresses) applied) must be considered, mechanical properties informs on the binding characteristics, mechanical stability and structure. The elastic stiffness determines the response of the crystal to an externally applied strain (or stress) and provides information about the bonding characteristics, mechanical and structural stability. In general, estimating elastic constants from first principles calculation is really tough because it requires accurate methods to evaluate the total energy or stress accompanying strain. Fortunately, state of the art first principles computational modeling permits us to reproduce the elastic properties of oxynitrides well.

Born Stability criteria:

The elastic behavior of a completely asymmetric material is specified by 21 independent elastic constants, the necessary number is determined by the symmetry of the material, and it is 9 for orthorhombic crystals.

The elastic stability is checked by the whole set of elastic stiffness constants that satisfies the Born-Huang criterion **[Born-82].** The criteria for mechanical stability are given by:

$$C_{11} > 0\,, C_{22} > 0\,, C_{33} > 0\,, C_{44} > 0\,, C_{55} > 0\,, C_{66} > 0 \tag{4.2}$$

$$[C_{11} + C_{22} + C_{33} + 2(C_{12} + C_{13} + C_{23})] > 0 \tag{4.3}$$

$$(C_{11}+, C_{22} - 2C_{12} > 0\,, (\,C_{11} + C_{33} - 2C_{13)} > 0\ \,, (C_{22} + C_{33} - 2C_{23}) > 0 \tag{4.4}$$

The calculated elastic constants allow us to obtain the macroscopic mechanical parameters, namely their bulk B and shear G moduli. There are two methods for calculating these modules, the first defined by the Voigt model **[Voigt-28]** (B_V, G_V), which are expressed as:

$$B_V = (1/9)[C_{11}+C_{22} + C_{33} + 2(C_{12}+C_{13}+C_{23})] \tag{4.5}$$

$$G_V = \left(1/15\right)[C_{11} + C_{22} + C_{33} + 3(C_{44} + C_{55} + C_{66}) - (C_{12}+C_{13} + C_{23})] \tag{4.6}$$

And secondly by the Reuss model (GR) **[Reuss-29]** by the equations:

$$B_R = \Delta\begin{bmatrix} C_{11}(C_{22} + C_{33} - 2C_{23}) + C_{22}(C_{33} - 2C_{13}) - 2C_{33}C_{12} + \\ C_{12}(2C_{23} - C_{12}) + C_{13}(2C_{12} - C_{13}) + C_{23}(2C_{13} - C_{23}) \end{bmatrix}^{-1} \tag{4.7}$$

$$G_R = 15\begin{Bmatrix} 4[C_{11}(C_{22} + C_{33} + C_{23}) + C_{22}(C_{33} + C_{13}) + C_{33}C_{12} - \\ C_{12}(C_{23} + C_{12}) - C_{13}(C_{12} + C_{13}) - C_{23}(C_{13} + C_{23})]/\Delta \\ +3[\left(1/C_{44}\right) + \left(1/C_{55}\right) + \left(1/C_{66}\right)] \end{Bmatrix}^{-1} \tag{4.8}$$

With

$$\Delta = C_{13}(C_{12}C_{23} - C_{13}C_{22}) + C_{23}(C_{12}C_{13} - C_{23}C_{11}) + C_{33}\left(C_{11}C_{22} - {C_{12}}^2\right) \tag{4.9}$$

Then Hill **[Hill-52]** show that these two elastic modules represent the extreme limits, the actual value can be approximated by the average Hill:

$$G_H = \frac{(G_v + G_R)}{2} \quad (4.10)$$

$$B_H = \frac{(B_v + B_R)}{2} \quad (4.11)$$

and Young's modulus Ymay be calculatedby the expression:

$$Y_H = \frac{9B_H G_H}{3B_H + G_H} \quad (4.12)$$

Then, Poisson's modulus was obtained from BH andGH as:

$$v = \frac{3B_H - 2G_H}{2(3B_H + G_H)} \quad (4.13)$$

The elastic anisotropy of the low-symmetry crystal can be described by the percentage anisotropy in compressibility (A_B) and shear (A_G) **[Hill-52]:**

$$A_B = \frac{B_V - B_R}{B_V + B_R}\ 100\% \quad (4.14)$$

$$A_G = \frac{G_V - G_R}{G_V + G_R}\ 100\% \quad (4.15)$$

To investigate the mechanical stability description of Si_2N_2O and Ge_2N_2O compounds, a set of zero-pressure elastic constants was determined from the stress of the strained approach implemented in CASTEP code **[Clark-05]** by taking into account the ionic relaxations in response to strain perturbations. The predicted elastic stiffness constants C_{ij} are summarize in Table 4.2. The elastic stability is checked by the whole set of elastic stiffness constants that satisfies all the below conditions using the Born-Huang criterion **[Born-82].** Furthermore we show that the C_{11}, C_{33}, and C_{44} values of the Ge_2N_2O are lower (about 47-60%) than that of the Si_2N_2O compound. Indeed, our calculated bulk modulus, shear modulus, Young's modulus, and Poisson's ratio of Si_2N_2O and Ge_2N_2O compounds are summarized in the same table according to the Voight-Reuss-Hill bounds **[Hill-52].**

Table4.2: Calculated elastic constants, C_{ij} (in GPa), bulk modulus B_H (in GPa), shear modulus G_H, (in GPa), Young's modulus, Y (in GPa), and Poisson's ratio (ν) of Si_2N_2O and Ge_2N_2O systems.

	C_{11}	C_{12}	C_{13}	C_{22}	C_{23}	C_{33}	C_{44}	C_{55}	C_{66}	B_H	G_H	Y	ν
Si_2N_2O	295	221	26	320	131	60	72	48	72	123.8	93.5	224.2	0.198
Ge_2N_2O	156	127	6.0	230	99	29	29	29	38	69.4	56.5	133.4	0.179

From this table, the bulk modulus agrees with that from the third-order Birch-Murnaghan equation of state. Then, it should be remarked that the shear and Young's modulus and of Si_2N_2O are higher than that of Ge_2N_2O. In fact, no measured values of the quantities in table 4.2 are available in the literature. The larger shear modulus of Si_2N_2O is mainly due to its larger C_{44}, which is about one time that of Ge_2N_2O.

Our calculated value for the bulk modulus of Si_2N_2O, 123.8 GPa, agrees well with the experimental value of 127 GPa **[Srinivasa-77]** obtained via neutron diffraction at low-pressures (P < 3 GPa), and somewhat overestimate the value of 115 GPa recently obtained by Haines et al **[Haines-08]** using an extended compression range (P < 50 GPa). Haines et al. also reported an anomalously small value for the bulk modulus derivative (B') about 1.2, which they ascribe to the possible effect of non-hydrostatic stress in their experiments. This discrepancy may be related to the experimental uncertainties reported in ref **[Haines-08]** that are quite large at high pressures. Then, when comparisons are performed with the bulk modulus results of Weng and al **[Haines-08],** 129.1 GPa and Kroll et al **[Haines-08],** 130 GPa, the differences are smaller and range between an underestimation by 4.1% and 4.7%, respectively. Again, the bulk modulus of Ge_2N_2O has also determined experimentally **[Srinivasa-79]** from compressibility to be about 101 GPa, which is smaller than our calculated value.

The elastic anisotropy (A) of crystals is also important for their mechanical applications. The elastic anisotropy of the low-symmetry crystal can be described by the percentage anisotropy in compressibility (A_B) and shear (A_G) **[Hill-52-Kanoun09**]. For A_B and A_G, the values of 0 and 1 (100%) represent the elastic isotropy and the largest anisotropy. Comparing the average A_B= 1.21% with A_G= 5.42% for Si_2N_2O, we find it less anisotropic in compression and shear. For Ge_2N_2O, the A_B= 2.55% and A_G=11.55%,

indicate it is elastically isotropic in compression and greatly anisotropic in shear. We can deduce that the Ge_2N_2O compound is less anisotropic than the Si_2N_2O one.

4.3.3. Electronic properties bonding characterization: charge density and Mulliken population

In this section, various properties will be presented; the electronic band structure (BS) of a solid describes those ranges of energy an electron is "forbidden" or "allowed" to have, the BS determines several characteristics about our compounds, the density of states (DOS) of a system who describes the number of states per interval of energy at each energy level that are available to be occupied. Also the electron density plays the key role and thus we use it for another mode of interpretation in DFT.

4.4. 3. 1. Band structures:

The one-electron energy eigenvalues (solutions of the Kohn–Sham equation) as functions of k-vectors define the band structure. The calculated electronic band structures of Si_2N_2O and Ge_2N_2O are displayed in Fig.4.2 (a and b), along the symmetry lines of the Brillouin zone (BZ). As we have mentioned before, that one of our motivations for studying these two oxynitride, is the nature of their band gap which was subject of various ab-initio contradictory studies, and we will explain this through this property, so, the band structures of these compounds show the appearance of a forbidden band gaps. Our calculations show (Fig.4.2a) that Si_2N_2O crystal is an insulator with a rather large value of a direct band gap equal to 5.1 eV. The band gap (Eg) is found to be direct at Ґpoint, which is in good agreement with the experimental values of Eg (5.2- 5.6 eV) **[Ivanovskii-00]** and the theoretical result obtained by the OLCAO method (5.2 eV) **[Ching-81],** but it is bigger than the value obtained from the FLMTO method (3.24 eV)**[Ivanovskii-00, Ivanovskii-99]** and by projector augmented wave (PAW) method (4.86 eV) **[Xu-95].**

The band structure of Ge_2N_2O (Fig. 4.2b) is characterized by an indirect band gap of 2.65 eV between the maximum of the valence band at the S point and the conduction band minimum at the Ґpoint. Our results disagree with those reported previously by Ching et al **[Ching-81]** and Weng et al **[Weng-10].**

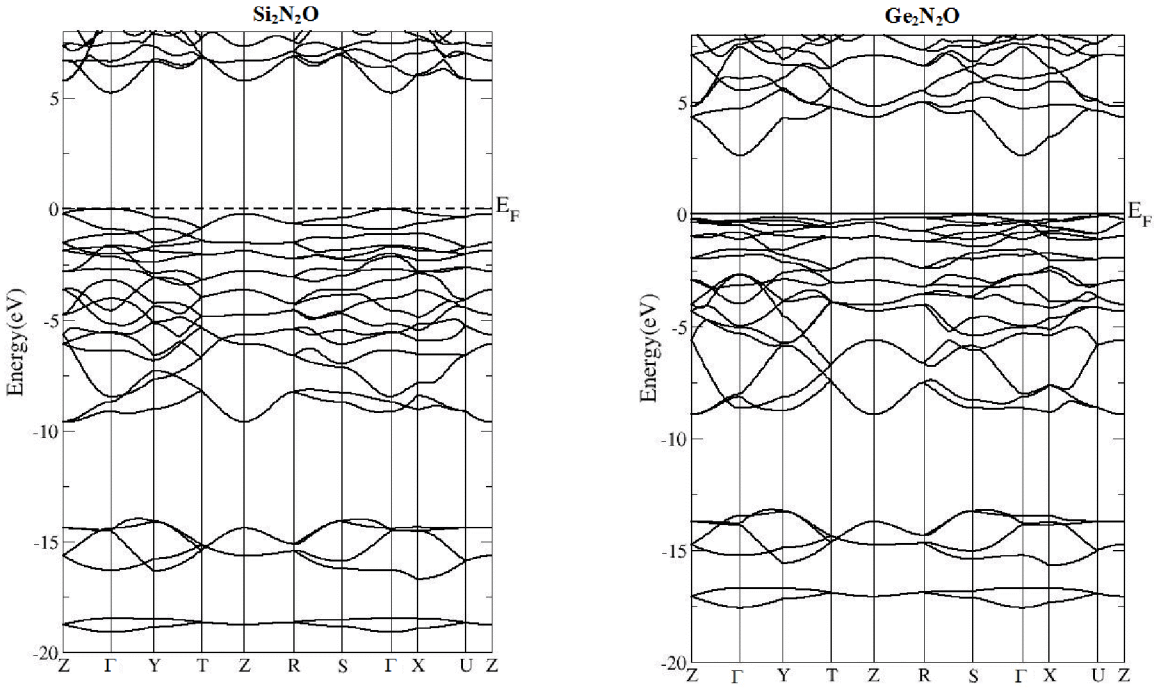

Figure 4.2: Band structure of (a) Si_2N_2O and (b) Ge_2N_2O.

4. 3.3. 2. Densities of states.

In order to assess the results obtained with the band structures calculations, we present in Fig.4.3 (a,b) the densities of states which have been computed by the improved tetrahedron method (which requires many k points) **[Blochl-94].** From the eigenvalues and eigenvectors solved at sufficient number k-points in the BZ, the total DOS can be projected into its partial components (PDOS) with respect to the different atoms which are useful for the interpretation of chemical bonding. Figures 4.3 (a and b) show the calculated total and partial densities of states of both Si_2N_2O and Ge_2N_2O systems. As can be seen, for both compounds there are three valence regions: the lowest energy band extends over a small interval of energy around -18 eV(-17.5 eV) for Si_2N_2O(Ge_2N_2O), is mainly composed of the O s with mixture of Si/Ge s states, the next band occur between -13 and -17 eV are mostly due to N *s* and Si/Ge*s*, and *p* states with a minor admixture of Ge *d* states. The upper valence band which is wider for a range of -9

eV up to Fermi level consists of hybridized *p* states of Si/Ge, N and O atoms, the Si/Ge *s* and Ge *d* states are contributing to this valence band. Note also that the contribution of Ge *d* states is quite small compared to Ge *p* states. Moreover, the unoccupied conduction band separated from the valence band by an energy gap of 5.1 eV in the case of Si_2N_2O, is made up of antibonding Si *3p* with a slight contributions of N *2p* states. While for Ge_2N_2O, the conduction band is composed of the antibonding Ge 4*p*, Ge 3*d* and N *2p* states. It can be noted that the conduction band minimum of Si_2N_2O possesses *p* character, while in Ge_2N_2O the unoccupied Ge *s* states dominate this energy rang.

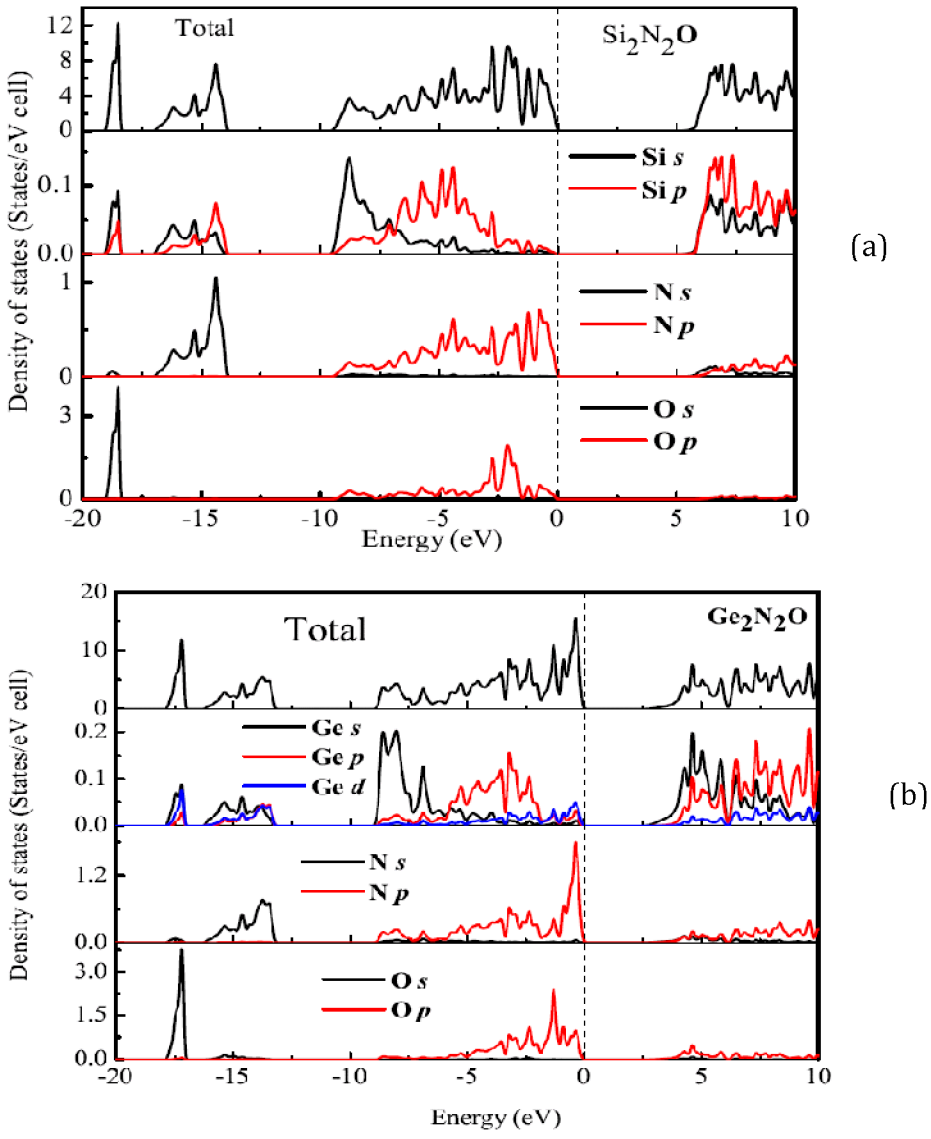

Figure 4.3: Total and partial densities of sates of (a) Si_2N_2O and (b) Ge_2N_2O. The origin for energy is at the Fermi level.

4.3. 3. 3. Electronic charge densities.

The charge density distribution is an important property of solids in the fact that provide a good description of the chemical properties. The investigation of chemical trends in solid-state properties appears as an extremely useful part of new material research. Performing those calculations, we try to gain some information about the Si_2N_2O oxyitrides and his hypothetical Ge_2N_2O. The bonding mechanism can be described based on the electronic density of charge calculations, So, To investigate the charge transfer of these compounds, we have calculated the charge densities in plane [111] shown in Fig. 4.4 (a and b). As we can see, the charge transfer from Ge to N and O atoms is more important in the Ge_2N_2O than in Si_2N_2O. When we analyze more carefully these maps, we may observe that the charge density distribution is essentially non-spherical in the case of Si_2N_2O and this behavior is more accentuated in Ge_2N_2O system.

Furthermore, the bonds between Si-O and Si-N in Si_2N_2O and Ge-O and Ge-N in Ge_2N_2O (as presented in Fig.4.4 (a,b,c and d)) are strongly covalent. The charge density along Ge-N bonds is more pronounced for the Germanium oxynitrides, this is dueto the stronger hybridization of covalent Ge-N and Ge-O bonds. These conclusion correlate with the full potential linear muffin-tin orbital (FP-LMTO) method performed on C_2N_2O and Si_2N_2O systems **[Ivanovskii-00]** and agree well with conclusion drawn from the bond population analysis reported in ref. **[Yuryvea-99].**

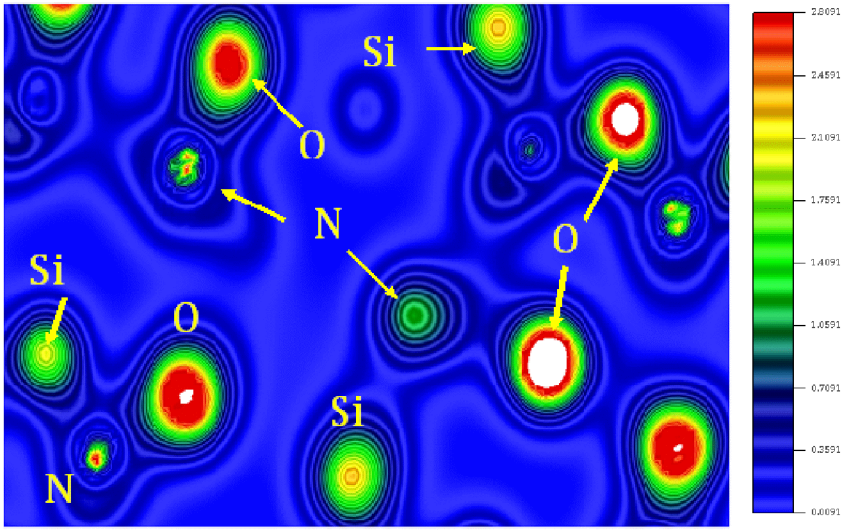

(a)

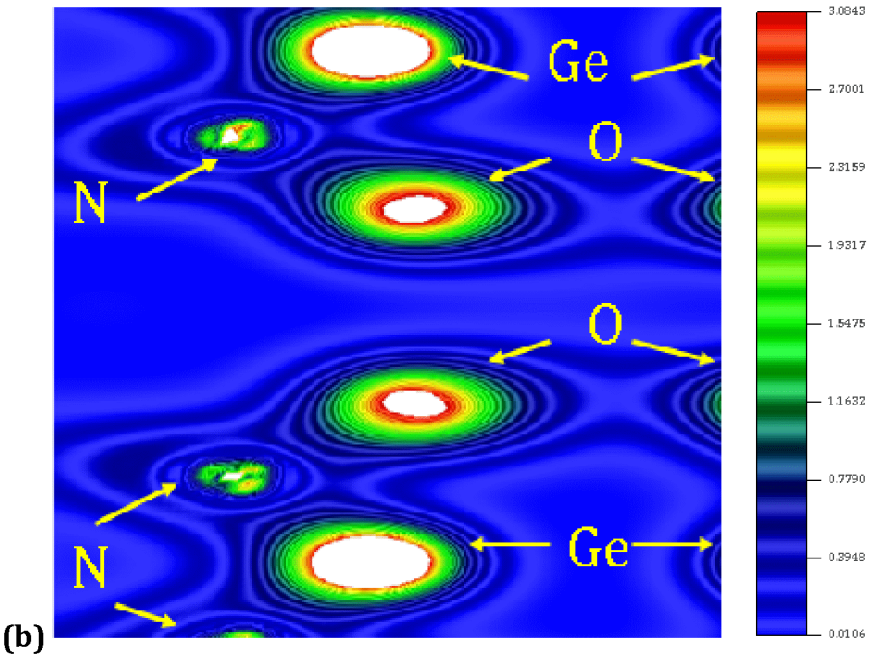

(b)

Figure4.4 Calculated valence charge density of (a) Si_2N_2O and (b) Ge_2N_2O

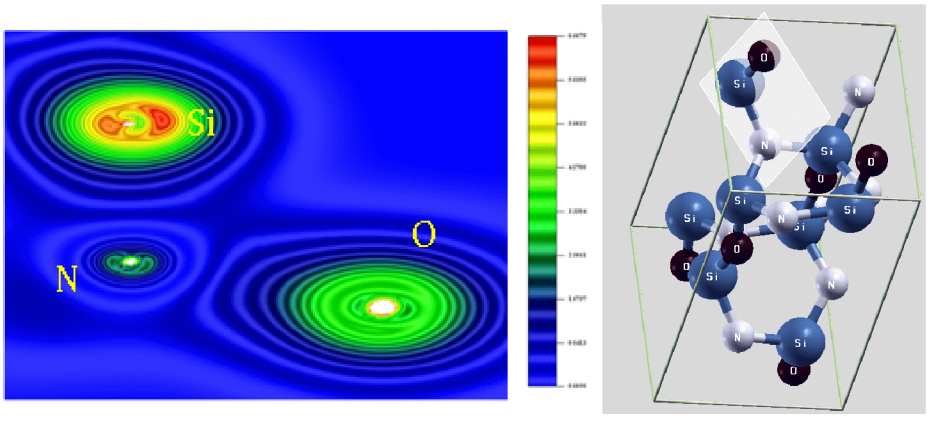

(a)

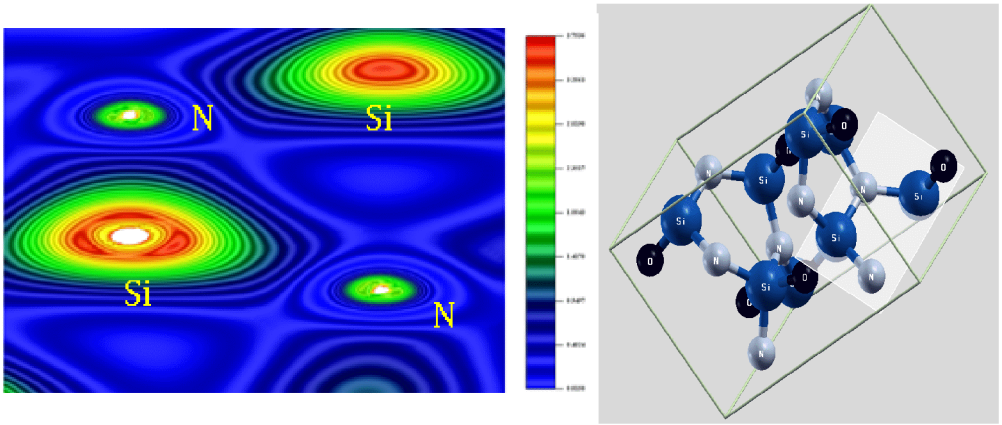

(b)

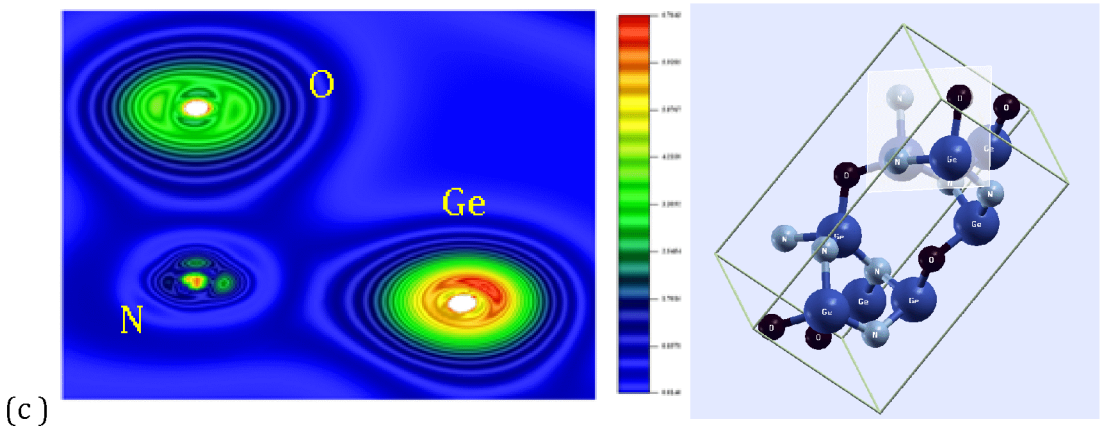

(c)

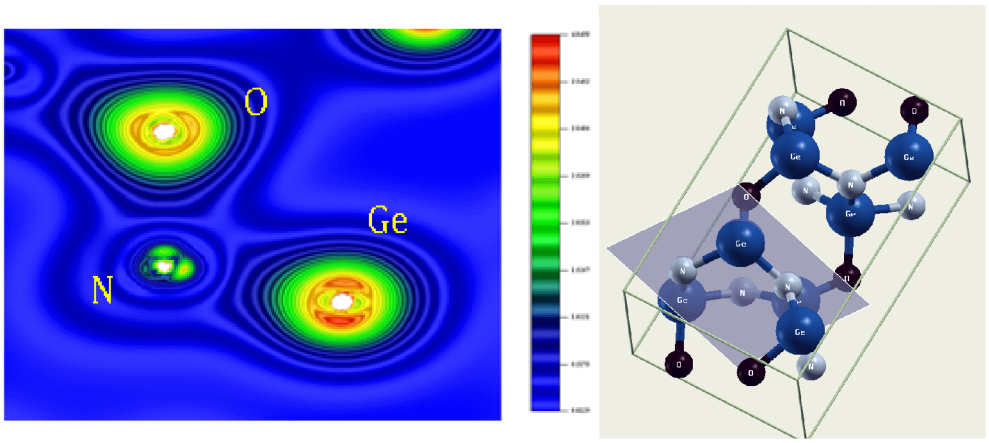

(d)

Figure 4.5: Calculated valence charge density of selected plane in (a,b) Si_2N_2O and (c,d) Ge_2N_2O.

4.3. 3. 4. Mulliken population analysis

For discussion of bonding mechanism of the structures, we have calculated *Mulliken* bond populations and bond lengths in unit lattices of Si_2N_2O and Ge_2N_2O. The results for *Mulliken* populations along with bond length are given in Table 4.3 Chemically, the positive *Mulliken* population values correspond to bonding character and negative values are related to an anti-bonding character of these systems. Furthermore, if the value of *Mulliken* bond population is close to zero, the ionic interaction increases between two atoms forming the bond. Generally, a high value of positive population indicates a high degree of covalency in the bond. As seen from Table 4.3, two different bonding characters take place in the atomic interactions of the both systems, Si(Ge)-O, N-O, N-Si(Ge) and N-N, one group of O-Si(Ge) and N-Si(Ge) bonds are

covalent, and N-O, N-N are ionic for both systems. It is interesting to note that in Si_2N_2O the Si-Si bonds are also ionic as well as the Ge-Ge interaction. We may observe also that the bond population of the Ge-O (1.878) bond is clearly much larger than that of the Si-O (1.624) but with same bond population. When we compare the N-O and N-N bonds interaction in Si_2N_2O and Ge_2N_2O systems, we observe a small but negative N-O and N-N population, which indicates a repulsive overlap of oxygen and nitrogen shells in both considered systems. In both systems, the anti-bonding character is induced between N-O, N-N and Si-Si (Ge-Ge) atoms in Si_2N_2O (in Ge_2N_2O). Moreover, we report the calculated *Mulliken* atomic population for both structures. The *Mulliken* charges are determined to be -1.08e and -1.48e for N atoms, -0.79e and -1.14e for O atoms and 1.48e and 2.05e for Si and Ge atoms for Si_2N_2O and Ge_2N_2O systems, respectively. Both the values of Si and Ge *Mulliken* charges are representative of the concurrent ionic and covalent bonding in Si_2N_2O and Ge_2N_2O systems.

Table 4.3: Atomic Mulliken charges and Mulliken overlap populations calculated from PW pseudopotential calculations.

Si_2N_2O			Ge_2N_2O		
Species	population Mulliken	Bond length	Species	Mulliken population	Bond length
O-Si	0.55	1.624	O-Ge	0.52	1.878
N-Si	0.63	1.724	N-Ge	0.68	1.846
N-O	-0.16	2.740	N-O	-0.14	2.867
N-N	-0.21	2.815	N-N	-0.14	2.993
Si-Si	-0.28	2.949	Ge-Ge	-0.31	2.997

4.3.4. Optical properties

The optical properties of crystalline Si_2N_2O and Ge_2N_2O were not well studied at all due to the lack of single-crystal samples until the publication of some limited optical measurement more than 20 years ago**[Baak-82].** In theoretical side, except the work of Xu and Ching **[Xu-95]** about the optical properties of Si_2N_2O, we are not aware of any serious numerical calculation of the optical properties of both Si_2N_2O and Ge_2N_2O crystals. Based on the FP(L)APW+lo method and GGA approach, we have calculated

different optical functions such as imaginary and real parts of the dielectric function, the reectivity spectra and the loss function. Since the considered systems crystallize in the orthorhombic structure space group Cmc21, the dielectric tensor has three components corresponding to the electric field $\vec{E}$ being along the *a, b,* and *c*-crystallographic axes. These are the complex tensor components: $\varepsilon^{xx}(\omega)$, $\varepsilon^{yy}(\omega)$ and $\varepsilon^{zz}(\omega)$. The imaginary part of these three complex components are $\varepsilon_2^{xx}(\omega)$, $\varepsilon_2^{yy}(\omega)and\varepsilon_2^{zz}(\omega)$. Measurements of the dielectric properties are normally done on single crystals. Sometimes experiments are performed with light vector $\vec{E}$parallel or perpendicular to the c-axis. The experimentally determined dielectric functions are then $\varepsilon_2^{\perp}(\omega)and\varepsilon_2^{\parallel}(\omega)$. These are related to the above mentioned components by **[Adachi-99]:**

$$\frac{\varepsilon^{xx}(\omega)+\varepsilon^{yy}(\omega)}{2} = \varepsilon_2^{\perp}(\omega) \tag{4.16}$$

And

$$\varepsilon_2^{zz}(\omega) = \varepsilon_2^{\parallel}(\omega) \tag{4.17}$$

The imaginary part $\varepsilon_2^{xx}(\omega)$, $\varepsilon_2^{yy}(\omega)$ and $\varepsilon_2^{zz}(\omega)$ of theoptical function's dispersion completely defines the linear optical properties. These are shown at Fig. 4.6. Broadening is taken to be 0.1 eV which is traditional for oxide crystals and this value is typical of the experimental accuracy. All the optical properties are scissors corrected **[Levine-73],** which is the difference between the calculated and measured energy gaps. It is a consequence of a fact that the DFT calculations usually underestimate the energy gaps. A very simple way to overcome this drawback is to use the scissors correction, which merely brings the calculated energy gap close to the experimental gap.

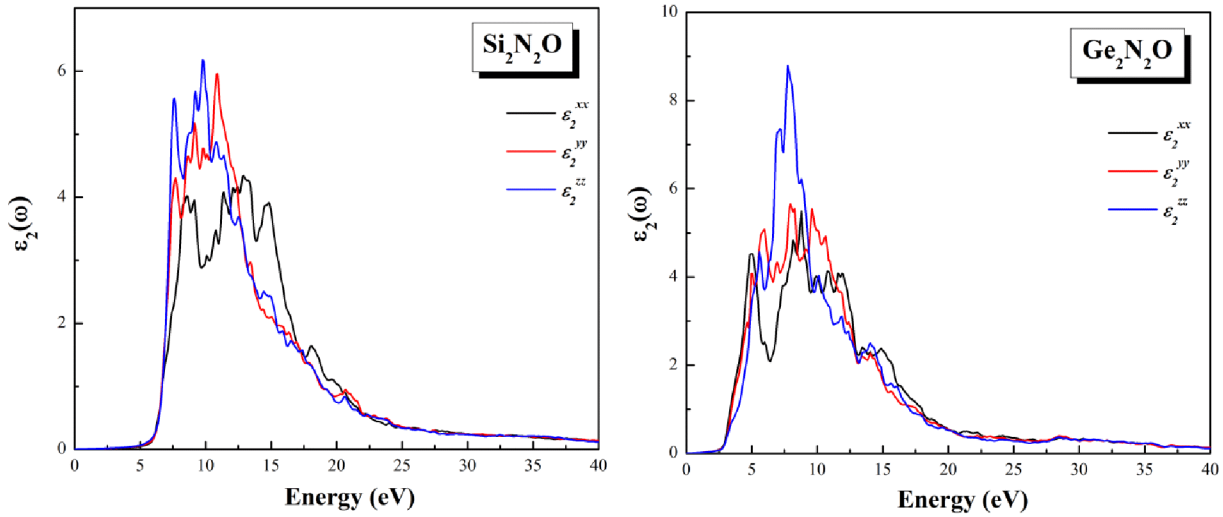

Figure4.6: Calculated $\varepsilon_2^{xx}(\omega)$ (dark solid curve), $\varepsilon_2^{yy}(\omega)$(red dashed curve) and $\varepsilon_2^{zz}(\omega)$(blue solid curve) spectra.

From Fig. 4.6, one can see that the edge of optical absorption (fundamental absorption edge) for $\varepsilon_2^{xx}(\omega)$, $\varepsilon_2^{yy}(\omega)$and $\varepsilon_2^{zz}(\omega)$ are located at 5.6 eV and 4.7 for Si_2N_2O and Ge_2N_2O, respectively. These edges of optical absorption give the threshold for direct optical transitions between the top of valence band and bottom of conduction band. All the components$\varepsilon_2^{ii}(\omega)$(ii= xx, yy and zz) display one principal peak situated around 14.0, 12.0, and 10.0 eV for Si_2N_2O and 11.0, 11.5 and 10.0 eV for Ge_2N_2O. Some insignificant/significant humps are situated around these peaks. One can see a considerable anisotropy between these three components of the frequency dependent dielectric function. In order to identify the spectral peaks in the linear optical spectra we considered the optical transition matrix elements. We used our calculated band structure and density of states to indicate the transitions, indicating the major structure for the principal components$\varepsilon_2^{ii}(\omega)$. From the imaginary part of the dielectric function's dispersions $\varepsilon_2^{ii}(\omega)$ the real part $\varepsilon_1^{ii}(\omega)$(ii= xx, yy and zz), were calculatedusing Kramers-Kronig relations **[Tributsch-77].** The results of our calculated $\varepsilon_1^{ii}(\omega)$are shown in Fig. 4.7. The calculated $\varepsilon_1^{ii}(0)$ are listed in Table 4.4. Using the calculated imaginary and real parts of the dielectric function dispersions one can evaluate other optical properties such as reectivity spectra R(ω), and loss function L(ω). Moreover, the square root of $\varepsilon(0)$is a good estimate of the refractive index. We list our calculated values as well as the

available experimental data **[Gritsenko-78, del Giudice-90]** for non-stoichiometric amorphous samples of Si_2N_2O. The general agreements are very consistent.

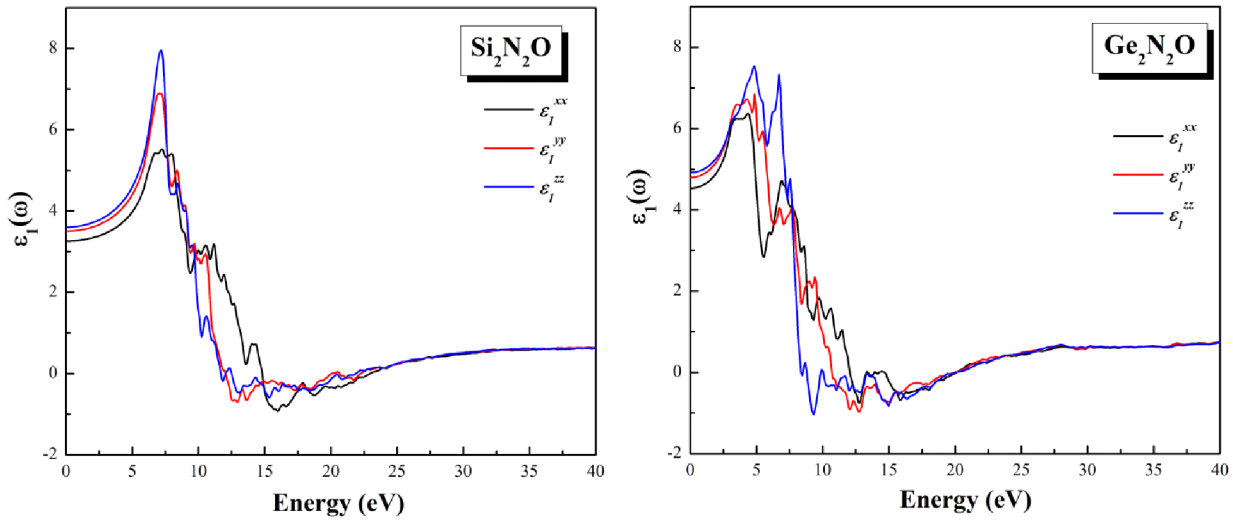

Figure4.7: Calculated $\varepsilon_1^{xx}(\omega)$ (dark solidcurve), $\varepsilon_1^{yy}(\omega)$ (red dashed curve) and $\varepsilon_1^{zz}(\omega)$ (blue solidcurve) spectra.

Table4.4: Calculated dielectric constants$\varepsilon_1^{\perp}(\omega)$, $\varepsilon_1^{\parallel}(\omega)$and refractive index, n, for Si_2N_2O and Ge_2N_2O compounds.

		$\varepsilon_1^{\parallel}(0)$	$\varepsilon_1^{\perp}(0)$	$\varepsilon_1(0)$	n
Si_2N_2O	Our work	3.06	2.88	2.92	1.71
	Calculation[a]	3.33	3.36	3.34	1.83
	Experiment[b]				1.55-2.91
	Experiment [c]				1.68
Ge_2N_2O	Our work	3.52	3.36	3.46	1.86

[a]reference **[Xu-95],** [b]reference **[Gritsenko-78],** [c] reference**[del Giudice-90]**

4.3.5. Lattice dynamics and thermodynamic properties

Dynamical properties were obtained by the use of linear response method, within density functional perturbation theory (DFPT) **[Gonze-97, Baroni-01].** Unlike the previous calculations performed with CASTEP **[Clark-05],** the calculations of phonons have been made using the norm-conserving pseudopotentials **[Vanderbilt-90]** as implemented in this code. In fact, DFPT is able to calculate of the second-order derivatives of the total energy with respect to atomic position, and thus the properties of phonon modes can be directly evaluated. Furthermore, phonons of a nonzero wave-vector play an important role in the thermo-physical properties of crystalline solids and the physics of many solid state phase transitions. Proving the mechanical stability of a crystal structure by testing for real frequencies requires a vibrational calculation over the full BZ and dispersion curves and densities of states are frequently required for comparison with inelastic neutron and X-ray scattering experiments. Our calculated dispersion curves and total densities of states of the phonon in Si_2N_2O and Ge_2N_2O are displayed in Fig. 4.10(a) and (b). There is LO-TO splitting at the Γ point due to coupling between the phonon modes and the electric field. It is important to further check the dynamical stability of Si_2N_2O and Ge_2N_2O from their phonon-dispersion curves. It is clear that no imaginary phonon frequency exists in the whole BZ, indicating the dynamical stability of our systems.

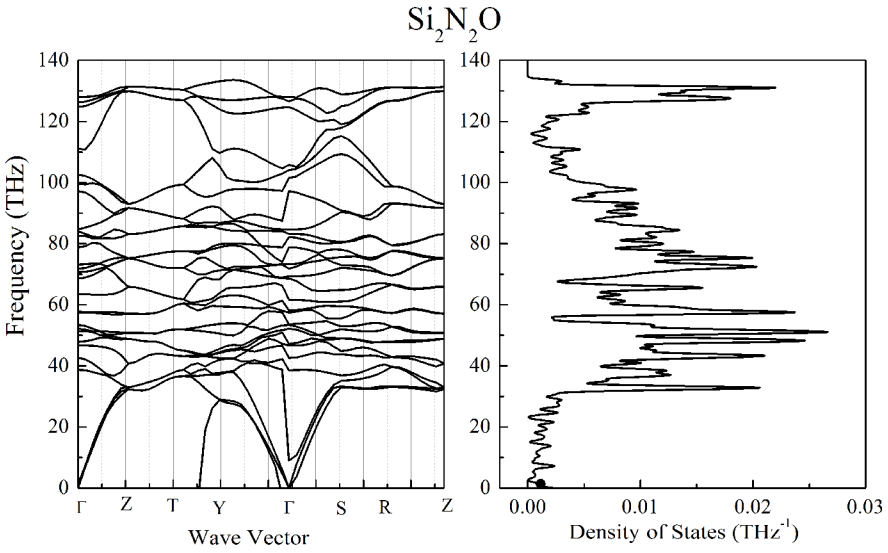

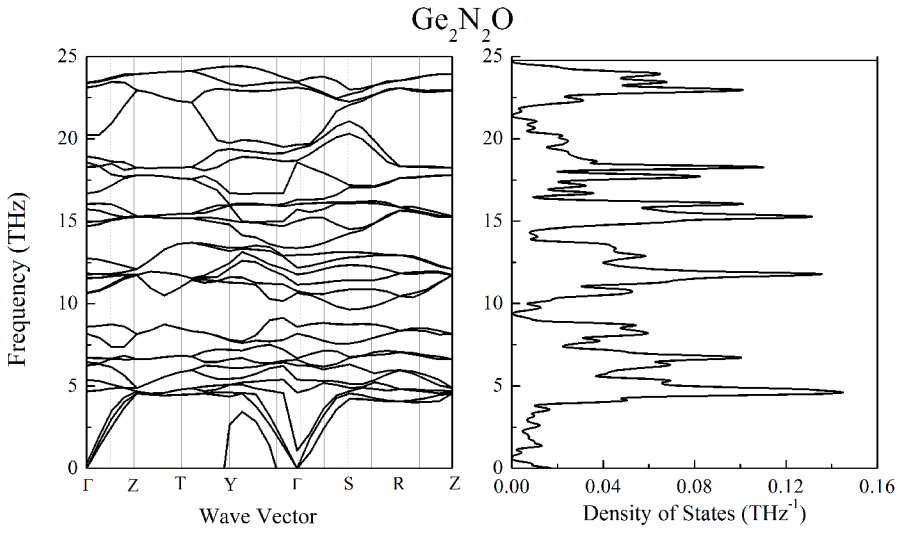

Figure 4.10: Dispersion curves of phonon and total phonon density of states for (a) Si_2N_2O and (b) Ge_2N_2O

Phonon calculations from DFPT calculation can be used to evaluate the temperature dependence of the enthalpy, entropy, free energy, and lattice heat capacity of a crystal in a quasi-harmonic approximation. These results can be compared with experimental data (for example heat capacity measurements) or used to predict phase stability of different structural modifications or phase transitions. Are given in Fig.4.11 (a,b), the variations of the lattice heat capacity with temperature for Si_2N_2O and Ge_2N_2O respectively. It is suggested that the heat capacities C_v increase with the applied temperature. Below a temperature ~ 562 K for Si2N2O and ~ 441 K for Ge_2N_2O, C_v increases very rapidly with increasing temperature; Above these temperatures, C_v increases slowly with temperature and gradually approaches the Dulong-Petit limit owing to the ana-harmonic approximations of the Debye model **[Ashcroft-76].**

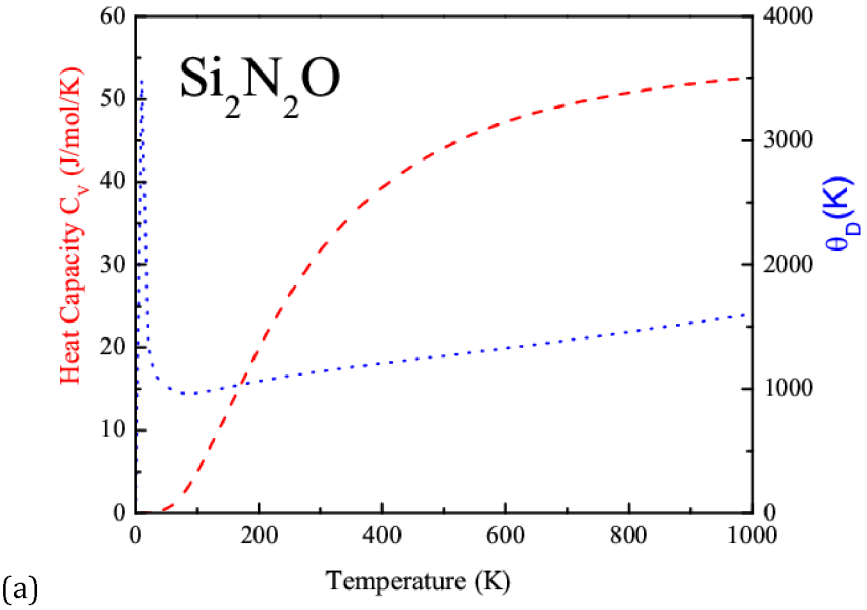

(a)

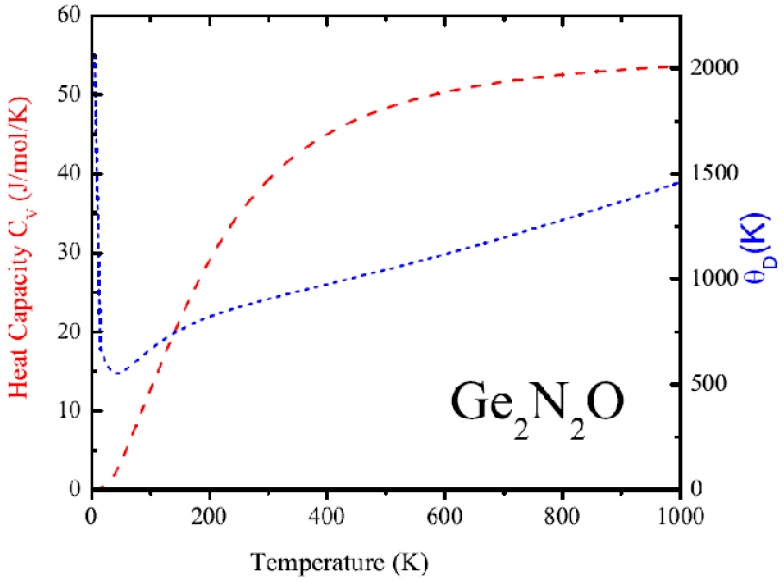

(b)

Figure4.11: Constant volume heat capacity Cv and temperature dependence of Debye temperature θ_D for (a) Si_2N_2O and (b) Ge_2N_2O.

Conclusion

We have performed a detailed investigation on the structural, elastic, electronic, and optical and lattice dynamic properties of Si_2N_2O and Ge_2N_2O compounds within the DFT framework based on two approaches full potential and pseudo-potential plane waves.

- The band structure of these oxynitrides states that these materials are semiconductors with a direct band gap of 5.1 eV at Γ for Si_2N_2O and an indirect

band gap about 2.65 eV between S and Γ' points for Ge_2N_2O. The moderate size of band gap places Si_2N_2O crystal in the class of semiconductors of large gaps rather than Ge_2N_2O insulator. An inspection of the Mulliken bond population shows that this material has mixed ionic-covalent character.

- Calculation of the complete set of zero-pressure elastic constants has been performed and satisfied the *Born* mechanical stability criteria, highlighting the fact that the Si_2N_2O and Ge_2N_2O structures are mechanically stables. In addition, their bulk and shear modulus are larger than those reported on III-V semiconductors like GaN and AlN.
- Optical properties of Si_2N_2O and Ge_2N_2O crystals were reported and compared with the available experimental and theoretical data. The optical properties namely the dielectric functions, refractive index were calculated as part of a material characterization. The typical goals of such calculations were to predict optical spectra of these materials under extreme conditions and to achieve better understanding of the optical properties in connection to their electronic structure.
- Vibrational density of states integrated across the Brillouin zone was used to compute thermodynamic properties including specific heat capacity and Debye temperature. Ab initio lattice dynamics calculations using DFPT methods were very well adapted to Si_2N_2O and Ge_2N_2O given for first time as prediction.

We expect that our results will be useful for future measurements on these systems and especially for mixing systems such as $Si_xGe_yN_2O$. In particular, solid Si-Ge-O-N phases may be immediately relevant in the emerging area of high-k gate materials for use in next generation high mobility Si-Ge based transistors **[Weng-10].**

References

[Adachi-99] S. Adachi, Optical properties of crystalline and amorphous semiconductors, Kluwer Academic Publishers, (1999).

[Appl-79]*J. Appl. Cryst.* Journal of Applied Crystallography **12**, 511 (1979).

[Ashcroft-76] N. W. Ashcroft and N. D. Mermin, Solid State Physics,Saunders College: Philadelphia (1976).

[Baak-82]T. Baak, Appl. Opt. 21, 1070 (1982).

[Baroni-01]S. Baroni, S. de Gironcoli, A. dal Corso, P. Giannozzi, Rev. Mod. Phys., 73, 515-562 (2001).

[Birch-78]F. Birch, Phys. Rev. B 71, 809 (1947), J. Geophys. Res. 86, 1257 (1978).

[Blaha-01] P. Blaha, K. Schwarz, G. K. H. Madsen, D. K.vanicka, J. Luitz, WIEN2K-An Augmented Plane Wave and Local Orbital Program for calculating Crystal Properties, edited by K. Schwarz, Vienna University of Technology, Austria,(2001).

[Blochl-94]P.E. Blochl, O. Jepsen and O. K. Andersen , Phys. Rev B 49, 16223 (1994).

[Born-82] M., K. Hang, Dynamical Theory and Experiments I, Springer Verlag Publishers, Berlin, 1982.

[Chelikowsky-77] J.R. Chelikowsky and M. Schluter, Phys. Rev. B. 15, 4020 (1977); S. Ciraci, and I. P. Batra, ibid. 15, 4923 (1977);E. Calabrese and W. B. Fowler, ibid. 18, 2888 (1978).

[Ching-81] W. Y. Ching and S. Y. Ren, Phys. Rev. B 24, 5788 (1981).

[Chourasia-96] A. R. Chourasia, S. J. Hood, and D. R. Chopra, J. Vac. Sci. Technol. A 14, 699 (1996).

[Clark-05]S. J. Clark, M. D. Segall, C. J. Pickard, P. J. Hasnip, M. J. Probert, K. Refson, M. C. Payne, Zeitschrift fuer Kristallographie 220(5-6) pp. 567-570 (2005).

[del Giudice-90]M. del Giudice, F. Bruno, T. Cicinelli and M. Valli, Appl.Opt. 29, 3489 (1990).

[Gonze-97] X. Gonze, Phys. Rev. B. 55, 10337 (1997).

[Gritsenko-78]V. A. Gritsenko, N. D. Dikovskaja and K. P. Magilnikoo,Thin Solid Films 51, 353 (1978).

[Haines-08] J. Haines, and M. Santoro, Phys. Rev. B 77, 144206 (2008).

[Hill-52] R. Hill, Proc. Phys. Soc. Lond. A 65, 349.(1952).

[Hill-52]R. Hill, Proc. Phys. Soc. Lond. A 65, 349(1952).

[Idrestedt-64]I Idrestedt and C. Brosset, Acta Chem. Scand. 18, 1879(1964).

[Ivanovskii-00] A. L. Ivanovskii, N. I. Medvedeva , O. Yu. Kontsevoi and G. P. Shveikin. phys. stat. sol. (b) 221, 647(2000).

[Ivanovskii-99] A. L. Ivanovskii, N. I. Medvedeva and G. P. Shveikin, Mendeleev Commun., 9(1), 34 (1999).

[Kanoun09]M. B. Kanoun, S. Goumri-Said, and A.H. Reshak, Comput.Mat. Sci 47, 491 (2009).

[Kroll-03] P. Kroll and M. Milko, Z. Anorg. Allg. Chem., 629, 1737 (2003).

[Labbe-77]J.C. Labbe, M. Billy, Materials Chemistry 2, 157-170 (1977). J. C. Labbe and M. Billy, C. R. Acad. Sci. Ser. C 277, 1173 (1973).

[Levine-73] B.F. Levine, Phys. Rev. B 7, 2600 (1973).

[Loehman-79]R. E. Loehman J. Am. Ceram. Soc. 62 491 (1979).

[Loughin-96]S. Loughin, R.H. French, L.K. De Noyer, W.-Y. Ching, Y.-N. Xu, J. Phys. D: Appl. Phys. 29, 1740 (1996).

[Mirgorodsky-89] A. P. Mirgorodsky, M. I. Barton, and P. Quintard, J. Phys.: Condens. Matter1, 10053(1989).

[Murakami-88]M. Murakami and S.Sakka, J. Non-Cryst. Solids 101, 271 (1988).

[Murnaghan-44] Murnaghan F D 1944 Proc. Natl. Acad. Sci. U.S.A. 30244

[Reuss-29] A. Reuss, Z. Angew. Math.Mech. 9, 49(1929).

[Riley-77] F. Riley, Nitrogen Ceramic (Noordho, Leynden, (1977).

[Riviere-88] J. C. Riviere, J. A. A. Crossley, and B. A. Sexton, J. Appl. Phys.64, 4585 (1988).

[Srinivasa-77]S. Srinivasa, L. Curtz, J. D. Jorgensen, T. G. Worlton, R. Beyerlein, and M. Billy, J. Appl. Crystallgr. 10, 146 (1977).

[Srinivasa-79]S. R. Srinivasa, L. Cartzj, J. D. Jorgensen, and J. C. Labbe, J. Appl. Cryst. 12, 511 (1979).

[Tributsch-77] H. Tributsch, Z. Naturforsch. A 32A, 972 (1977).

[Vanderbilt-90]D. Vanderbilt Phys. Rev. B 41 7892 (1990).

[Vanderbilt-90]D. Vanderbilt, Phys. Rev. B. 41, 7892 (1990).

[Voigt-28]W. Voigt, Lehrbuch der Kristallphysik, Teubner, Leipzig, 1928.

[Weng-10] C. Weng, J. Kouvetakis and A.V.G. Chizmeshya, Chem.Mater. 22, 3884 (2010).

[Wu-06] Z. Wu and R. E. Cohen, Phys. Rev. B. 73, 235116 (2006).

[Xu-95]Y. -N. Xu and W. Y. Ching, Phys. Rev. B. 51, 17379 (1995)

[Yuryvea-99]E. I., G. P. Shveikin and . L. Ivanovskii, Functional Mater. 6 , 640 (1999).

Conclusion

On ne fait jamais attention à ce qui a été fait : on ne voit que ce qui reste à faire

Marie Curie

This thesis has been concerned with the computational study of copper nitrides, rare earth dioxides and potentially important oxynitrides materials incorporating silicon and germanium. We have applied *ab-initio* calculations including the FP-(L)APW+lo and pseudopotential methods, based on DFT approach. We have presented an extensive investigation on the structural, electronic, elastic, electronic optical and dynamical properties and the relative stabilities of the bulk of these nitrides, dioxides and oxynitrides based systems. The main results of our work can be summarized as follow:

- For copper nitrides, ab *initio* calculations of structural, elastic, electronic, bonding, and thermal properties were performed for different cubic phases, zincblende, rocksalt, and fluorite phases. A concurrence between ionic and covalent character was observed in all phases. Structural and mechanical stabilities were examined by calculating the structure parameters and elastic constants. We paid more attention to the electronic properties and bonding and their relation to the possible covalent/ionic bonding characters. Using a quasi-harmonic model we have calculated the temperature effects on the thermal expansion parameters and specific heat observables.

- In the case of rare earth dioxides, we have performed a set of simulations to predict Coulomb parameter (U_{eff}) used in LDA+U and GGA+U approaches, especially for CeO_2. The GGA+U (WC) method gives better agreement than the LDA+U method. The application of GGA+U added to the spin-orbit coupling, on the electronic, magnetic and optical properties was detailed and demonstrated to be relevant for the correctness of our results. Elastic constants calculation proves the mechanical stability of the rare earth dioxides. The electronic structure description has shown that these structures are stable in ferromagnetic phases and an excellent agreement with experiment has been obtained for the magnetic moment. We were able to give a trend on the magnetic moments as function of the atomic number (Z) of the rare earth atoms. Magnetic contribution of the rare earth atom in each dioxide was achieved by analyzing the spin-density contours, where the polarization on the first neighbor oxygen was confirmed.

- For first time we report predictions on the silicon-germanium-based oxynitrides. Their bulk and shear modulus are larger than those reported on III-V semiconductors like GaN and AlN. We provided new information on the electronic nature of Si_2N_2O and Ge_2N_2O. In fact, the FP-LAPW+lo method is known to be very accurate on the electronic structure calculations compared to the other methods. It is employed for first time to determine the electronic properties: band structure, densities of states and the optical properties. These properties have been studied experimentally in the past especially and also theoretically with on-self-consistent orthogonalized linear combination of atomic orbitals (OLCAO) for Si_2N_2O. In our work, we applied FP-LAPW+lo method for Si_2N_2O and Ge_2N_2O and our results are in good agreement with experiments/theoretical works. The calculations on Ge_2N_2O are purely predictive because this material remains unusable and we have shown that it is a very interesting material from electronic structure point view. We have also applied the plane wave pseudo-potential (PW-PP) method to calculate the elastic properties and density functional perturbation theory (DFPT) for phonons. In particular their elastic constants have been performed and satisfied the *Born* mechanical stability criteria, highlighting the fact that the Si_2N_2O and Ge_2N_2O structures are mechanically stables. The elastic constants are reported for the first time and thermodynamic properties are deduced from these calculations.

Therefore we are able to conclude this work. Using the modern computational methods for material modeling, we have simulated the properties of new materials and made prediction of new phenomena as well as timed explain experimental observations. These different materials could be highly interesting materials for modern and future industrial applications.

Annex

Annex 1: Calculation of elastic stiffness constants

The mechanical properties of materials are of crucial importance for technological applications. A solid body which is subject to external forces, or a body in which one part exerts a force on neighbouring parts, is in a state of stress. If such forces are proportional to the area of the surface of the given part, the force per unit are so-called the stress. The stress in a crystalline material is a direction dependent quantity and, therefore, is in general described by the stress tensorσ_{ij} .

$$[\sigma] = \begin{bmatrix} \sigma_{11} & \sigma_{12} & \sigma_{13} \\ \sigma_{21} & \sigma_{22} & \sigma_{23} \\ \sigma_{31} & \sigma_{32} & \sigma_{33} \end{bmatrix} \quad \text{(A-1)}$$

If all parts of the body are in equilibrium and body forces are absent the equation:

$$\frac{\partial \sigma_{ij}}{\partial x_j} = 0 \quad \text{(A-2)}$$

It must be fulfilled. The symbols x_i denotes the Cartesian axes. The deformations of the solid caused by the exerted stress are described by the strain tensor defined as:

$$[\epsilon] = \begin{bmatrix} \epsilon_{11} & \epsilon_{12} & \epsilon_{13} \\ \epsilon_{21} & \epsilon_{22} & \epsilon_{31} \\ \epsilon_{31} & \epsilon_{32} & \epsilon_{33} \end{bmatrix} \quad \text{(A-3)}$$

If u_i is the displacement of a point x_j in a deformed solid, the strain tensor element is then defined as

$$\epsilon_{ij} = \frac{1}{2}\left(\frac{\partial u_i}{\partial x_j} + \frac{\partial u_j}{\partial x_i}\right) \quad \text{(A-4)}$$

The diagonal components ϵ_{11}, ϵ_{22} andϵ_{33} are called tensile strains, whereas theother components are usually denoted as shear strains. Both stress and straintensors are symmetrical.

The linear theory of elasticity provides a mathematical description for the phenomenological fact, that relative elongations and distortions (or strains in general) are linearly proportional to applied stresses, provided that these stresses are kept to suitable small magnitudes. Once the stresses are removed, an ideal linearly elastic body returns to the unstrained state. This theoretical model does not refer to any model for real matter, and the atomistic nature of matter does not enter as a prerequisite to this concept. The range of the stress for which the assumption from above applies is called the elastic limit. Beyond the elastic limit a non-linear effects break the (linear) proportionality between stress and strain, and for large stresses a plastic dissipation makes the deformation irreversible.

The most general linear relationship which connects stress to strain is provided by the generalized version of the well-known Hooke's law:

$$\sigma_{mn} = C_{mnpr}\epsilon_{pr} \tag{A-5}$$

in which σ_{mn} denotes the stress tensor, ϵ_{pr} the strain tensor and the elements of the fourth-order tensor C_{mnpr} are the so-called elastic constants. Alternatively, one might express the strains in terms of the stresses by

$$\epsilon_{mn} = S_{mnpr}\sigma_{pr} \tag{A-6}$$

defining the elastic moduli S_{mnpr}. The elastic constants and elastic moduli are fundamental materials parameters providing detailed information on the mechanical properties of materials.

The knowledge of these data may enable prediction of mechanical behaviour in many different situations. Whereas σ_{mn} and ϵ_{pr} are symmetric and have therefore only 6 independent elements, the number of 36 elastic constant is reduced by symmetry arguments to a total of 21. The elastic energy density U, which is defined as the total energy per volume, is obtained from the stress tensor (force per unit area) by integration of Hooke's law

$$U = \frac{E}{V} = \frac{1}{2}C_{mnpr}\epsilon_{mn}\epsilon_{pr} \tag{A-7}$$

So far, the strain tensor has been considered as a tensor of order two of the form

$$\epsilon = \begin{pmatrix} 1 + e_{xx} & \frac{1}{2}e_{xy} & \frac{1}{2}e_{zz} \\ \frac{1}{2}e_{yx} & 1 + e_{yy} & \frac{1}{2}e_{yz} \\ \frac{1}{2}e_{zx} & \frac{1}{2}e_{zy} & 1 + e_{zz} \end{pmatrix} \tag{A-8}$$

Introducing the convenient matrix-vector notation, where the 6 independent elements of stress and strain are represented as vectors (denoted as $\sum_i$ and ε_j with i, j running from 1 . . . 6 according to the sequence *xx; yy; zz; yz; xz; xy*), and furthermore rewriting the fourth order tensor C_{mnpr} as a 6x6 matrix c_{ij}.

Table A.1: The number of independent elastic constants for different lattice symmetries and point groups **[LePage-01].**

Lattice (point group)	No. of constants
Triclinic	21
Monoclinic	13
Orthorhombic	9
Tetragonal(4, -4, 4/m)	7
Tetragonal(422, 4mm, -42/m, 4/mmm)	6
Hexagonal and rhombohedral(3, -3)	7
Hexagonal and rhombohedral (32, 3m, -32/m)	6
Hexagonal (6, -6, 6/m, 622, 6mm, -62m, 6/mmm)	5
Cubic	3

Taking into account additional symmetry arguments imposed by the crystal lattice, the number of elastic constants further decreases. In particular, for a cubic lattice only three independent elastic constants, C_{11}, C_{12}, C_{44} remain, whereas for an orthorhombic lattice the 9 elastic constants C_{11},C_{12}, C_{13}, C_{22}, C_{23}, C_{33}, C_{44}, C_{55} ,C_{66}, are sufficient, Since the examples discussed here are cubic and orthorhombic crystals, the explicit form of the tensor is given for these two cases:

$$C_{cubic} = \begin{pmatrix} c_{11} & c_{12} & c_{12} & 0 & 0 & 0 \\ c_{12} & c_{11} & c_{12} & 0 & 0 & 0 \\ c_{12} & c_{12} & c_{11} & 0 & 0 & 0 \\ 0 & 0 & 0 & c_{44} & 0 & 0 \\ 0 & 0 & 0 & 0 & c_{44} & 0 \\ 0 & 0 & 0 & 0 & 0 & c_{44} \end{pmatrix} \quad \text{(A-9)}$$

$$C_{orthorhombic} = \begin{pmatrix} c_{11} & c_{12} & c_{13} & 0 & 0 & 0 \\ 0 & c_{22} & c_{23} & 0 & 0 & 0 \\ 0 & 0 & c_{33} & 0 & 0 & 0 \\ 0 & 0 & 0 & c_{44} & 0 & 0 \\ 0 & 0 & 0 & 0 & c_{55} & 0 \\ 0 & 0 & 0 & 0 & 0 & c_{66} \end{pmatrix} \quad \text{(A-10)}$$

Annex 2: Quasi-harmonic Debye model

To investigate the temperature and pressure dependences of thermodynamic properties of a crystal, the quasi-harmonic Debye model is applied, in which the phononic effect is considered. This model is described in detail in Ref. **[Blanco-04]**. In the following, we make a brief description for this model.

The Debye model is based on the estimation of the Debye temperature, using the isotropic approximation **[McLellan-80].**

$$\Theta = \frac{\hbar}{k_B}[6\pi^2 V^{\frac{1}{2}} n]^{1/3} f(v)\sqrt{\frac{B_S}{M}} \tag{A-11}$$

where V is the molecular volume, M the molecular mass of the compound, B_S the adiabatic bulk modulus, *f(v)* the scaling function **[Francisco-98**, **Francisco -01]**, that depends on Poisson's ratio *v***[Poirier-91]**, **[Maradudin-71]** of the isotropic solid and k_B the Boltzmann constant.

B_S can be approximated by the static bulk modulus B static, leading to the following equation:

$$B_s = B_{static} = V\left(\frac{d^2E(V)}{dV^2}\right) \tag{A-12}$$

Where E is the total energy for each volume of the crystal, obtained from FP-LAPW method at static conditions (T = 0 K). As a first step, the Equation of mechanical stability of a compound is used to obtain the Debye temperature that is calculated from the static bulk modulus B_0, which is determined using one of the three empirical EOS (Vinet, Birch–Murnaghan and spinodal EOS) **[Poirier-91].**

A quasi-harmonic Debye model is then used to obtain the vibrational Helmotz free energy $A_{vib}(\Theta, T)$as a function of temperature at each volume

$$A_{vib}(\Theta, T) = nk_B\left[\frac{9}{8}\frac{\Theta}{T} + 3\ln\left(1 - e^{-\Theta/T}\right)\right] - D(\Theta/T) \tag{A-13}$$

Where *D(y)* is the Debye integral defined as

$$\begin{cases} D(y) = \frac{3}{y^3}\int_0^y \frac{x^3}{e^{x-1}}dx \\ x = \frac{\hbar\omega}{k_B T} \end{cases} \tag{A-14}$$

The *(p,T)* equilibrium situation is then obtained by minimizing the dynamic Gibbs energy G* with respect to *V*. The non-equilibrium Gibbs energy is given by **[Francisco-98]**

$$G^*(V,p,T) = E(V) + pV + A_{vib}(\Theta(V),T) \quad \text{(A-15)}$$

The equilibrium *V(p,T)* curve (the thermal equation state (EOS)) is obtained by solving the equation:

$$\left(\frac{\partial G^*(V,p,T)}{\partial V}\right)_{p,T} \quad \text{(A-16)}$$

The isothermal bulk modulus is then defined as

$$B_T(p,T) = -V\left(\frac{\partial p}{\partial V}\right)_T \quad \text{(A-17)}$$

The adiabatic bulk modulus is given by

$$B_s = B_s(1 + \alpha\gamma T) \quad \text{(A-18)}$$

Where α and γ are the thermal expansion coefficient and Grüneisen parameter, respectively. The common thermodynamic parameters that depend on temperature and pressure are used to derive other macroscopic properties.

References

[Blanco-04]M.A. Blanco, E. Francisco, V. Luana, Comput. Phys. Commun. 158, 57(2004).

[Francisco-01]E. Francisco, G. Sanjurjo, M.A. Blanco, Phys. Rev. B 63, 094107 (2001).

[Francisco-98]E. Francisco, J.M. Recio, M.A. Blanco, A. Martin Pendas, J. Phys.Chem. 102, 1595(1998).

[LePage-01]Y. Le Page,P. Saxe. Phys Rev B, 63, 174103 (2001).

[Maradudin-71] A.A. Maradudin, E.W. Montroll, G.H. Weiss, I.P. Ipatova, *Theory of Lattice Dynamics in the Harmonic Approximation*, AcademicPress, 1971.

[McLellan-80]A.G. McLellan, *The Classical Thermodynamics of Deformable Materials*, vol. 165, Cambridge University Press, 1980.

[Poirier-91] J.P. Poirier, *Introduction to the Physics of the Earth's Interior*, Cambridge University Press, 1991.

Abstract: The aim of the present thesis is to study the physical properties of crystalline materials using the density functional theory (DFT) by means of two methods, the full-potential linearized augmented plane-wave plus local orbitals and plane-wave pseudopotential. After presentation of the employed method and its conceptual basis as well as the most recent developments, we will pay more attention to a direct application of the introduced method to compute the structural, electronic and magnetic properties as well as the mechanical stability criteria in different systems. The effect of strong correlation will be undertaken using both of the Hubbard (U) parameter and the spin-orbit coupling. It is worthwhile to see that the rare-earth dioxides need the application of both corrections: U and SOC compared to the rare-earth nitrides, where GGA+U is sufficient to describe correctly the electronic structure. The last application concerns the oxynitrides based on silicon and germanium, where structural, electronic, elastic, electronic optical and dynamical properties are detailed.

Key words: DFT, nitrides, rare earth dioxide, the oxynitride, Lapw, pseudopotential, Hubbard, spin-orbit coupling.

Résumé : L'objectif de la thèse est d'étudier les propriétés physiques des matériaux cristallins en utilisant la théorie de la fonctionnelle de densité (DFT) implémentée sous deux approches : la méthode linéaire des ondes plane augmentées plus orbitales locales et la méthode de pseudopotentiel. Les fondements de cette théorie ainsi que ces récents développements, qui permirent de palier aux problèmes numériques rencontrés dans les systèmes complexes comme les terres rares, seront détaillés. Nous aborderons ensuite le calcul des propriétés structurales, électroniques et magnétiques ainsi que le critère de stabilité mécanique et énergétique des différents systèmes. Le problème de la forte corrélation électronique sera ensuite abordé dans les dioxydes de terre rare via l'introduction du paramètre de Hubbard (U) ainsi que le couplage spin-orbite qui corrigeront la structure électronique. Il est intéressant de voir que les dioxydes de terre rare nécessitent l'application des deux corrections: U et SO alors que les nitrure de terre rare exige que la correction U. Nous avons étendu notre étude à des matériaux potentiellement important à savoir les oxynitrures à base de silicium et de germanium.

Mots clés : DFT, les nitrures, les dioxydes de terre rares, les oxynitrure, LAPW, pseudopotentiel, hubbard, couplage spin orbit